Structural Engineering Report No. ST-96-6

A Cyclic Distributed Plasticity Formulation for Three-Dimensional Rectangular Concrete-Filled Steel Tube Beam-Columns and Composite Frames

Aleksandr Molodan and Jerome F. Hajjar

August 1997

Department of Civil Engineering
Institute of Technology
University of Minnesota
Minneapolis, Minnesota 55455

Abstract

This research presents a three-dimensional, cyclic, geometrically and materially nonlinear distributed plasticity finite element model for square or rectangular concrete-filled tube (CFT) beam-columns used in composite frames consisting of steel I-girders framing rigidly into CFT beam-columns. This formulation is most effective for studying the entire load-deformation behavior of CFTs as part of complete composite frames subjected to either monotonic or cyclic loading. It is also suitable for conducting comprehensive parametric studies of individual CFT beam-columns or composite subassemblages, which, in conjunction with experiments, may provide the data required to improve the accuracy and scope of current non-seismic and seismic design specification provisions for CFTs.

The distributed plasticity model, developed within the context of a stiffness-based beam-column finite element formulation, discretizes the CFT cross-sections at the beam ends into a grid of fibers, and the stress-strain behavior of each steel and concrete fiber is monitored explicitly during the loading history. Frame members are modeled as line beam-column elements with their degrees-of-freedom located at the centroidal axis at each element end. The cross-sectional stiffness of each element end is obtained using numerical integration over all the fibers, and interpolation functions are used to integrate along the element length. The modeling of geometric nonlinearity is based upon a co-rotational formulation, and the terms retained in the stiffness matrix and force recovery account sufficiently for all significant P-δ and P-Δ effects within the CFT beam-column.

The steel and concrete constitutive formulations account for the significant inelastic phenomena which are exhibited in cyclic CFT experiments and which greatly affect the behavior of CFTs. The steel formulation models the rounded shape of the stress-strain curve found in cold-formed tube steel, a decreasing elastic zone with increased cyclic excitation, cyclic hardening, ratchetting, and the different stress-strain behavior exhibited in the corners and flanges of cold-worked steel tubes. The concrete formulation models strength and stiffness degradation by means of a cumulative damage parameter, and the post-peak behavior of the concrete is calibrated to account implicitly for the effects of confinement of the concrete core by the steel tube. The concrete formulation also models fibers which cycle into tension and then back into compression. In addition, slip is accounted for between the steel and concrete components of the CFT by incorporation of a nonlinear slip interface. This interface allows axial movement of the concrete core with respect to the steel tube. It is able to capture behavior ranging from perfect bond to perfect slip.

The model is verified against several monotonic and cyclic experiments of CFT beam-columns. A final experimental comparison consists of a cyclically loaded three-dimensional subassemblage of three steel I-beams framing into a CFT beam-column, which is thus subjected to cyclic biaxial bending plus axial compression.

Acknowledgments

The authors would like to thank the contributions of Dr. H. Shakir-Khalil, University of Manchester, U. K., Dr. S. Morino, Mie University, Japan, Dr. T. Usami, Nagoya University, Japan, Dr. O. Buyukozturk, Massachusetts Institute of Technology, Dr. J. M. Ricles, Lehigh University, Dr. D. W. White, Georgia Institute of Technology, Mr. P. H. Schiller, Barr Engineering, Minneapolis, Minnesota, and Mr. B. C. Gourley, Hammel, Green, and Abrahamson, Minneapolis, Minnesota, for providing details of their work and suggestions for the current research.

This research was supported by the National Science Foundation (Grant No. CMS-9410473) under Dr. Shih-Chi Liu and Dr. M. P. Singh, and the Department of Civil Engineering at the University of Minnesota. This support is gratefully acknowledged. Any opinions, findings, and conclusions or recommendations expressed in this material are those of the authors and do not necessarily reflect the views of the National Science Foundation.

Table of Contents

List of Figures

List of Tables

Chapter 1

Introduction

Composite steel-concrete structures have been steadily gaining in popularity as an economical alternative to either all steel or all concrete building frames. Two main types of composite beam-columns are encased steel shapes and concrete-filled steel tubes (CFT). Concrete-filled tubes consist of either circular or rectangular steel tubes filled with reinforced or unreinforced concrete. This type of composite element provides many advantages, particularly for use in the low or moderate rise unbraced frames.

The combination of the high tensile capacity of steel with the compressive resistance of concrete leads to an element with enhanced axial and flexural capacity. The concrete core delays or prevents buckling of the steel shell. Alternately, the steel tube provides some confinement of concrete at high levels of axial load, increasing the concrete strength and especially its ductility, as well as preventing concrete spalling (Sakino and Tomii, 1981). Placing the steel at the perimeter of the beam-column also makes its use optimal for uniaxial or biaxial bending. Concrete-filled steel tubes exhibit high torsional stiffness, making them less susceptible to torsional and lateral-torsional buckling modes that are typical for steel shapes. In addition, crushing of the concrete combined with the steel yielding provides an energy dissipation mechanism important for ductile behavior under seismic loading. The combination of increased ductility of the concrete and delayed local buckling of the steel contributes to improved cyclic resistance of CFTs, manifested by their ability to withstand further cyclic loading even after initial

local buckling of steel and some crushing of concrete (Matsui, 1985). Concrete-filled tubes are often more economical than other structural types, and their construction is potentially faster and requires less formwork that reinforced concrete or encased shapes (Bridge and Webb, 1993).

Concrete-filled tube beam-columns are particularly promising for earthquake resistant structures due to their excellent resistance to cyclic loading. In order to predict CFT behavior, both experimental and computational studies must be conducted. This research focuses on the computational modeling of CFTs, while experimental results are utilized for calibration and verification of the proposed model. The primary objective of this research is to develop a three-dimensional, geometrically and materially nonlinear distributed plasticity finite element model for cyclic analysis of square or rectangular CFT beam-columns used in low- to moderate-rise unbraced frames.

1.1 Overview of Fiber Analysis of CFTs

A stiffness-based beam-column finite element forms the basis of the CFT model. The element degrees-of-freedom are displacements and rotations of the element ends, and the stiffness formulation is based on the stress resultants (forces and moments) at the element ends. This formulation utilizes the fiber element approach for modeling distributed plasticity. The model discretizes the CFT cross section at the beam ends into a grid of fibers, and the stress-strain behavior is tracked explicitly at each fiber. The stress resultants are obtained by numerical integration of stresses through the cross section. Fiber element formulations require less computing time than three-dimensional continuum finite elements, yet they permit direct modeling of the variation of material properties across the element cross section, and they may account explicitly for such effects as residual stresses or initial plastic strains.

The use of these types of finite elements has been well documented for decades by many researchers and has been shown to provide an accurate representation of the behavior of beam-column elements in structural frames. A wide variety of fiber (or, in two-dimensions, "layered") elements have been used to model steel wide-flange beam-columns (Wright and Gaylord, 1968; Alvarez and Birnstiel, 1969; Kanchanalai, 1977; White; 1985; Izzuddin and Elnashai, 1993; Challa and Hall, 1994), reinforced concrete beam-columns (Krishnamoorthy, 1987; Taucer et al. 1991; Chang and Mander, 1994; Izzuddin et al., 1994; Ahmad and Weerakoon, 1995), and steel reinforced concrete beam-columns (Roik and Bergmann, 1992; Elnashai and Elghazouli, 1993; El-Tawil and Deierlein, 1996), to name only a few.

Several fiber-based models for CFT analysis may be found in the literature. Most were formulated for monotonic analysis of individual CFT beam-columns, often in two dimensions (axial force and uniaxial bending). Very few models of this type have been developed for CFT beam-columns as part of frames. Bode (1976), Bridge (1976), Tomii and Sakino (1979), Shakir-Khalil and Zeghiche (1989), and Tsuji et al. (1991) have presented fiber-based formulations for monotonic CFT analysis. There are also several fiber formulations capable of cyclic analysis of CFTs which are briefly reviewed below.

The formulation of Kawaguchi et al. (1991, 1993) uses uniaxial steel and concrete stress-strain relations for the analysis. The tensile branch of the steel stress-strain curve consists of linear elastic and linear strain hardening regions connected by a curvilinear elasto-plastic transition zone. The compressive branch of the steel stress-strain curve has the linear elastic region followed by the elasto-plastic transition zone. As soon as the strain level corresponding to local buckling is reached, the stress-strain curve assumes a negative slope. This negative slope of a fiber accounts approximately for the strength and stiffness degradation caused by local buckling of the steel tube. A relation proposed by Popovics is used for the concrete stress-strain curve; upon reaching the compressive strength, the fiber is assumed to maintain a constant stress level in compression to account for the beneficial effect of confinement. Both the steel and the concrete models

are cyclic, and they are used to predict a force-deflection curve of individual CFT beam-columns loaded in cyclic shear plus axial force.

The formulation of Inai and Sakino (1996) also utilizes uniaxial cyclic steel and concrete stress-strain models for fiber analysis of CFT beam-columns. The concrete stress-strain model accounts for the enhancement in ductility caused by confinement by making the rate of softening in the postfailure region smaller than that of plain concrete. A bilinear relation is used for the tensile branch of the steel stress-strain curve. For the compressive branch, a linear elastic region is followed by a linear strain hardening region until the maximum compressive stress is reached. The stress-strain curve then descends linearly until the stress is equal to a specified percentage of the maximum compressive stress, with the compressive stress level remaining constant thereafter. This formulation approximately accounts on the fiber level for the concrete confinement and for the local buckling of the steel tube. Both the concrete and steel models have several empirical parameters that have been calibrated to a series of CFT tests, rather than to material tests. The formulation was used to predict the cyclic behavior of CFTs subjected to cyclic shear and axial force. The computational results show good agreement with experimental data obtained from tests conducted by authors.

1.2 Objective of the Research

Kawaguchi et al. (1991, 1993) and Inai and Sakino (1996) focused their analyses on modeling individual CFTs, rather than on the analysis of composite CFT frames, and much of the other computational research conducted on CFTs to date has focused mainly on computing the ultimate axial and flexural capacity of individual members (Gourley et al., 1995). The objective of this research is to develop a three-dimensional, geometrically and materially nonlinear distributed plasticity finite element model to analyze low- to moderate-rise unbraced frames consisting of steel I-girders framing rigidly into square or

rectangular CFT beam-columns. In contrast to existing formulations directed toward modeling individual CFT members, the current formulation provides an efficient method to study both the significant stress-strain behavior of a CFT member and the load-deformation behavior of CFTs as part of complete composite frames. The model is intended for use in parametric studies of cyclic CFT behavior, as well as for the analysis of entire composite frames consisting of CFT columns with rigidly framing steel girders.

To obtain a realistic description of CFT behavior, both a geometrically nonlinear formulation and an accurate model of the material response are developed. The geometric formulation, developed by Schiller and Hajjar (1996) for monotonic behavior of CFTs, is utilized in the current research for modeling cyclic behavior. This formulation is also capable of modeling slip at the concrete core - steel tube interface (Hajjar et al., 1997b).

Current design approaches for seismically resistant structures generally assume that the structural elements will be loaded in the inelastic range when the structure is subjected to severe earthquake loading. The inelastic capacity of the elements is important to provide structural ductility and energy dissipation. Consequently, cyclic analysis of the CFT must account for the inelastic behavior of both steel tube and concrete core. Thus, constitutive models for both steel and concrete capable of representing inelastic cyclic behavior are required. Development and implementation of cyclic plasticity models suitable for the analysis of CFTs is the main focus of this research (Hajjar et al., 1997c). Since the interaction of concrete and steel generally causes a multiaxial state of stress in the steel tube and concrete core, multiaxial plasticity models are used as the basis for the analysis. This selection makes it easier to incorporate multiaxial behavior in the analysis, although currently only uniaxial (longitudinal) stress and strain are calculated explicitly in the steel tube and concrete core.

1.3 Overview of Cyclic Experiments of CFTs

The role of the experimental results in the computational studies of structural behavior is threefold. First, in order to understand and properly model the behavior of CFTs, the experimental results must be carefully studied, so that salient features of the CFT load-deformation response may be identified and accounted for in the computational modeling procedure. Second, the material models must be calibrated to the experimental results on the material stress-strain and, possibly, member levels. Third, the computational predictions must be verified by comparing to a selected suite of CFT experiments in order to demonstrate the validity of the model. Therefore, familiarity with and understanding of the experimental research on cyclically loaded CFTs are essential for this work. Toward this goal, a brief description of experiments involving rectangular CFTs subjected to cyclic loading is provided.

Experimental studies of CFTs have been conducted for several decades. Early studies focused primarily on determining the axial and flexural capacity of single members, and utilized relatively simple loading histories. Later studies focused on the behavior of CFT members subjected to more complex loading programs such as biaxial bending, non-proportional loading, and cyclic loading. Effects of different structural parameters including material strength and geometric proportions were also studied. A comprehensive review of many of the experiments conducted on CFT beam-columns is presented by Gourley et al. (1995). A short review of several experimental studies involving cyclic loading of rectangular CFT specimens is given below.

In the experimental program of Sakino and Tomii (1981), fifteen specimens were subjected to a combination of constant axial load and cyclic shear load. The cyclic loading was displacement controlled, with each specimen subjected to three cycles of shear loading at increasing displacement levels. The specimens were bent in double curvature, with the support conditions simulating fixed ends. The main test parameters were the specimen width-to-tube thickness ratio (referred to as D/t), the ratio of axial load

to nominal axial strength of the column (referred to as P/P_0), and the shear span ratio. All specimens in these tests were short, stocky tubes filled with low strength concrete. The authors concluded that the effect of the shear span ratio on CFT strength was negligible for the small ratios used in these experiments, while an increase in either the D/t ratio or the P/P_0 ratio caused a decrease in the member strength. For specimens with a relatively high axial load, an initial decrease in shear strength during cyclic loading was followed by a stabilization and even a slight increase of the strength. The authors attributed this strength increase to an increase of the concrete confinement, as the steel tube gradually transformed from a rectangular to a more circular shape. This change in shape was observed in the regions of maximum curvature at the member ends following initial local buckling. Significant axial shortening of the CFTs was also observed in these tests.

The tests by Sakino and Ishibashi (1985) were conducted as a continuation of the earlier study by Sakino and Tomii (1981) and used similar procedures and testing equipment. They included nine specimens of relatively short CFTs subjected to combined constant axial force and cyclic shear loading, as well as twelve specimens loaded monotonically by axial and shear forces. The goal of these tests was to study the behavior and failure mechanisms of CFT beam-columns loaded primarily in shear. The transformation of tube shape after the initial local buckling and corresponding stabilization and slight increase of shear capacity were also observed in these tests. The specimens having larger D/t ratios exhibited a greater reduction of shear strength with successive loading cycles.

In the experiments described in (Matsui, 1985) and (Matsui, 1986), the behavior of one bay, one story frames was studied. The frames had either CFT or hollow steel tube columns and steel girders. The columns had short tubes with mid-range D/t ratios, filled with moderate strength concrete. Both overall frame behavior and the behavior of the beam-to-column connections were studied. The frames were loaded by constant axial force applied to the columns, followed by monotonic or cyclic shear force under displacement control. The goal of these tests was to compare the behavior of frames with CFT columns to ones with hollow steel tube columns, and to provide experimental

support to a connection design procedure. The observed strength of the CFTs was higher than the value predicted by plastic limit analysis, while the strength of hollow steel tubes was lower than the computed value because of the steel local buckling. The CFT specimens also exhibited a better post-buckling behavior than the hollow tubes. The authors attributed the superior behavior of CFTs to the delay or prevention of local buckling of the steel tube by the concrete infill. The presence of concrete in the CFTs forced the steel to buckle outwards, while both inward and outward buckling modes were observed for hollow steel tubes. The improvement of the post-buckling behavior of CFTs was caused by the transfer of a significant portion of axial load to the concrete core following local buckling, so that the CFT members were able to retain much of their strength after local buckling of the steel tube.

The experiments of Matsui and Tsuda (1987) included CFTs and hollow steel tube cantilever beam-columns with high D/t ratios subjected to axial force and monotonic or cyclic shear force. Six CFTs were loaded with cyclic shear in displacement control at the points corresponding to the inflection points of a frame, so that the behavior of a beam-column as part of a frame was simulated. The main test parameters were the presence of concrete, D/t ratio, and type of shear loading (monotonic or cyclic). Low strength concrete was used in the CFTs. The CFT specimens were able to achieve the strength predicted by the plastic limit analysis, even for relatively large D/t ratios, while the strength of the hollow steel tube columns was below the predicted values, similarly to the results reported by (Matsui, 1985). The CFT load-deformation curves showed significant energy dissipation capacity and large ductility.

Cyclic behavior of CFT braces was investigated by Liu and Goel (1988). A test frame with CFT braces was loaded cyclically to simulate the behavior of a structure subjected to seismic load. This type of loading caused the CFT specimens to be cycled repeatedly between tension and compression. The main testing parameters were presence of concrete, D/t ratio, brace slenderness, and concrete strength. Slender elements with mid-range D/t ratios filled with low strength concrete were tested with displacement controlled loading. The concrete presence was observed to change the mode of the steel

tube local buckling, reduce its severity, and delay crack formation, thus increasing the number of cycles to failure.

Strength deterioration caused by local buckling of the steel tube in cyclically loaded CFT beam-columns was the focus of the experiments conducted by Kawaguchi et al. (1991). Four CFTs and four hollow steel tube cantilever specimens were subjected to axial load and cyclic shear load. The cyclic shear load was displacement controlled, and each specimen was subjected to ten cycles of loading at a displacement amplitude equal to the amplitude observed at local buckling of a virgin specimen. The main test parameters were presence of concrete and the axial load ratio P/P_0. Short columns with low D/t ratios, filled with low strength concrete were tested. The CFT specimens were observed to have less strength deterioration and more energy dissipation capacity than the hollow steel tubes.

The experimental program of Kawaguchi et al. (1993) was also concerned with documenting strength deterioration caused by local buckling, as well as energy dissipation of the CFT specimens loaded cyclically. Fourteen CFTs and twelve hollow steel cantilever beam-columns were subjected to axial force and cyclic shear. The main test parameters were the D/t ratio, the P/P_0 ratio, and the ratio of displacement amplitude to the displacement observed at local buckling of a virgin specimen. Relatively short columns with low to mid-range D/t ratios, filled with low strength concrete, were tested. The loading was displacement controlled. The CFT specimens were able to retain most of their strength and reach a stabilization, while the hollow steel tubes experienced significant strength deterioration following local buckling. The concrete core contribution to the flexural strength in bending was not significant, but its ability to inhibit local buckling of the steel tube increased the energy dissipation capacity of CFTs.

Tests by Sugano et al. (1992) were conducted to investigate the effect of concrete confinement on both strength and ductility of cyclically loaded CFTs and to incorporate the confinement effect into design guidelines. Nineteen rectangular and nineteen circular CFT beam-columns were tested. The specimens were simply supported and were loaded with constant axial load and cyclic transverse load. The cyclic loading was displacement

controlled. The main test parameters were the specimen shape (square or circular), the D/t ratio, the P/P_0 ratio, and concrete and steel strength. All specimens were short members, with the D/t ratio and material strength varying from low to high values. The ductility of the members was observed to decrease with an increase of the D/t ratio or the P/P_0 ratio. In contrast to observations of other researchers, the authors concluded that the increase of concrete strength caused by confinement was significant, even for rectangular CFTs.

In the experiments of Morino et al. (1993), three-dimensional cruciform subassemblies were subjected to cyclic nonproportional loading. The subassemblies consisted of a CFT beam-column into which four steel girders were framed. The column was loaded by a constant axial load, while one of the girders framing into the minor axis of the column had a constant transverse tip load. The girders framing into the major axis of the column were loaded with anti-symmetric cyclic transverse tip loads which were displacement controlled. This pattern of loading resulted in a combination of axial force and nonproportional biaxial bending being applied to the CFT specimens. The CFT beam-columns had mid-range lengths and D/t ratios; low strength concrete was used. Half of the specimens were designed to experience column failure prior to connection failure, and the other half were detailed for connection failure to occur first. The details of one experiment designed for the column failure are presented in Chapter 5, where the computational results are compared to the experimental data.

Documentation of the cyclic load-deformation behavior and ultimate strength and ductility of CFT beam-columns were the focus of the study by Fujimoto et al. (1996). Thirteen circular and twenty square CFTs were subjected to axial load and cyclic shear load. Short CFT members with mid-range D/t ratios were tested; strength of the steel and concrete varied from low to high values. Axial load was varied for four circular and four square specimens, and was constant for the other tests. The method of load application and testing apparatus were similar to those described in (Sakino and Tomii, 1981). The test setup simulated fixed end conditions and induced double curvature in the specimens. The cyclic shear loading was displacement controlled. The main test parameters were

tube shape (square and circular), D/t ratio, strength of the steel and concrete, axial load ratio P/P_0, and loading angle for biaxial bending. The rotation capacity and axial strength of circular specimens exceeded those of similarly-sized square specimens. Rotation capacity and maximum strength were smaller for the variable axial load specimens, and were not affected by the loading angle.

Portal frames consisting of CFT columns and a steel girder were tested by Kawaguchi et al. (1996). The columns were loaded by constant axial load, the top of the frame was restrained against sidesway, and the bottom of the frame was loaded by a cyclic horizontal load. The goal of this study was to investigate the frame strength and deformation capacity in cyclic loading. The main test parameters were the failure mode of the frame (column failure or connection failure), and axial load ratio P/P_0. CFT members had relatively short lengths and mid-range D/t ratios; moderate strength concrete was used. The authors concluded that frames utilizing CFT columns exhibit better hysteretic characteristics than similar steel frames do.

1.4 Scope of the Concrete-Filled Steel Tube Fiber Model

The fiber element model developed in this research has been incorporated into a general purpose frame analysis program. This program, CFTFiber, is capable of conducting monotonic and cyclic static analysis of CFT elements or composite frames consisting of CFT and steel members. The fiber element formulation complements a concentrated plasticity CFT finite element model developed by Gourley and Hajjar, (1994) which is suitable for conducting static, transient dynamic, and eigenvalue buckling analysis of composite CFT frames (Gourley and Hajjar, 1994; Hajjar and Gourley, 1996; Hajjar et al., 1997b, c). While computationally more expensive than the concentrated plasticity model, the fiber element formulation in the present work provides more detailed

information which is critical for conducting parametric studies of CFT subjected to monotonic or cyclic loading, and for assessing member and frame ductility.

The current research is limited to frame structures consisting of steel I-beams framing into square or rectangular CFTs. The steel constitutive model calibration has been conducted for ASTM A500 Grade B steel for CFTs, and ASTM A36 or A572 Grade 50 steel for wide-flange members. The concrete constitutive model calibration has been conducted for concrete strengths (f_c') up to 50 MPa. The CFTs are assumed to be completely filled with concrete and to have no reinforcement or shear connectors. Confinement of the concrete core of the CFT by the steel tube is accounted for through calibration of the concrete constitutive model. Residual stresses produced in cold-formed, welded steel tubes vary significantly through the tube thickness (Sherman, 1992) and are accounted for indirectly in the steel constitutive model used in the fiber analysis (Sully and Hancock, 1996). Effects which are not modeled directly in the current formulation include local buckling, nonlinearity due to shear or torsion (since shear and torsional forces are expected to be small in CFT frame members), shear deformations due to flexure (i.e., Euler-Bernoulli beam theory is assumed), time dependent effects on the materials, and post-collapse behavior.

1.5 Overview of the Thesis

Formulation of the beam-column finite element including geometric nonlinearity and modeling of slip between the concrete core and steel tube is presented in Chapter 2. A particular emphasis is placed on the description of how the material nonlinear models are utilized in the finite element formulation. The development of material models is presented in the following two chapters. They describe the requirements which the cyclic plasticity models must satisfy, formulation of the models, and calibration of model parameters to the results of material and CFT tests. The cyclic structural steel model is

described in Chapter 3, and the concrete plasticity model is presented in Chapter 4. Verification of the fiber element formulation including comparison of computational results to both monotonic and cyclic CFT experiments is presented in Chapter 5. Conclusions are drawn and directions for further research are outlined in Chapter 6.

Chapter 2

Beam-Column Finite Element Formulation

All CFT members are modeled in this research using an 18 degree-of-freedom (DOF) beam-column finite element developed by Schiller and Hajjar (1996). This element is similar to the standard 12 DOF element commonly used in the three-dimensional analysis of frames, but it has separate translational degrees-of-freedom for steel and concrete. This separation permits modeling of slip between the concrete core and the steel shell of a CFT member. The element degrees-of-freedom are located at the centroid of the steel tube at each element end cross section. The element end cross sections, in turn, are discretized in two dimensions using a grid of fibers, and interpolating functions specify the variation of cross-sectional properties and element forces. This chapter briefly describes the beam-column element formulation, with a particular emphasis on the inclusion of material nonlinearity in the analysis.

2.1 Element Description

In the CFT finite element, nine degrees-of-freedom are modeled at each element end: three translations for steel, three translations for concrete, and three element end rotations. The layout of these degrees-of-freedom is shown in Figure 2.1.

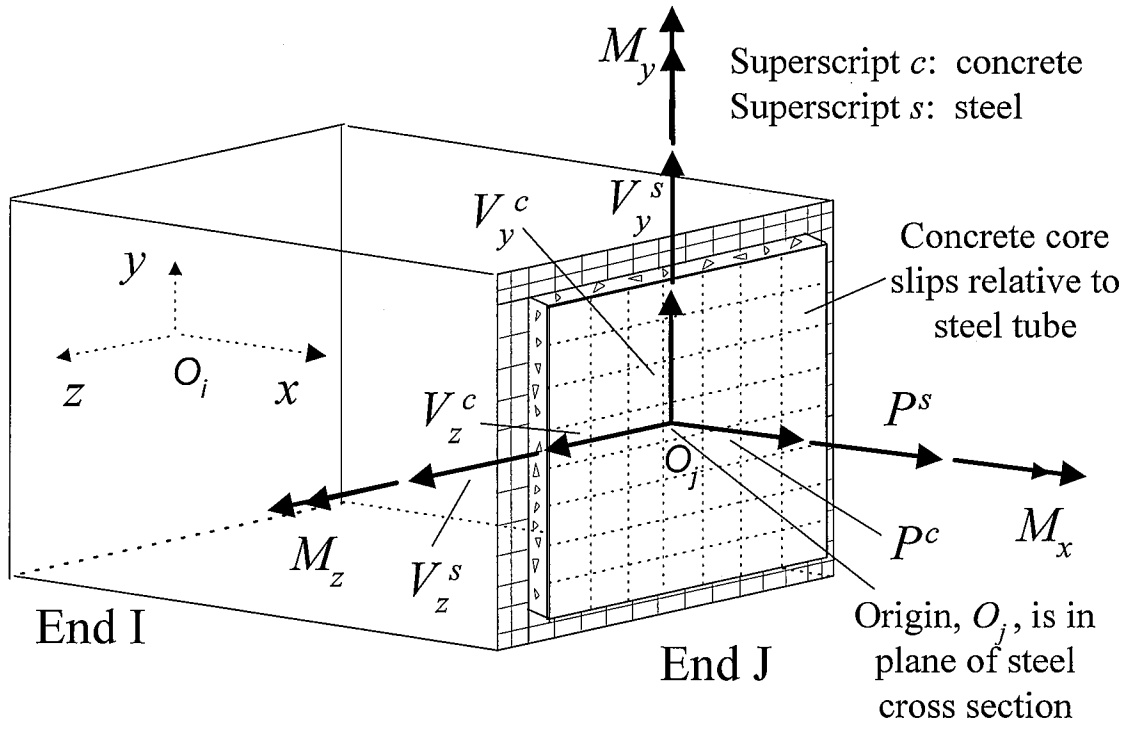

Figure 2.1: Beam-Column Element Degrees-of-Freedom

Translations of the steel and concrete are defined separately to permit modeling of slip between these two materials. Since another CFT element framing into a joint may have a different orientation of its longitudinal axis, translations in all three directions must be considered. This difference of orientation may be caused by either the original layout of structural members or by geometric nonlinearity of elements that were originally aligned in a column stack. However, the transverse displacements of the steel and concrete are assumed to coincide, with slip occurring only in the longitudinal direction of the CFT. Therefore, penalty functions are used to provide shear constraints at each element end.

The slip interface between the steel shell and concrete core of the CFT element is modeled as a spring having a cyclic bi-linear force-deformation relation. In general, any nonlinear force-deformation relation may be incorporated into this slip model. Parameters used to describe the slip-deformation relation were calibrated to the results of

several connection tests. A detailed description of the slip formulation, calibration, and verification is presented by Schiller and Hajjar (1996).

2.2 Equilibrium Equation

Static equilibrium for each CFT element can be written using the principle of virtual work. Elements are assumed to have no body forces since self-weight is neglected. The virtual work equation, with separate terms for steel and concrete, and a term accounting for the slip interface strain energy, may be written as (Schiller and Hajjar, 1996):

$$\int_{^2V^c} {}^2\tau_{ij}^c \delta_2 e_{ij}^{c\,2} dV^c + \int_{^2V^s} {}^2\tau_{ij}^s \delta_2 e_{ij}^{s\,2} dV^s + \int_{^2I} {}^2\pi\, \delta_2 \psi\, {}^2dI = \int_{^2S^c} {}^2t_i^c \delta_2 u_i^{c\,2} dS^c + \int_{^2S^s} {}^2t_i^s \delta_2 u_i^{s\,2} dS^s \tag{2.1}$$

where: ^2V is the volume of the element in configuration C2

^2S is the surface of the element in configuration C2

^2I is the steel-concrete interface in C2 (units of length^2)

$^2\tau_{ij}$ is the Cauchy stress tensor measured in configuration C2

$_2e_{ij}$ is the engineering strain tensor measured with respect to configuration C2

$^2\pi$ is the force transferred between the steel and concrete portions of the element through the slip layer per unit area of the interface (units of force/length^2)

$_2\psi$ is the slip between the steel and the concrete at a point along the element length (units of length)

^2t_i are the surface tractions in configuration C2

${}_2u_i$ are the element deformations measured with respect to configuration C2

In this equation C1 refers to the last converged configuration, and C2 refers to the current (unknown) configuration. All integrals in this equation must be evaluated in the current configuration C2. Following the notation of (Bathe, 1982), a left superscript denotes the configuration in which a quantity is measured, while a left subscript denotes the configuration to which a quantity is referred. If either the left subscript or superscript is not shown, the two configurations are the same. A right superscript denotes the material, where *c* stands for concrete and *s* stands for steel. The right subscript denotes the tensorial components.

This equation can be rewritten so that all quantities are referred to the known configuration C1. This can be done using the second Piola-Kirchhoff stress and Green-Lagrange strain tensors (Bathe, 1982), resulting in the virtual work equation (Schiller and Hajjar, 1996):

$$\int_{{}^1V^c} {}_1^2S_{ij}^c \delta_1 \varepsilon_{ij}^{c\,1} dV^c + \int_{{}^1V^s} {}_1^2S_{ij}^s \delta_1 \varepsilon_{ij}^{s\,1} dV^s + \int_{{}^1I}{}^2\pi\, \delta_2 \psi^1 dI = \int_{{}^1S^c}{}^2t_i^c \delta_1 u_i^{c\,1} dS^c + \int_{{}^1S^s}{}^2t_i^s \delta_1 u_i^{s\,1} dS^s \tag{2.2}$$

where: ${}_1^2S_{ij}$ are the components of the second Piola-Kirchhoff stress measured at C2 with respect to C1

${}_1\varepsilon_{ij}$ are the components of the Green-Lagrange strain measured with respect to C1

In an incremental analysis, the second Piola-Kirchhoff stress may be additively decomposed into the Cauchy stress in configuration C1 and the Piola-Kirchhoff stress increment, which is equal to the contraction of constitutive tensor and the strain increment. This decomposition may be expressed as:

$$ {}_1^2S_{ij} = {}^1\tau_{ij} + \Delta S_{ij} = {}^1\tau_{ij} + {}_1C_{ijkl}\Delta\varepsilon_{ij} \tag{2.3} $$

where: ${}_1C_{ijkl}$ is the material constitutive tensor in configuration C1

The Green-Lagrange strain tensor corresponding to virtual displacements may also be separated into an infinitesimal strain tensor and a nonlinear strain tensor. All components of the infinitesimal strain tensor are linear functions of displacement derivatives, while the nonlinear strain tensor has quadratic components. This separation may be written as:

$$ {}_1\varepsilon_{ij} = {}_1e_{ij} + {}_1\eta_{ij} \tag{2.4} $$

where: ${}_1e_{ij}$ are the components of the infinitesimal strain tensor

${}_1\eta_{ij}$ are the nonlinear components of the Green-Lagrange strain tensor

The incremental deformation of the spring layer at the interface is equal to the difference of the steel and concrete incremental axial deformations. It may be expressed as:

$$ \Delta\psi = \Delta u_c^s - \Delta u_c^c \tag{2.5} $$

where: Δu_c^s is the incremental centroidal deformation of the steel tube

Δu_c^c is the incremental centroidal deformation of the concrete core

Assuming an incrementally linear slip stiffness, the stress at the interface may be written in incremental form as:

$$^{2}\pi = {}^{1}\pi + \Delta\pi = {}^{1}\pi + \hat{k}\Delta\psi \tag{2.6}$$

where: $\hat{k}$ is the tangent stiffness of the interface (units of force/length^3)

Substituting these expressions for the second Piola-Kirchhoff stress tensor, Green-Lagrange strain tensor, and interface stress into Eq. 2.2 results in the following form of the virtual work equation (Schiller and Hajjar, 1996):

$$\begin{aligned}
&\int_{{}^{1}V^c} {}_1C^c_{ijkl}\Delta e^c_{kl}\delta_1 e^{c\,1}_{ij} dV^c + \int_{{}^{1}V^c} {}^{1}\tau^c_{ij}\delta_1\eta^{c\,1}_{ij} dV^c + \\
&\int_{{}^{1}V^c} {}_1C^c_{ijkl}\Delta e^c_{kl}\delta_1\eta^{c\,1}_{ij} dV^c + \int_{{}^{1}V^c} {}_1C^c_{ijkl}\Delta\eta^c_{kl}\delta_1\eta^{c\,1}_{ij} dV^c + \int_{{}^{1}V^c} {}_1C^c_{ijkl}\Delta\eta^c_{kl}\delta_1 e^{c\,1}_{ij} dV^c + \\
&\int_{{}^{1}V^s} {}_1C^s_{ijkl}\Delta e^s_{kl}\delta_1 e^{s\,1}_{ij} dV^s + \int_{{}^{1}V^s} {}^{1}\tau^s_{ij}\delta_1\eta^{s\,1}_{ij} dV^s + \\
&\int_{{}^{1}V^s} {}_1C^s_{ijkl}\Delta e^s_{kl}\delta_1\eta^{s\,1}_{ij} dV^s + \int_{{}^{1}V^s} {}_1C^s_{ijkl}\Delta\eta^s_{kl}\delta_1\eta^{s\,1}_{ij} dV^s + \int_{{}^{1}V^s} {}_1C^s_{ijkl}\Delta\eta^s_{kl}\delta_1 e^{s\,1}_{ij} dV^s + \\
&\int_{{}^{1}I} \Delta\pi\,\delta_1\psi\,{}^{1}dI = \Delta\Re
\end{aligned} \tag{2.7}$$

where: $\Delta\Re$ is the incremental applied load calculated as:

$$\begin{aligned}
\Delta\Re = &\int_{{}^{1}S^c} {}^{2}t^c_i\delta_2 u^{c\,1}_i dS^c + \int_{{}^{1}S^s} {}^{2}t^s_i\delta_2 u^{s\,1}_i dS^s - \\
&\int_{{}^{1}V^c} {}^{1}\tau^c_{ij}\delta_1 e^{c\,1}_{ij} dV^c - \int_{{}^{1}V^s} {}^{1}\tau^s_{ij}\delta_1 e^{s\,1}_{ij} dV^s - \int_{{}^{1}I} {}^{1}\pi\,\delta_1\psi\,{}^{1}dI
\end{aligned}$$

This form of the virtual work equation provides clear separation of linear and nonlinear terms. Such separation is useful because only terms that are linear in the displacement derivatives are used in the stiffness matrix calculation. On the other hand all terms except the ones accounting for the bowing effect (fifth and tenth integrals in the virtual work equation) are used in the force recovery procedure in this work.

2.3 Fiber Element Approach

The virtual work equation presented above is applicable to a general three dimensional continuum problem. In the fiber analysis approach, several simplifying assumptions are made to obtain the one-dimensional element formulation in terms of stress resultants. Cross sections that are plane and normal to the neutral axis before deformation are assumed to remain so (Euler-Bernoulli assumption), so that shear deformation due to flexure is ignored. This allows the deformation of any point in the cross section to be expressed as a function of the deformation of the cross section centroid. This function is linearized since only small strains and incremental rotations, and moderate total rotations, are allowed in this formulation. The incremental displacements of the point with coordinates *(x, y, z)* may be expressed as:

$$\begin{aligned} \Delta u^c &= \Delta u^c_{center} - y\Delta v_{center}{}' - z\Delta w_{center}{}' \\ \Delta u^s &= \Delta u^s_{center} - y\Delta v_{center}{}' - z\Delta w_{center}{}' \\ \Delta v &= \Delta v_{center} - z\Delta\theta_x \\ \Delta w &= \Delta w_{center} + y\Delta\theta_x \end{aligned} \tag{2.8}$$

where: ' denotes differentiation with respect to x, the longitudinal element axis

$\Delta\theta_x$ is the incremental torsional rotation of the element

(u,v,w) are displacements in the directions (*x, y, z*), respectively

Another important assumption of the fiber element approach is that only longitudinal normal stress and strain components are significant. This reduces the virtual work equation from tensorial to scalar form. In particular, the constitutive tensor is replaced by a scalar material tangent modulus for both steel and concrete. The non-zero stress, strain, and constitutive tensor components are:

$$
\begin{aligned}
{}^1\tau^c_{ij} = {}^1\tau^c_{11} = {}^1\tau^c \qquad & \delta_1 e^c_{ij} = \delta_1 e^c_{xx} \\
{}^1\tau^s_{ij} = {}^1\tau^s_{11} = {}^1\tau^s \qquad & \delta_1 e^s_{ij} = \delta_1 e^s_{xx} \\
{}_1C^c_{ijkl} = {}_1C^c_{1111} = {}_1E^c \qquad & \Delta e^c_{ij} = \Delta e^c_{xx} \\
{}_1C^s_{ijkl} = {}_1C^s_{1111} = {}_1E^s \qquad & \Delta e^s_{ij} = \Delta e^s_{xx} \\
\Delta\eta^c_{ij} = \Delta\eta^c_{xx} &= \frac{1}{2}\left[\left(\Delta u'^c\right)^2 + \left(\Delta v'^c\right)^2 + \left(\Delta w'^c\right)^2\right] \\
\Delta\eta^s_{ij} = \Delta\eta^s_{xx} &= \frac{1}{2}\left[\left(\Delta u'^s\right)^2 + \left(\Delta v'^s\right)^2 + \left(\Delta w'^s\right)^2\right] \\
\delta_1\eta^c_{ij} = \delta_1\eta^c_{xx} &= \Delta u'^c \delta_1 u'^c + \Delta v'^c \delta_1 v'^c + \Delta w'^c \delta_1 w'^c \\
\delta_1\eta^s_{ij} = \delta_1\eta^s_{xx} &= \Delta u'^s \delta_1 u'^s + \Delta v'^s \delta_1 v'^s + \Delta w'^s \delta_1 w'^s
\end{aligned}
\tag{2.9}
$$

where: ${}_1E^s$ is the tangent modulus of steel

${}_1E^c$ is the tangent modulus of concrete

The virtual work equation may then be written in terms of these components (Schiller and Hajjar, 1996):

$$
\begin{aligned}
&\int_{{}^1V^c} {}_1E^c(\Delta u'^c_c - y\Delta v_c'' - z\Delta w_c'')(\delta_1 u'^c_c - y\delta_1 v_c'' - z\delta_1 w_c'')\,{}^1dV^c + \\
&\int_{{}^1V^c} {}^1\tau^c(\Delta u'^c\delta_1 u'^c + \Delta v'\delta_1 v' + \Delta w'\delta_1 w')\,{}^1dV^c + \\
&\int_{{}^1V^c} \Delta\tau^c(\Delta u'^c\delta_1 u'^c + \Delta v'\delta_1 v' + \Delta w'\delta_1 w')\,{}^1dV^c + \\
&\int_{{}^1V^s} {}_1E^s(\Delta u'^s_c - y\Delta v_c'' - z\Delta w_c'')(\delta_1 u'^s_c - y\delta_1 v_c'' - z\delta_1 w_c'')\,{}^1dV^s + \\
&\int_{{}^1V^s} {}^1\tau^s(\Delta u'^s\delta_1 u'^s + \Delta v'\delta_1 v' + \Delta w'\delta_1 w')\,{}^1dV^s + \\
&\int_{{}^1V^s} \Delta\tau^s(\Delta u'^s\delta_1 u'^s + \Delta v'\delta_1 v' + \Delta w'\delta_1 w')\,{}^1dV^s + \\
&\int_{{}^1I} \hat{k}(\Delta u^s_c - \Delta u^c_c)(\delta_1 u^s_c - \delta_1 u^c_c)\,{}^1dI = \Delta\Re
\end{aligned}
\tag{2.10}
$$

This equation can be further expanded with all displacements expressed as functions of the centerline deformations as:

$$
\begin{aligned}
&\int_{{}^1V^c} {}_1E^c \begin{pmatrix} \Delta u_c^{c\prime}\delta_1 u_c^{c\prime} - y\Delta u_c^{c\prime}\delta_1 v_c^{c\prime\prime} - y\Delta v_c^{c\prime\prime}\delta_1 u_c^{c\prime} - z\Delta u_c^{c\prime}\delta_1 w_c^{c\prime\prime} - z\Delta w_c^{c\prime\prime}\delta_1 u_c^{c\prime} + \\ yz\Delta v_c^{c\prime\prime}\delta_1 w_c^{c\prime\prime} + yz\Delta w_c^{c\prime\prime}\delta_1 v_c^{c\prime\prime} + y^2\Delta v_c^{c\prime\prime}\delta_1 v_c^{c\prime\prime} + z^2\Delta w_c^{c\prime\prime}\delta_1 w_c^{c\prime\prime} \end{pmatrix} {}^1dV^c + \\
&\int_{{}^1V^c} {}^1\tau^c \begin{pmatrix} \Delta u_c^{c\prime}\delta_1 u_c^{c\prime} - y\Delta u_c^{c\prime}\delta_1 v_c^{c\prime\prime} - y\Delta v_c^{c\prime\prime}\delta_1 u_c^{c\prime} - z\Delta u_c^{c\prime}\delta_1 w_c^{c\prime\prime} - z\Delta w_c^{c\prime\prime}\delta_1 u_c^{c\prime} + \\ yz\Delta v_c^{c\prime\prime}\delta_1 w_c^{c\prime\prime} + yz\Delta w_c^{c\prime\prime}\delta_1 v_c^{c\prime\prime} + y^2\Delta v_c^{c\prime\prime}\delta_1 v_c^{c\prime\prime} + z^2\Delta w_c^{c\prime\prime}\delta_1 w_c^{c\prime\prime} + \\ \Delta v_c^{c\prime}\delta_1 v_c^{c\prime} - z\Delta v_c^{c\prime}\delta_1\theta_x{}' - z\Delta\theta_x{}'\delta_1 v_c^{c\prime} + z^2\Delta\theta_x{}'\delta_1\theta_x{}' + \\ \Delta w_c^{c\prime}\delta_1 w_c^{c\prime} + y\Delta w_c^{c\prime}\delta_1\theta_x{}' + y\Delta\theta_x{}'\delta_1 w_c^{c\prime} + y^2\Delta\theta_x{}'\delta_1\theta_x{}' \end{pmatrix} {}^1dV^c + \\
&\int_{{}^1V^c} \Delta\tau^c \begin{pmatrix} \Delta u_c^{c\prime}\delta_1 u_c^{c\prime} - y\Delta u_c^{c\prime}\delta_1 v_c^{c\prime\prime} - y\Delta v_c^{c\prime\prime}\delta_1 u_c^{c\prime} - z\Delta u_c^{c\prime}\delta_1 w_c^{c\prime\prime} - z\Delta w_c^{c\prime\prime}\delta_1 u_c^{c\prime} + \\ yz\Delta v_c^{c\prime\prime}\delta_1 w_c^{c\prime\prime} + yz\Delta w_c^{c\prime\prime}\delta_1 v_c^{c\prime\prime} + y^2\Delta v_c^{c\prime\prime}\delta_1 v_c^{c\prime\prime} + z^2\Delta w_c^{c\prime\prime}\delta_1 w_c^{c\prime\prime} + \\ \Delta v_c^{c\prime}\delta_1 v_c^{c\prime} - z\Delta v_c^{c\prime}\delta_1\theta_x{}' - z\Delta\theta_x{}'\delta_1 v_c^{c\prime} + z^2\Delta\theta_x{}'\delta_1\theta_x{}' + \\ \Delta w_c^{c\prime}\delta_1 w_c^{c\prime} + y\Delta w_c^{c\prime}\delta_1\theta_x{}' + y\Delta\theta_x{}'\delta_1 w_c^{c\prime} + y^2\Delta\theta_x{}'\delta_1\theta_x{}' \end{pmatrix} {}^1dV^c + \\
&\int_{{}^1V^s} {}_1E^s \begin{pmatrix} \Delta u_c^{s\prime}\delta_1 u_c^{s\prime} - y\Delta u_c^{s\prime}\delta_1 v_c^{s\prime\prime} - y\Delta v_c^{s\prime\prime}\delta_1 u_c^{s\prime} - z\Delta u_c^{s\prime}\delta_1 w_c^{s\prime\prime} - z\Delta w_c^{s\prime\prime}\delta_1 u_c^{s\prime} + \\ yz\Delta v_c^{s\prime\prime}\delta_1 w_c^{s\prime\prime} + yz\Delta w_c^{s\prime\prime}\delta_1 v_c^{s\prime\prime} + y^2\Delta v_c^{s\prime\prime}\delta_1 v_c^{s\prime\prime} + z^2\Delta w_c^{s\prime\prime}\delta_1 w_c^{s\prime\prime} \end{pmatrix} {}^1dV^s + \\
&\int_{{}^1V^s} {}^1\tau^s \begin{pmatrix} \Delta u_c^{s\prime}\delta_1 u_c^{s\prime} - y\Delta u_c^{s\prime}\delta_1 v_c^{s\prime\prime} - y\Delta v_c^{s\prime\prime}\delta_1 u_c^{s\prime} - z\Delta u_c^{s\prime}\delta_1 w_c^{s\prime\prime} - z\Delta w_c^{s\prime\prime}\delta_1 u_c^{s\prime} + \\ yz\Delta v_c^{s\prime\prime}\delta_1 w_c^{s\prime\prime} + yz\Delta w_c^{s\prime\prime}\delta_1 v_c^{s\prime\prime} + y^2\Delta v_c^{s\prime\prime}\delta_1 v_c^{s\prime\prime} + z^2\Delta w_c^{s\prime\prime}\delta_1 w_c^{s\prime\prime} + \\ \Delta v_c^{s\prime}\delta_1 v_c^{s\prime} - z\Delta v_c^{s\prime}\delta_1\theta_x{}' - z\Delta\theta_x{}'\delta_1 v_c^{s\prime} + z^2\Delta\theta_x{}'\delta_1\theta_x{}' + \\ \Delta w_c^{s\prime}\delta_1 w_c^{s\prime} + y\Delta w_c^{s\prime}\delta_1\theta_x{}' + y\Delta\theta_x{}'\delta_1 w_c^{s\prime} + y^2\Delta\theta_x{}'\delta_1\theta_x{}' \end{pmatrix} {}^1dV^s + \\
&\int_{{}^1V^s} \Delta\tau^s \begin{pmatrix} \Delta u_c^{s\prime}\delta_1 u_c^{s\prime} - y\Delta u_c^{s\prime}\delta_1 v_c^{s\prime\prime} - y\Delta v_c^{s\prime\prime}\delta_1 u_c^{s\prime} - z\Delta u_c^{s\prime}\delta_1 w_c^{s\prime\prime} - z\Delta w_c^{s\prime\prime}\delta_1 u_c^{s\prime} + \\ yz\Delta v_c^{s\prime\prime}\delta_1 w_c^{s\prime\prime} + yz\Delta w_c^{s\prime\prime}\delta_1 v_c^{s\prime\prime} + y^2\Delta v_c^{s\prime\prime}\delta_1 v_c^{s\prime\prime} + z^2\Delta w_c^{s\prime\prime}\delta_1 w_c^{s\prime\prime} + \\ \Delta v_c^{s\prime}\delta_1 v_c^{s\prime} - z\Delta v_c^{s\prime}\delta_1\theta_x{}' - z\Delta\theta_x{}'\delta_1 v_c^{s\prime} + z^2\Delta\theta_x{}'\delta_1\theta_x{}' + \\ \Delta w_c^{s\prime}\delta_1 w_c^{s\prime} + y\Delta w_c^{s\prime}\delta_1\theta_x{}' + y\Delta\theta_x{}'\delta_1 w_c^{s\prime} + y^2\Delta\theta_x{}'\delta_1\theta_x{}' \end{pmatrix} {}^1dV^s + \\
&\int_{{}^1I} \hat{k}(\Delta u_c^s\delta_1 u_c^s - \Delta u_c^c\delta_1 u_c^s - \Delta u_c^s\delta_1 u_c^c + \Delta u_c^c\delta_1 u_c^c)\,{}^1dI = \Delta\Re
\end{aligned}
\tag{2.11}
$$

2.4 Fiber Discretization and Interpolation Functions

In a finite element formulation all quantities at any point are functions of the corresponding quantities at the element nodes. A set of interpolating functions is used to prescribe variation of element parameters between the nodal points. In a fiber element formulation, only interpolation along the length is needed, since the beam-column is

modeled as a line element with cross-sectional properties varying along its length. This element coincides with a centerline of a beam-column, with all deformations of an arbitrary point on the cross section related to those of the centerline by the linear kinematic assumptions of Eq. 2.8.

Each volume integral appearing in the virtual work equation may be separated into an integral over the cross-sectional area and an integral along the element length. The cross section is discretized into a grid of fibers, and all integrals over the cross section are evaluated by numerical integration, with the contribution of each fiber added to the total sum. Integrals along the length are calculated analytically, since only simple polynomial functions are chosen for interpolating functions.

Interpolation functions are used to specify the variations of element deformations, stress resultants (forces and moments), and rigidities (Schiller and Hajjar, 1996). Cubic Hermitian polynomials are used to describe the transverse deformations and rotations of the element. They are exact for the first order description of the linear elastic element having constant flexural rigidity and no axial force, but for any other case are only approximate. Torsional rotation of the element is described by a linear function. Longitudinal displacements are interpolated using a quadratic function. This requires an additional mid-element node whose DOFs are removed from the stiffness matrix using static condensation. The total axial force is assumed to be constant for the element, while the axial forces in both steel and concrete may vary linearly, so that axial force may be transferred between the steel and concrete through the slip interface. The torque is assumed to be constant along the length, while all other stress resultants are assumed to vary linearly between the element ends. Axial, flexural, and torsional rigidities of the elements may vary linearly.

When the interpolation functions are substituted into the virtual work equation and integration along the length is carried out, the resulting expression involves only nodal degrees-of-freedom, nodal force increments, and numerous area integrals listed below:

$$
\begin{aligned}
&\int_{1A^c} {}^1E^c\,{}^1dA = \sum_f \left({}^1E^c\,{}^1A\right)_f = EA^c && \int_{1A^s} {}^1E^s\,{}^1dA = \sum_f \left({}^1E^s\,{}^1A\right)_f = EA^s \\
&\int_{1A^c} {}^1E^c\,y^1dA = \sum_f \left({}^1E^c\,y^1A\right)_f = -EQ^c{}_z && \int_{1A^s} {}^1E^s\,y^1dA = \sum_f \left({}^1E^s\,y^1A\right)_f = -EQ^s{}_z \\
&\int_{1A^c} {}^1E^c\,z^1dA = \sum_f \left({}^1E^c\,z^1A\right)_f = -EQ^c{}_y && \int_{1A^s} {}^1E^s\,z^1dA = \sum_f \left({}^1E^s\,z^1A\right)_f = -EQ^s{}_y \\
&\int_{1A^c} {}^1E^c\,y^{21}dA = \sum_f \left({}^1E^c\,y^{21}A\right)_f = EI^c{}_{zz} && \int_{1A^s} {}^1E^s\,y^{21}dA = \sum_f \left({}^1E^s\,y^{21}A\right)_f = EI^s{}_{zz} \\
&\int_{1A^c} {}^1E^c\,z^{21}dA = \sum_f \left({}^1E^c\,z^{21}A\right)_f = EI^c{}_{yy} && \int_{1A^s} {}^1E^s\,z^{21}dA = \sum_f \left({}^1E^s\,z^{21}A\right)_f = EI^s{}_{yy} \\
&\int_{1A^c} {}^1E^c\,yz^1dA = \sum_f \left({}^1E^c\,yz^1A\right)_f = EI^c{}_{yz} && \int_{1A^s} {}^1E^s\,yz^1dA = \sum_f \left({}^1E^s\,yz^1A\right)_f = EI^s{}_{yz} \\
&\int_{1A^c} {}^1\tau^c\,{}^1dA = \sum_f \left({}^1\tau^c\,{}^1A\right)_f = P^c && \int_{1A^s} {}^1\tau^s\,{}^1dA = \sum_f \left({}^1\tau^s\,{}^1A\right)_f = P^s \\
&\int_{1A^c} {}^1\tau^c\,y^1dA = \sum_f \left({}^1\tau^c\,y^1A\right)_f = -M^c{}_z && \int_{1A^s} {}^1\tau^s\,y^1dA = \sum_f \left({}^1\tau^s\,y^1A\right)_f = -M^s{}_z \\
&\int_{1A^c} {}^1\tau^c\,z^1dA = \sum_f \left({}^1\tau^c\,z^1A\right)_f = -M^c{}_y && \int_{1A^s} {}^1\tau^s\,z^1dA = \sum_f \left({}^1\tau^s\,z^1A\right)_f = -M^s{}_y \\
&\int_{1A^c} {}^1\tau^c\,y^{21}dA = \sum_f \left({}^1\tau^c\,y^{21}A\right)_f = \zeta^c{}_{zz} && \int_{1A^s} {}^1\tau^s\,y^{21}dA = \sum_f \left({}^1\tau^s\,y^{21}A\right)_f = \zeta^s{}_{zz} \\
&\int_{1A^c} {}^1\tau^c\,z^{21}dA = \sum_f \left({}^1\tau^c\,z^{21}A\right)_f = \zeta^c{}_{yy} && \int_{1A^s} {}^1\tau^s\,z^{21}dA = \sum_f \left({}^1\tau^s\,z^{21}A\right)_f = \zeta^s{}_{yy} \\
&\int_{1A^c} {}^1\tau^c\,yz^1dA = \sum_f \left({}^1\tau^c\,yz^1A\right)_f = \zeta^c{}_{yz} && \int_{1A^s} {}^1\tau^s\,yz^1dA = \sum_f \left({}^1\tau^s\,yz^1A\right)_f = \zeta^s{}_{yz}
\end{aligned}
\tag{2.12}
$$

$$
\int_{1I} \hat{k}(\Delta u_c^s - \Delta u_c^c)(\delta_1 u_c^s - \delta_1 u_c^c)^1 dI =
$$

$$
\int_{1L} \rho \cdot \hat{k}(\Delta u_c^s - \Delta u_c^c)(\delta_1 u_c^s - \delta_1 u_c^c)^1 dx = \int_{1L} k(\Delta u_c^s - \Delta u_c^c)(\delta_1 u_c^s - \delta_1 u_c^c)^1 dx
$$

where: k is a calibrated constant value of slip stiffness per unit length of interface, (units of force/length^2), such that $\hat{k} = k/\rho$

ρ is the perimeter of the tube

These integrals are approximated by sums over all the fibers, *f*, in the cross section. They involve displacements of power less than or equal to two, which results from the choice of polynomial interpolation functions. These integrals constitute the

element rigidities and stress resultants (axial force, bending moment, and higher order stress moments). All rigidity integrals constitute moments of the area (area, first moment of the area, and moment of inertia) multiplied by the material tangent modulus at the last converged configuration C1, which may change from fiber to fiber within a cross section. Stress resultant integrals do not have explicit tangent modulus dependence, but involve the values of stresses, which may also change between fibers.

2.5 Tangent Stiffness Calculations

An incremental/iterative solution is used in this work (Schiller and Hajjar, 1996). Using the incremental virtual work equation, the stress resultant increment may be expressed as:

$$\Delta F = K \cdot \Delta d + \varphi(\Delta d) \tag{2.13}$$

where: ΔF is the vector of element stress resultant increments

Δd is the vector of nodal displacement increments

K is the element tangent stiffness matrix

$\varphi(\Delta d)$ is a nonlinear function of the nodal displacement increments

The element tangent stiffness matrix may be separated into a small displacement matrix and a geometrically nonlinear matrix. The terms of the small displacement stiffness matrix include rigidities calculated by summation over the fibers, so that they depend on the values of fiber tangent moduli, but are independent of stress resultants. The terms of the geometrically nonlinear stiffness matrix are linear functions of the stress resultants, calculated by summing the contributions of individual fibers in a cross section. The explicit form of the 18 DOF element stiffness matrices is given in Appendix A of (Schiller and Hajjar, 1996).

The linearized element stiffness matrices are assembled into the global stiffness matrix which is used to calculate a prediction of the global displacement increments, given a global out-of-balance load vector. For a particular level of applied load, the out-of-balance load vector is calculated as the difference between the applied load and the internal force vector. For this analysis procedure, the Newton-Raphson method is used within each applied load increment. The tangent stiffness matrix and the internal force vector are updated at every iteration. This process is repeated iteratively until the convergence is reached, so that the out-of balance load vector becomes smaller than a prescribed tolerance.

Thus, the accuracy of the displacement increment prediction directly depends on the accuracy of the stiffness matrix calculation. As discussed previously, element tangent stiffness matrices are computed using the values of material tangent modulus in each fiber and values of fiber stresses. Thus, the material models must be capable of predicting both the tangent modulus and the stress level with a high degree of accuracy to obtain a good prediction of incremental displacements. It should be noted that the quality of the tangent stiffness matrix usually does not affect the obtained structural response as long as the Newton-Raphson iterations converge. On the other hand, the convergence rate is greatly affected by the tangent stiffness matrix accuracy. Thus obtaining a good approximation of tangent stiffness of the structure is desirable.

2.6 Force Recovery

Unlike tangent stiffness prediction, force recovery utilizes integrals of the virtual work equation that are nonlinear in the displacement increments, together with the linear terms. The element elongation is computed directly from the end-of-iteration nodal displacements, and it in turn is used to calculate the incremental axial forces. The values

of these incremental axial forces are used to update the tangent stiffness matrix, which is used to calculate incremental nodal forces:

$$\Delta F = K \cdot \Delta d \tag{2.14}$$

where: ΔF is the vector of incremental element forces

Δd is the vector of nodal displacement increments

K is the element end-of-iteration tangent stiffness matrix

This technique accounts for the change of axial force during the load step, so that the contribution of the third and sixth integrals of Eq. 2.11 are included (Morales, 1994; Schiller and Hajjar, 1996).

Element strains are often computed from the element nodal displacements using the interpolation functions. However, this approach has several disadvantages for the current formulation. First, it would require calculation of the midpoint axial displacement, eliminating the benefit of its static condensation. Second, it may produce discontinuous strain fields, since derivatives of the interpolation functions need not be continuous on the element boundaries, particularly if the element rigidities are varying along the length. Third, the interpolation functions are exact only for the prismatic elastic element. As soon as spread of plasticity begins, the interpolation functions provide a less accurate solution for the displacements. Moreover, the strains calculations will be even less accurate, since the strains are calculated from the interpolation functions derivatives.

An alternative technique of strain recovery uses recovered incremental forces to compute strains (White, 1985). This approach takes into account partial plastification of the element. Fiber stress is related to the fiber strains through constitutive equations, and element end forces are calculated by numerical integration of fiber stresses in a cross section. Thus, initial estimates of the element end-of-iteration end forces may be expressed in terms of the fiber centroidal strains as:

$$
\begin{aligned}
\Delta P^c &= \int_{A_f^c} \Delta\tau^c dA^c = \int_{A_f^c} E^c \Delta u'^c \, dA^c = \int_{A_f^c} E^c \left(\Delta u'^c_c - y\Delta v''_c - z\Delta w''_c\right) dA^c \\
&= EA^c \Delta u'^c_c + EQ_z^c \Delta v''_c + EQ_y^c \Delta w''_c \\
\Delta P^s &= \int_{A_f^s} \Delta\tau^s dA^s = \int_{A_f^s} E^s \Delta u'^s \, dA^s = \int_{A_f^s} E^s \left(\Delta u'^s_c - y\Delta v''_c - z\Delta w''_c\right) dA^s \\
&= EA^s \Delta u'^s_c + EQ_z^s \Delta v''_c + EQ_y^s \Delta w''_c \\
\Delta M_z &= -\int_{A^{tot}} y\Delta\tau^c dA^c + y\Delta\tau^s dA^s = -\int_{A_f^s} y_1 E^s \Delta u'^s \, dA^s - \int_{A_f^c} y_1 E^c \Delta u'^c \, dA^c \\
&= \int_{A_f^s} E^s \left(-y\Delta u'^s_c + y^2 \Delta v''_c + yz\Delta w''_c\right) dA^s + \int_{A_f^c} E^c \left(-y\Delta u'^c_c + y^2 \Delta v''_c + yz\Delta w''_c\right) dA^c \\
&= EQ_z^c \Delta u'^c_c + EQ_z^s \Delta u'^s_c + EI_{zz}^{s+c} \Delta v''_c + EI_{yz}^{s+c} \Delta w''_c \\
\Delta M_y &= -\int_{A^{tot}} z\Delta\tau^c dA^c + z\Delta\tau^s dA^s = -\int_{A_f^s} z_1 E^s \Delta u'^s \, dA^s - \int_{A_f^c} z_1 E^c \Delta u'^c \, dA^c \\
&= \int_{A_f^s} E^s \left(-z\Delta u'^s_c + yz\Delta v''_c + z^2 \Delta w''_c\right) dA^s + \int_{A_f^c} E^c \left(-z\Delta u'^c_c + yz\Delta v''_c + z^2 \Delta w''_c\right) dA^c \\
&= EQ_y^c \Delta u'^c_c + EQ_y^s \Delta u'^s_c + EI_{yz}^{s+c} \Delta v''_c + EI_{yy}^{s+c} \Delta w''_c
\end{aligned}
\tag{2.15}
$$

It can be seen that incremental end forces are linear functions of the centerline strains. If integration is carried out, the coefficients of these functions become cross-sections rigidities introduced earlier (Eq. 2.12). Thus, the relation between the element end incremental forces and the centroidal strain increments can be written in matrix form as:

$$
\begin{Bmatrix} \Delta P^c \\ \Delta P^s \\ \Delta M_z \\ \Delta M_y \end{Bmatrix} = \begin{bmatrix} EA^c & 0 & EQ_z^c & EQ_y^c \\ 0 & EA^s & EQ_z^s & EQ_y^s \\ EQ_z^c & EQ_z^s & EI_{zz}^{s+c} & EI_{yz}^{s+c} \\ EQ_y^c & EQ_y^s & EI_{yz}^{s+c} & EI_{yy}^{s+c} \end{bmatrix} \begin{Bmatrix} \Delta u'^c_c \\ \Delta u'^s_c \\ \Delta v''_c \\ \Delta w''_c \end{Bmatrix} \tag{2.16}
$$

This system may be solved for the centroidal incremental strains provided that the coefficient matrix is nonsingular. Since the elements of this cross-section stiffness matrix are obtained using the tangent moduli of cross-section fibers, this procedure accounts for the partial plastification of the cross-section. The accuracy of the strain calculation depends on the accuracy of fiber tangent moduli predicted by the material models.

These centroidal strain increments are used to calculate the strain increment for all of the cross-section fibers using the kinematic relations of Eq. 2.8. Knowing the strain

increment for each fiber, a stress increment may be predicted by the material models, and the total stress and tangent modulus may be updated. These updated values are used to calculate cross-section rigidities utilized in the subsequent tangent stiffness matrix calculation and force recovery procedure.

For the incremental-iterative solution procedure used in this work, there are two possible approaches to calculating the incremental strain, stress, displacement, and force quantities at each iteration (Crisfield, 1991). The first approach is to use iterative strains calculated from iterative displacements, calculate iterative stresses from iterative strains, and add these stresses to the beginning-of-iteration stresses. The second approach is to update incremental displacements using iterative displacements, calculate incremental strains from incremental displacements, compute incremental stresses from incremental strains, and add these stresses to the beginning-of-increment stresses. While the first approach may be computationally more efficient in some cases, it can lead to 'spurious unloading' since the reference beginning-of-iteration state may not correspond to any actual state experienced by the material. On the other hand, the second approach uses the converged beginning-of-increment equilibrium state as the reference, thus following the material loading path more accurately. The second approach is used consistently for this research, with all quantities referenced to the converged beginning-of-increment state.

In order to increase the robustness of the formulation, material nonlinearity is not considered in the unbalanced load calculation for the Newton-Raphson iterative solution. Additionally, all external load are applied at the steel degrees-of-freedom and end-of-step forces computed in the force recovery procedure are assembled at steel degrees-of-freedom only. This approach does not affect the solution accuracy, but ensures stable convergence of the unbalanced forces in the iterative process (Schiller and Hajjar, 1996).

Chapter 3

Cyclic Steel Plasticity Model

3.1 Cyclic Behavior of CFT Beam-Columns

The primary goal of this research is to comprehensively model the behavior of CFT elements and structures on the force-deformation level. While capturing the corresponding stress-strain behavior of both steel and concrete is an essential step of modeling, some of the stress level phenomena may be modeled in an approximate or average sense only, as long as the overall structural behavior is captured sufficiently well by the model. Therefore, the requirements for the steel and concrete constitutive models on the stress-strain level must be selected by identifying the key behavioral characteristics of the structural response of CFTs on the force-deformation level. Figure 3.1 illustrates typical behavior of a CFT beam-column subjected to cyclic loading, showing the load-deformation response of a square CFT beam-column tested by Sakino and Tomii (1981). A schematic illustration of the test setup is shown in the inset. The specimen was subjected to a constant axial load, $P = 0.3P_o$ ($P_o = 528$ kN), and a cyclic shear loading, Q, applied nonproportionally for three full cycles at each increasing increment of chord rotation, R, which was varied from 0.5% to 2.5%.

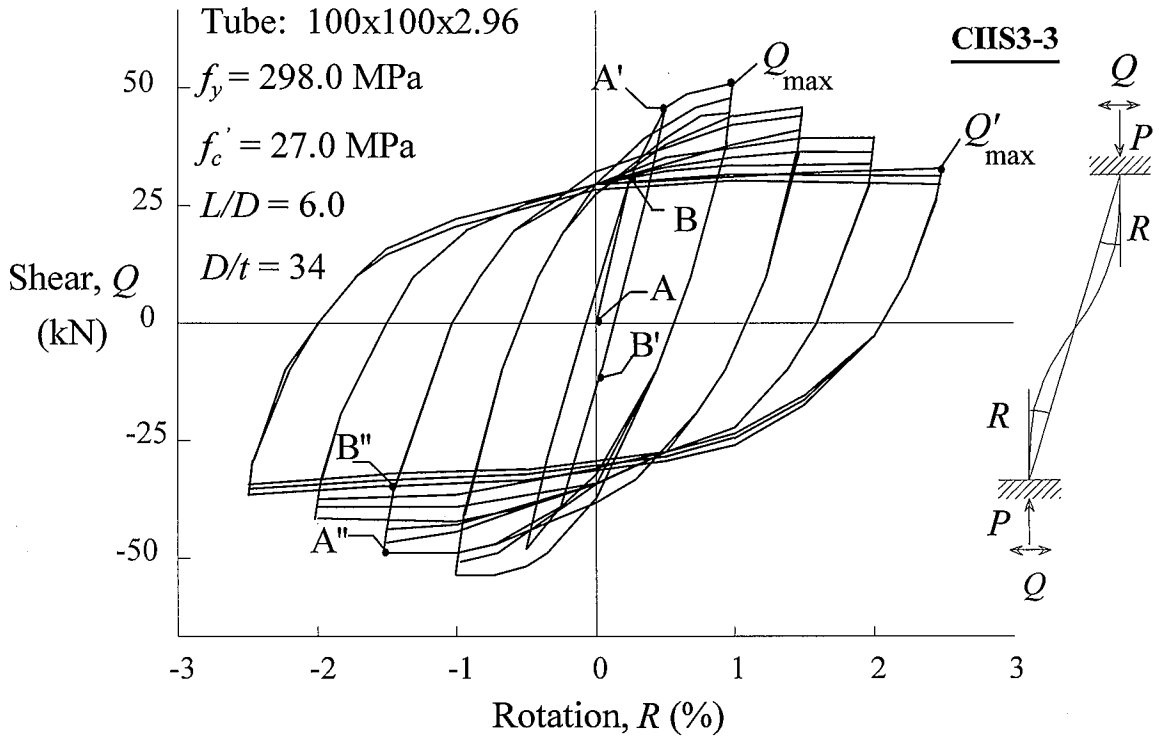

Figure 3.1: Typical Cyclic Behavior of a CFT Beam-Column

The main behavioral features which can be observed in this experiment and which must be modeled include:

1. *Elastic unloading*: CFTs unload elastically, such that the stiffness at the load reversal is nearly equal to the stiffness of a virgin specimen. However, the elastic stiffness degrades somewhat due to the concrete crushing after the first half-cycle of loading before reaching a nearly constant value (e.g., compare the stiffness of segment AB to that of segment A'B' in Fig. 3.1).
2. *Decreasing elastic zone*: The size of the "elastic zone" of a CFT reduces with cyclic loading, mainly due to steel local buckling and concrete crushing, as well as to the reduction in size of the elastic zone of the steel material. Eventually, the elastic zone stabilizes at a non-zero value (this is seen in comparing segments AB and A"B" in Fig. 3.1).
3. *Strength degradation*: The maximum strength achieved within each hysteretic cycle degrades as the analysis proceeds, due primarily to local buckling of the steel tube

and to damage of the concrete (compare peaks Q_{max} to Q'_{max} in Fig. 3.1). However, in the earliest cycles of loading, the experiments of Sakino and Tomii (1981) show that an increase of CFT capacity beyond the nominal monotonic strength is sometimes observed. This increase may be attributed to steel cyclic hardening, or to the structure being stiffer than expected due to support fixity in the experiments.

4. *Bauschinger effect*: The Bauschinger effect typically exhibited at the stress level by the steel tube is seen in Fig. 3.1 to propagate to the stress-resultant level of a CFT.
5. *Gradual stiffness reduction*: During a loading excursion, the stiffness of a CFT reduces gradually from its initial elastic value, due to both geometric and material nonlinearity, as evidenced in each cycle in Fig. 3.1.
6. *Bounding stiffness*: CFTs exhibit a limiting bounding stiffness, which may be seen most clearly in the last two hysteretic cycles in Fig. 3.1. The bounding stiffness evolves due to the stabilization of the steel tube, even after local buckling (Sakino and Tomii, 1981).

This stress-resultant behavior exhibits the cumulative effects of material nonlinearity at the stress-point level in both the steel and concrete, coupled with the effects of geometric nonlinearity of the member. Thus, this key stress-resultant behavior must be reflected in the cyclic stress-strain models of the steel and concrete.

3.2 Characteristic Features of Tube Steel

Behavior of structural steel under monotonic and cyclic loading has been documented by many researchers and will not be described here. However, the features that are specific to the cold formed steel used for steel tubes will be briefly reviewed here.

It is customary to idealize the stress-strain curve of a steel specimen as consisting of an elastic zone followed by an elasto-plastic zone. The stress is proportional to the strain in the elastic zone, which is assumed to terminate when the initial yield stress of the

material is reached, while in fact a stress level where the deviation from the proportional relation becomes noticeable is always below the yield stress. This early departure from linearity has often been neglected in applications and most classical plasticity theories. For design purposes the proportional limit and the yield limit defined by some value of the residual plastic strain are almost always assumed to coincide. This is a good approximation for hot-rolled structural shapes, and its use can significantly simplify calculations. On the other hand, for cold worked shapes, and structural tubes in particular, this approximation may be inaccurate, especially if the material does not posses a well defined yield point. Tests of tube stub-columns showed the proportional limit to be only one-fourth to one-third of the yield limit defined at the 0.2% offset (Lu and Kennedy, 1994). The strain-stress curves obtained in these tests did not have a yield plateau region. Another set of tests shows the proportional limit to be less than a half of the yield limit (Zhao and Hancock, 1993), even for the specimens showing a well defined yield point.

Stress-strain curves obtained by testing the coupons cut from the cold-formed steel hollow sections generally are rounded (Masuo et al., 1991; Clarke, 1992; Sully and Hancock, 1994). They do not posses a well defined yield stress or the sharp transition from the yield plateau to strain hardening region. The distinct yield plateau, typical for mild steel of hot-rolled shapes, is not characteristic of material curves of cold-formed shapes (Clarke, 1992). Consequently, the yield stress for this type of steel is defined as the stress corresponding to a 0.2% offset of strain.

Another characteristic feature of the cold-formed sections is the nonuniform distribution of material properties. It has been observed that for rectangular tubes, the flat flange regions possess fairly uniform material properties, while the corner regions exhibit enhanced strength and reduced ductility. The relative difference between the yield strength of the coupons cut from the corner section, and the coupons cut from the flat region was reported to have an average value of 34% by (Clarke, 1992). This difference was found to vary from 20% to 32% in another investigation (Key et al., 1988). Similar results were also reported in (Sully and Hancock, 1996).

Cold-worked tubes usually have significant residual stresses induced by the manufacturing process. Residual stresses at any point in the tube may be in the longitudinal, circumferential, or radial (through the tube thickness) directions. Residual stresses may also be identified by their distribution through the thickness of a steel tube: membrane stresses, which are mean values of stresses oriented in the longitudinal or circumferential directions, obtained by averaging their values across the tube thickness; and through-thickness stresses, which represent the variation of the residual stresses through the thickness of the tube wall. Both longitudinal and radial stresses have a nonlinear distribution profile through the tube wall thickness, and are highly dependent on the details of the manufacturing process (Sherman, 1992). Longitudinal residual stresses may be as high as 80 percent of the yield stress of the material; however they vary across the thickness from tension to compression, so that the resulting membrane residual stresses have relatively low values and are not modeled in this work (Sherman, 1992). Through-thickness residual stresses may have values exceeding the yield stress (Bridge, 1976), and are more appropriately thought of as residual strains (Sherman, 1992). Since the through-thickness residual strains are present in the tensile coupons that are cut out of the steel tube and used to obtain the stress-strain curve, the uniaxial stress-strain curve implicitly accounts for their presence by the change in the proportional and yield limits (Sully and Hancock, 1996). Therefore, through-thickness residual stresses need not be explicitly considered in the modeling of the steel behavior if the model is calibrated to the stress-strain curve obtained by testing a coupon cut from the cold-formed section. In addition, tubes with welded seams may also have high circumferential residual stresses due to welding process, but their effect is localized in the weld vicinity (Sherman, 1992).

3.3 Required Properties of the Steel Plasticity Model

A constitutive material model must describe the salient features of material response. Thus, a cyclic plasticity model must be capable of representing the typical phenomena observed experimentally on the stress-strain level that significantly affect the behavior exhibited by CFT beam-columns on the structural level.

A set of requirements for steel cyclic plasticity models was formulated by Drucker and Palgen (Drucker and Palgen, 1981) and subsequently expanded upon by Dafalias (Dafalias, 1992). These requirements are:

1. Extensive plastic loading of almost fixed direction overwhelms and wipes out many of the past history effects, if not all.
2. Under symmetric stress or strain cycles, the material hardens or softens towards a stabilized state with only kinematic hardening, depending on the initial annealed or cold-worked state.
3. Unsymmetric stress cycles will cause plastic creep in the direction of mean stress.
4. Unsymmetric strain cycles will cause progressive relaxation to zero mean stress.
5. The model must predict as accurately as possible the variation of the plastic modulus (and therefore the slope of the stress-strain curves) during random cyclic loading.

In common plasticity formulations, isotropic hardening refers to the change of a plasticity surface size, often used to capture cyclic hardening or softening, changes in the size of the elastic zone, and other phenomena. Kinematic hardening refers to the change of the surface position, often used to capture the Bauschinger effect (Khan and Huang, 1995).

The first requirement is often discussed in terms of fading versus nonfading memory of the material. It states that fading memory governs the material behavior. This suggests using a set of discrete parameters, often called plastic internal variables (Dafalias and Popov, 1976), determine the current plastic state of the material. Such

parameters may change discontinuously even for a continuous change in stress or strain to reflect the effect of "wiping out" the past history effects. Such discontinuous changes are referred to as update procedures.

The second requirement reflects the experimentally observed stabilization of the stress-strain curves to a cyclic curve corresponding to a given strain range. For a cold formed steel section usually only a limiting amount of cyclic hardening is observed. This requirement does not account for possible nonproportionality of loading.

The third and fourth requirements state the general behavioral trends observed experimentally. Due to unsymmetric response exhibiting by the concrete core in tension-compression cycling, both stress and strain ranges for a particular steel fiber are likely to be unsymmetric, even for a symmetric loading program. It should be noted here that the rates of both ratchetting (cyclic creep) and mean stress relaxation are comparatively low for structural steel.

The fifth requirement, added by Dafalias, is especially important for earthquake applications, where loading produced by the ground motion is essentially random.

The recommendations above should be augmented by several additional requirements reflecting recent experimental observations (Lee et al., 1992). These additional requirements are:

6. The mean strain value does not affect material behavior for both proportional and nonproportional straining.
7. Elastic stress range reduces with the increase of the maximum strain range, and this reduction saturates for large strain ranges.

The sixth requirement may be contrasted with the fact that the mean stress value affects the behavior significantly, as stated in the third and fourth requirements (Dafalias, 1992). The seventh requirement, reflecting fairly recent observations (Lee et al., 1992), is

in disagreement with several existing models (Chang and Lee, 1986), postulating that the elastic stress range remains constant.

The last group of requirements is specific to modeling cold form steel (i.e., a steel tube):

8. A smooth elasto-plastic transition zone with the proportional limit significantly lower than the yield limit must be modeled.
9. A variation of material properties across the cross-section should be accounted for by a gradual change of model parameters within the framework of the plasticity model.

The eighth requirement specifies a characteristic feature of cold-formed structural steel: a rounded shape of a stress-strain curve. It emphasizes that the limit of elastic behavior is reached much earlier than a yield stress customarily defined by some value of plastic strain (i.e., 0.2%). The ninth requirement reflects the experimental observations that the mechanical properties of cold-formed steel sections vary appreciably along the perimeter (Sherman, 1992; Sully and Hancock, 1996).

3.4 Overview of Cyclic Plasticity Models

Several types of the plasticity formulations suitable for modeling steel behavior are described here. The presentation progresses from basic models to more advanced formulations, and culminates with the description of the cyclic bounding surface plasticity model implemented in the fiber analysis as part of this research. The purpose of this presentation is to describe the important features of the plasticity models and to justify the selection of the final model for this research.

3.4.1 Linear Kinematic Hardening

Prager model (Prager, 1956) is the simplest kinematic hardening model. This model has a single yield surface, and it assumes that the increment of the backstress (i.e., the origin of the yield surface) is proportional to the plastic strain increment. The yield surface translates kinematically, without changing its size or shape, in the direction of the normal to the yield surface at the current stress point. This model predicts the Bauschinger effect, but cannot predict many other important phenomena such as ratchetting, mean stress relaxation, and a gradual elasto-plastic transition. An abrupt change of the plastic modulus at the yield limit does not describe a gradual elasto-plastic transition, so that the shape of the hysteresis loops may not be predicted well by this model. The Prager model is implemented as a simple alternative cyclic plasticity model in this research.

3.4.2 Modern Cyclic Plasticity Models

All modern cyclic plasticity models can be classified as (Chaboche, 1986; Khan and Huang, 1995):

1. Models where the present state of the material depends on the present values and the past history of observable variables. This approach gives rise to various hereditary theories, most notably the endochronic theory of plasticity (Valanis, 1971), as well as several similar theories of viscoplasticity.
2. Models where the present state of the material depends on the present values of observable variables and a set of internal state variables (plastic internal variables) only. This second approach can be considered a generalization of classic models

of isotropic and kinematic hardening. Various types of models following this approach can be further classified as:

a) Multilayer models.
b) Multisurface models.
c) Infinite number of surfaces models.
d) Two surface (bounding surface) models.
e) One surface models with yield surface reduced to a single point.
f) Nonlinear kinematic hardening models.

Mathematically the first approach is implemented by explicitly specifying a functional relating the stress and strain tensors. Use of a functional rather than a function reflects the dependence on the past history of observable variables.

The second approach is mathematically expressed by specifying the relation between infinitesimal increments of the stress and strain tensors. Dependence on the past history is expressed by continuous updating of a set of plastic internal variables. These variables are in general expressed as functions of the current values of the strain tensor and other internal variables. Thus, a linear or nonlinear function relating the stress rate and the strain rate and a system of coupled differential equations which expresses the internal state variables constitute the most general formulation of a plasticity model. These equations must be homogeneous first order differential equations in order to define a rate independent model (Khan and Huang, 1995).

It has been shown that these two approaches are closely related (Khan and Huang, 1995), and formulation utilizing one of them may often be expressed in terms of the other. Currently, the approach specifying the incremental stress-incremental strain relation as a function of the internal variables is dominant in the field of rate independent plasticity models for metals, and this approach was chosen for the current research.

Within the framework of incremental plasticity, nonlinear kinematic hardening and bounding surface formulations are the most popular for modeling cyclic plasticity of

metals. For modeling structural steel response, the bounding surface formulation has been used extensively by many researchers (e.g., Dafalias and Popov, 1975; Chang and Lee, 1986; White, 1987; Shen, 1993). It has the advantages of easy interpretation in terms of the interacting plasticity surfaces, and of the ability to model the limiting (bounding) slope of the stress-strain curve directly. The bounding surface cyclic plasticity formulation has been implemented in current research as the primary material model for steel tubes.

3.5 Bounding Surface Plasticity Models

Bounding surface models were developed to explicitly model the experimental observation that the modulus of a uniaxial steel specimen subjected to random cyclic loading attains a bounding value (Dafalias and Popov, 1975). This characteristic of the steel behavior propagates to the structural level, manifesting itself in the bounding slope of the force-deformation response of CFTs (see Section 3.1). The bounding stiffness is a salient feature of CFT response; thus, accurate modeling of the bounding modulus of steel fibers is important. The bounding surface plasticity models account for the bounding modulus of the material explicitly, and thus are well suited for the purpose of this research.

The bounding surface model consists of an inner loading surface and an outer bounding surface in multiaxial stress space. Elastic behavior is presumed when the stress point is within the loading surface. Once the stress points contacts the loading surface, the plastic modulus of the steel begins to decrease. To each point on the yield surface corresponds a so-called "image point" or "conjugate point" on the bounding surface. The plastic modulus is postulated to be a function of the metric distance between the current stress point and the image point, and possibly some plastic internal variables. A set of hardening rules is prescribed for both the loading and bounding surfaces, so that each surface may experience both isotropic and kinematic hardening.

The plastic modulus changes from infinity at the start of plastic loading to some limiting value. This provides for a smooth elasto-plastic transition at the initiation of the plastic loading. The limiting value is attained only when the current stress points lies on the bounding surface. The image point on the bounding surface is often defined by the Mroz rule (Khan and Huang, 1995), which means that the image point has the same direction of external normal as the current stress point on the loading surface. The plastic modulus is commonly taken to be a function of the metric distance between the current stress point and the image point, δ, and the value of that distance at the most recent initiation of plastic flow, δ_{in}, called the initial plastic distance (Dafalias and Popov, 1975). The initial plastic distance is a discrete parameter that is changed only when the current loading point first contacts the loading surface. It does not change as long as the stress point remains on the loading surface, even though the direction of plastic loading may change for a multiaxial loading program. The plastic modulus is calculated as (Dafalias and Popov, 1975):

$$K^p = \frac{2}{3}(E_0^p + h \cdot (\frac{\delta}{\delta_{in} - \delta})) \tag{3.1}$$

where: E_0^p is the slope of the bounding line (bounding slope)

h is a shape parameter

The shape parameter h is selected to fit data obtained from cyclic experiments.

The versatility of the bounding surface model follows from its ability to specify the constitutive relations on two levels (Dafalias, 1992). On the first level, the isotropic and kinematic hardening rules specify the evolution of the loading surface, and the bounding plastic modulus is obtained from uniaxial cyclic experiments. On the second level, the plastic modulus is obtained as, for example, $K^p = K_0^p + h \cdot \frac{\delta}{(\delta_{in} - \delta)}$. Then, when either the isotropic or kinematic hardening rules is specified, the evolution of the bounding surface is completely determined. Only one hardening rule (isotropic or

kinematic) may be specified for the bounding surface, since the other one is determined be the plastic modulus and the consistency condition written for the bounding surface. These two levels of modeling permit direct calibration of the tangent elasto-plastic modulus of steel to the experimental results, while allowing almost any kinematic and isotropic hardening rule to be incorporated into the model.

While the bounding surface model is versatile and general, it has several shortcomings. The most important of them is the so called overshooting phenomenon, which is the most pronounced for uniaxial loading. It manifests itself in predicting the unrealistically stiff response for plastic loading following a small amount of plastic loading in the reverse direction (LeMaitre and Chaboche, 1990). The stiffness of the response is caused by the requirement for the plastic modulus to be infinite at the initiation of plastic loading. If, for example, a plastic loading is followed by an elastic unloading, and then by a reloading in the original direction, the initial plastic distance is, typically, not updated, and the response predicted is close to that which would be obtained in the absence of the unloading. This is the response obtained experimentally, so that the model prediction in this case is satisfactory. If, on the other hand, the plastic loading is followed by unloading including a small excursion into the plastic range, then a subsequent reloading in the original direction uses an updated value of the initial plastic distance, since a drastic change of the plastic loading direction has taken place. This update causes the model to predict stresses significantly higher than those obtained if there were no unloading. Thus, the reloading curve overshoots the original loading curve. While the amount of overshooting is controlled to some extent by the gradual decrease in modulus as the stress points approach the bounding surface, it is seen as an undesirable feature of the model (Dafalias, 1986), and special care is often taken to minimize its effect.

Another undesirable feature of common bounding surface plasticity models is prediction of excessive ratchetting (plastic creep). While some ratchetting is observed experimentally, and the ability to predict this phenomenon is essential for cyclic plasticity models (as stated in the third requirement in Section 3.3), many existing bounding surface

models predict a significantly greater amount of ratchetting than is observed experimentally (Hashiguchi, 1993).

3.6 Nonhardening Region Models

The concept of equivalent plastic strain has been utilized in a variety of ways in many plasticity models to provide a convenient way of relating the hardening rules in multiaxial stress space to the uniaxial stress-strain curve, which can relate stress directly to uniaxial plastic strain. While useful for modeling monotonic behavior, this concept is less amenable to cyclic plasticity models. An alternative approach, originating from uniaxial plasticity models (Mizuno et al., 1992), is using the maximum plastic strain ever achieved during the entire deformation history as a model parameter (Ohno, 1982). One means of utilizing this parameter is to specify the isotropic hardening rule for a loading surface using the parameter. Another way is to consider a range between the minimum and the maximum values of plastic strain and relate it to the occurrence of cyclic hardening. For example, since experiments show little or no cyclic hardening until the previously reached value of maximum plastic strain is exceeded, a concept of a nonhardening strain range has been proposed (Chaboche et al., 1979). It postulates that for uniaxial loading there exists a plastic strain range such that no hardening occurs if plastic strain produced during the loading cycle falls within this range. This range increases as the plastic strain exceeds its previous maximum value. For the multiaxial case, this concept may be generalized to a plastic strain range, enclosed by a limiting surface (Ohno, 1982). It is called a nonhardening surface because the plastic deformation occurring while the current stress point is inside the surface does not contribute to the accumulation of the cyclic hardening (Ohno and Kachi, 1986). The size of this surface changes only when the amount of the plastic strain produced exceeds the size (i.e., radius) of the surface, so that the plastic strain is on the surface and the direction of flow is external to the surface (LeMaitre and Chaboche, 1990). This idea is completely parallel

to the hardening of a yield surface in the stress space. The nonhardening plastic strain region may be explained from the standpoint of a dislocation theory as "dislocations piled up to obstacles may be remobilized under reverse straining, and thus a certain amount of plastic strain may proceed without marked increase of the dislocation density after a reversal of the straining direction" (Ohno and Kachi, 1986).

The concept of a nonhardening region may be incorporated into almost any previously discussed plasticity model, so that a model combining both stress space and plastic strain space surfaces, each having their own isotropic and kinematic hardening rules, may be viewed as a generalization of a typical stress space plasticity model. There are many ways to specify evolution rules for the nonhardening strain range. It can be assumed to be always centered at the origin of the plastic strain space, and to exhibit only isotropic hardening. In a more general case, both kinematic and isotropic hardening rules may be used. Assuming isotropic behavior, the von Mises type surface is one of the simplest to use. The equation of the limiting surface may then be written as (Ohno and Kachi, 1986):

$$\phi = \frac{2}{3}(\varepsilon_{ij}^{p} - \eta_{ij}) \cdot (\varepsilon_{ij}^{p} - \eta_{ij}) - \rho^{2} = 0 \tag{3.2}$$

where: ε_{ij}^{p} is a plastic strain tensor

η_{ij} is the center of the limiting surface in plastic strain space

ρ is a size parameter (often called the radius of the surface)

The consistency condition written for this limiting surface gives:

$$\frac{2}{3}(\varepsilon_{ij}^{p} - \eta_{ij}) \cdot (d\varepsilon_{ij}^{p} - d\eta_{ij}) - \rho d\rho = 0 \tag{3.3}$$

The kinematic hardening rule for this surface may be defined as (Ohno and Kachi, 1986):

$$d\eta_{ij} = \gamma \cdot d\varepsilon_{ij}^{p} \text{ if } \phi(\varepsilon_{ij}^{p} + d\varepsilon_{ij}^{p}) > 0 \tag{3.4}$$

where: γ is a kinematic hardening parameter assuming values between zero and one

The kinematic hardening rule and the consistency condition completely define the isotropic hardening rule, which takes the form:

$$d\rho = \frac{2}{3}(1-\gamma) \cdot (\varepsilon_{ij}^{p} - \eta_{ij}) \cdot \frac{d\varepsilon_{ij}^{p}}{\rho} \text{ if } \phi(\varepsilon_{ij}^{p} + d\varepsilon_{ij}^{p}) > 0 \tag{3.5}$$

Thus, the evolution rules for the limiting plastic strain surface are completely defined once the specific value of γ is chosen.

The choice of the value of the hardening parameter γ corresponds to incorporating different degrees of memory fading into the model. In particular, the constant value of 0.5 corresponds to the assumption of nonfading memory of past straining; it was used for the early formulations and is also used in this work (Ohno and Kachi, 1986). For this choice of the hardening parameter, the limit plastic strain surface is an envelope of all plastic deformation experienced by the material specimen. The material memory predicted by such a model is permanent--it never fades (LeMaitre and Chaboche, 1990). A repetitive excursion with some plastic range produces the same effect as a single excursion of the same range, if this formulation is used. In particular, if a specimen is cycled with a constant strain range which is symmetric about the origin, the nonhardening region expands during the first cycle, and does not change thereafter (White, 1987).

3.7 Shen's Cyclic Plasticity Model

The multiaxial cyclic bounding surface plasticity model developed by Shen (Shen et al., 1995) forms the basis for the constitutive description of the steel tubes in this research. This model was first developed for cyclic uniaxial loading of structural steel (Mizuno et al., 1992), and subsequently generalized to a multiaxial bounding surface model (Shen, 1993; Shen et al., 1995; Mamaghani et al., 1995).

This model utilizes the concept of a nonhardening plastic strain space surface in addition to the loading and bounding surfaces that are defined in stress space. The value of the hardening parameter γ is equal to 0.5, so that a nonfading material memory is modeled. There are also additional deviatoric stress space surfaces employed by the model which will be described below. All surfaces used by this model are of the von Mises type (Khan and Huang, 1995), with their shape not changing during the analysis. The point conjugate to the current stress point is always defined by Mroz rule (Shen 1993).

In addition to the features of bounding and nonhardening surface models described above, the Shen model provides several features which are unique to this model. Their main purpose is to provide a more accurate prediction of a stress-strain response to a random cyclic loading. These features include introduction of a virtual bounding surface and a memory surface in stress space, modification of the shape parameter h of Eq. 3.1, variation of the bounding slope, and decrease of the loading surface size with an increase in plastic straining.

The shape parameter h is usually taken to be a constant or a function of an initial plastic distance δ_{in}, in which case it is constant during a particular loading path from the initiation of plastic loading to the stress reversal (Dafalias, 1975). However, Shen (1993) concluded that a better correlation with the experimental results is obtained if the shape parameter changes continuously within each loading path with the change of the plastic distance δ. A linear relation of the form $h = e \cdot \delta + f$, where e and f are constant model

parameters, is used in the model. These parameters were obtained by the least squares method using the results of uniaxial cyclic experiments (Shen, 1993).

A common deficiency of the bounding surface models is the overshooting phenomenon discussed above. In addition to this, Shen (1993) found that the model predicts earlier reduction in modulus compared to the experimental results for the cases when unloading from the bounding surface is followed by reloading prior to the reverse stress point reaching the bounding surface. This earlier modulus reduction arises from the underestimation of the plastic distance values in the calculation of plastic modulus (Shen, 1993).

To correct both of these phenomena, Shen et al. (1995) proposed an addition of using a memory surface and a virtual bounding surface in deviatoric stress-space. The centroids of the memory and virtual bounding surfaces coincide with that of the bounding surface. The initial memory surface size is equal to the initial loading surface size, and all these surfaces are centered at the origin. As the loading surface hardens during plastic loading, the memory surface hardens isotropically and kinematically, so as to always enclose the loading surface and yet still share its centroid with the bounding surface. Thus, the radius of the memory surface is proportional to the maximum distance from the stress point to the center of then current bounding surface, where the maximum is taken over the entire loading history of the fiber. The size of the memory surface is always less than or equal to that of the bounding surface, but greater than or equal to that of the loading surface. Mathematically the radius of the memory surface is expressed as (Shen et al., 1995):

$$\bar{\kappa}_m = \left\{ \sqrt{\frac{3}{2}} \left\| S_{ij} - \beta_{ij} \right\| \right\}_{\max} \tag{3.6}$$

where: $\bar{\kappa}_m$ is the radius of the memory surface

β_{ij} is the centroid of the bounding surface

S_{ij} is the current stress point in deviatoric stress space

If the stress point unloads from the memory surface and then the loading is reversed before the memory surface is reached in the reverse direction, the distance δ_m between the point of reversal and its conjugate point on the memory surface is calculated in the manner analogous to the plastic distance calculation. The virtual bounding surface is then defined as the surface centered at the bounding surface center. The radius of the virtual bounding surface is greater than the radius of the bounding surface by $\delta_v=\delta_m$. This can be expressed as (Shen et al., 1995):

$$\bar{\kappa}_v = \bar{\kappa} + \delta_v \tag{3.7}$$

where: $\bar{\kappa}_v$ is the radius of the virtual bounding surface

$\bar{\kappa}$ is the radius of the current bounding surface

δ_v is the metric distance between the point of reversal and its conjugate point on the memory surface

The plastic distance δ is measured to the virtual bounding surface instead of the bounding surface as long as the stress point is inside the memory surface. As soon as the stress point reaches the memory surface, the plastic distance is measured to the bounding surface. This may create a discontinuity in the value of the plastic distance and, subsequently, the plastic modulus, but the stress-strain curve remains continuous. Through the use of the memory surface, it is possible to identify smaller plastic excursions relative to previous larger plastic excursions, where smaller excursions are the ones with the reverse stress point not reaching the memory surface prior to reversal. This arrangement leads to good accuracy in prediction the small unloading-reloading loops and minimizes the overshooting effect. Thus, use of the memory and virtual bounding surfaces improves the plastic modulus prediction, decreases the amount of ratchetting, and affects the magnitude of the Bauschinger effect. Shen et al. (1995) show excellent comparisons to cyclic experiments of structural steel using this feature of the model.

The model utilizes the plastic strain space nonhardening surface to calculate the yield and bounding surface radii. The bounding surface is assumed to expand with an increase in the plastic strain range. Thus, the bounding surface radius is an increasing function of the nonhardening surface radius, changing from the initial value to the ultimate tensile strength of the material. The loading surface, on the other hand, decreases with the increase in the plastic strain range. This feature is unique to the Shen model, and it is introduced to model the pronounced decrease of the elastic zone under increasing plastic strain range observed experimentally. Thus, the loading surface radius is also a function of the nonhardening surface radius, and it changes from the initial yield stress of the material to a value of approximately 20% of the initial size. The change in size is rapid at low levels of plastic strain, but it stabilizes after achieving a plastic strain of approximately 1%. The radius of the loading surface is calculated as (Shen et al., 1995):

$$\kappa = \kappa_o \cdot [\alpha - a \cdot \exp(-200b \cdot \rho) - (\alpha - a - 1) \cdot \exp(-200c \cdot \rho)] \tag{3.8}$$

where: κ is the radius of the loading surface

κ_0 is the initial radius of the loading surface

ρ is the radius of the nonhardening surface

α, a, b, and c are calibrated parameters of the model

Calibrated parameters were calculated by fitting the experimental data, and their values are given in (Shen et al., 1995) for several types of structural steel.

The bounding value of the plastic modulus is commonly assumed to be constant in the bounding surface formulations, but the experimental evidence suggests that it gradually decreases with increased cyclic excitation. Thus, the bounding modulus is a decreasing function of plastic work, asymptotically approaching zero. It is calculated as (Shen et al., 1995):

$$E_0^P = \frac{E_{0i}^P}{1 + \omega \cdot W^P} \tag{3.9}$$

where: E_{0i}^P is the initial value of the bounding modulus

W^P is the plastic work

ω is a calibrated model parameter

It should be noted that the model may predict unrealistically high stresses at large levels of strain (say greater than 5%) because the bounding slope does not decrease sufficiently fast. This discrepancy is particularly noticeable for the cases of monotonic loading, since the amount of plastic work is significantly less that that produced during the repeated cyclic loading with the same strain amplitude. For lower levels of straining and typical cyclic loading, the prediction of bounding modulus is satisfactory.

3.8 Calibration of the Cyclic Steel Plasticity Model

Shen et al. (1995) calibrated their cyclic steel model to tests of structural steel box columns. This steel showed a definitive yield plateau when stressing a virgin specimen. As discussed in Section 3.2, material taken from either the corners or flanges of a cold-formed tube steel often exhibit a distinctive rounded shape with a proportional limit that is substantially below the 0.2% offset stress of the coupons. Stress-strain curves obtained from coupon tests are shown in Fig. 3.2a for a coupon cut from a flat flange region of a cold-formed steel tube, and in Fig. 3.2b for a coupon cut from a corner region [experimental data from (Sully and Hancock, 1994) are represented by the solid line].

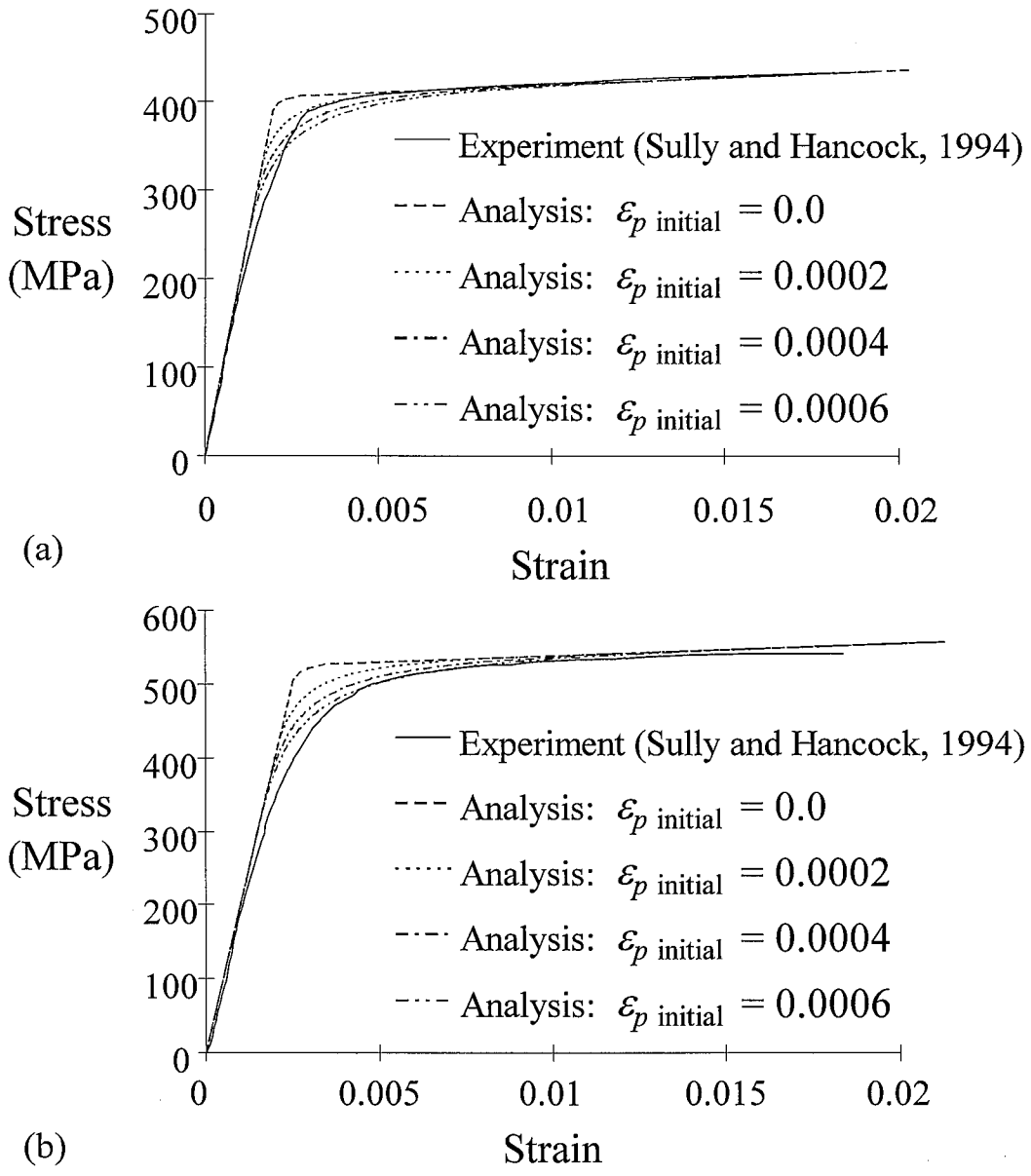

Figure 3.2: Comparison of Analysis to Strain-Stress Curves from Coupon Tests: a) Tube Flanges; b)Tube Corners

In this research, the size of the strain-space nonhardening surface is initialized to a non-zero value (rather than having a typical initial size of zero) to account for this straining. This is consistent with accounting for residual strain, rather than residual stress, as noted in Section 3.2. The loading surface size, which is a function of the size of the

nonhardening surface, is then modified according to the hardening rules of the model to properly reflect the initial plastic strain value. This modification produces a value of the initial proportional limit, and thus of the initial loading surface size, that is approximately 60% of the 0.2% offset yield stress of the steel tube. The initial plastic strain, $\varepsilon_{p\ initial}$, differs for the fibers in the corners and the flanges of the steel tube, with a value of initial strain of 0.0006 taken in the corners, and 0.0004 taken in the flanges (for the modeling of annealed tubes, these values are taken as zero). The value adopted for the corners is greater to account for the higher degree of cold-working experienced by the corners, relative to the flat portions of the tube. This causes the ratio of the initial elastic zone to the yield stress to be smaller for the corners, producing a more rounded stress-strain curve, which corresponds to the experimental observations (Lu and Kennedy, 1994; Sully and Hancock, 1994). Figure 3.2 indicates the strong correlation achieved between the experimental data and the constitutive model using these values of initial plastic strain. If these initial strains are not accounted for, the decrease in the elastic zone, as per Shen's calibration parameters, is significant in the early cycles of straining. Such a decrease is appropriate for structural steel which has an initial yield plateau, but is excessive for the behavior found in cold-formed tube steel. It should be noted that since the multiple coupon tests of Sully and Hancock (1994) showed some scatter, two coupon tests in the mid-range of their results were used for these calibrations.

In addition to the ratio of the proportional limit to the yield stress being different in the corners and flanges, the initial yield stress of the steel tube material differs in the corners and flanges, with the yield stress in the corners as much as 25% higher, as discussed in Section 3.2. In practice often only the yield and ultimate stress obtained from a stub-column test are available. In such a case, the variations of the material properties are not known, and the model must assign them using an assumed variation pattern and known average parameters. Thus, at the next stage of the calibration process, an average stress-average strain curve was obtained from the results of a stub-column test for which the actual yield stresses of the flange and corner portions of the tube were reported in (Sully and Hancock, 1996). From this curve, a nominal yield stress of the

steel tube was calculated, where the nominal yield stress was assumed to be measured as a 0.2% offset on the average stress-average stress curve obtained from the stub-column experiment. Ratios of the measured yield stresses at the flats and corners (attained from coupon tests) to this nominal average yield stress were then calculated. These ratios were assumed to be representative of cold-formed tubes. As a result, in this work, the yield stress of the material is varied from a minimum value in the flanges (0.96 times the reported nominal yield stress) to a peak in the corners (1.2 times the reported nominal yield stress), with an eighth order polynomial used to vary the yield stress continuously along the depth of each flange of the tube. The eighth order polynomial was chosen to approximate the variation of the yield stresses along the tube side reported by Bridge (1976). A constant yield stress is used for all fibers if the steel tube is annealed. The ratio of the measured yield stress in the flange portion of the tube to the nominal yield stress obtained from a stub column curve was also recorded by Shakir-Khalil and Mouli (1990). This ratio was reported to vary between 0.95 and 0.99, with an average value of 0.96.

3.9 Typical Cyclic Behavior Patterns Predicted by the Model

In order to illustrate the capabilities of the adapted steel model, it is instructive to consider its ability to predict several typical loading cases, such as constant stress and constant strain range loading.

If the fiber is subjected to cyclic loading with a constant strain range, the model predicts stabilization of the stress-strain curve after the first cycle, as shown in Fig. 3.3. This stabilization is caused by the fact that the nonhardening surface does not expand after the completion of the first cycle since the plastic strain range remains constant.

If the strain range is increased with each subsequent cycle, the model predicts an increase in the peak stress values, i.e., it exhibits cyclic hardening (Shen, 1993). The rate

of this increase diminishes with increasing cyclic excitation due to the gradual decrease of the bounding plastic modulus, as can be seen in Fig. 3.4.

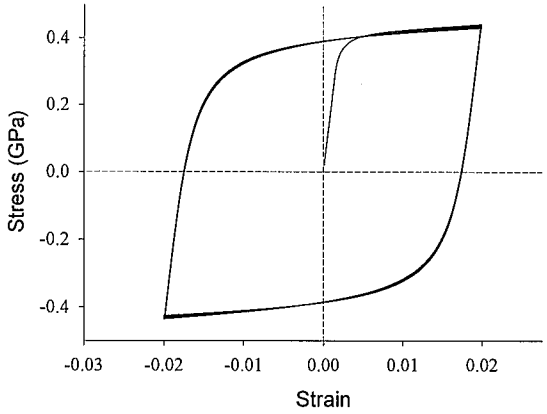

Figure 3.3: Symmetric Constant Strain Range Cycles

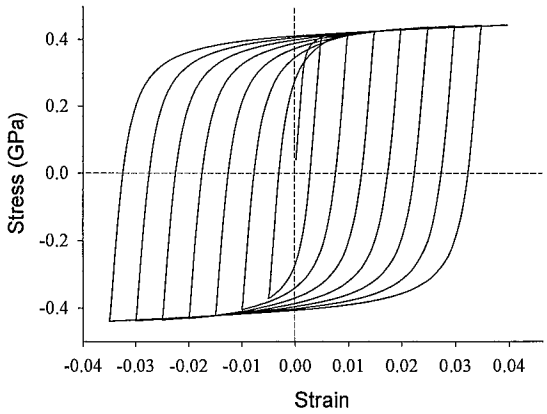

Figure 3.4: Symmetric Increasing Strain Range Cycles

An increase in the peak stress values is also predicted if the fiber is subjected to cyclic loading with an unsymmetric strain range. The maximum stress achieved in compression increases with an increase of the tensile plastic strain range, as can be seen in Fig. 3.5. This type of cyclic hardening under unsymmetric strain range has been observed in uniaxial structural steel experiments (Cofie and Krawinkler, 1985).

If the fiber is subjected to cyclic loading with a constant stress range and a nonzero mean stress, the model predicts a limited amount of ratchetting, as shown in Fig. 3.5. No ratchetting is predicted for cyclic loading with a constant stress range and a mean stress equal to zero.

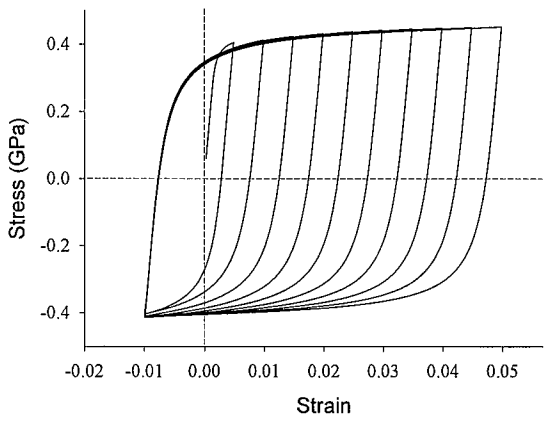

Figure 3.5: Unsymmetric Increasing Strain Range Cycles

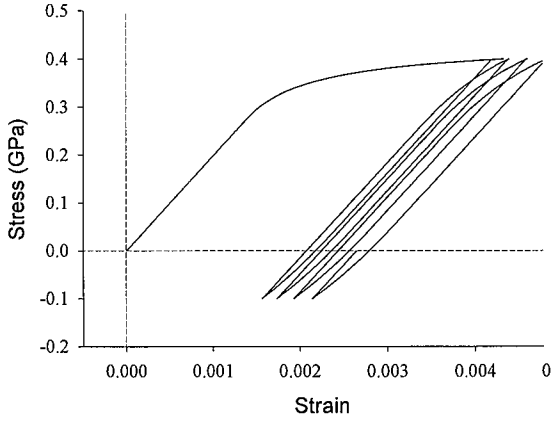

Figure 3.6: Unsymmetric Constant Stress Range Cycles

3.10 Suitability of Selected Steel Model for CFT Analysis

As can be seen from the discussion in this chapter the adapted cyclic plasticity steel model, as extended for the current research, is capable of modeling all important behavioral phenomena exhibited by tube steel. The ability of the model to predict the following features are particularly important for the CFT analysis:

- Rounded shape of the stress-strain curve
- Lack of yield plateau
- Decreasing elastic zone
- Elastic unloading
- Bauschinger effect
- Cyclic hardening
- Bounding stiffness
- Limited amount of ratchetting

All of these features propagate from the stress-strain level to the stress resultant level of the CFT, thus affecting the global element behavior.

Chapter 4

Cyclic Concrete Plasticity Model

4.1 Requirements for the Model

This chapter describes the cyclic plasticity concrete model used in this work. A set of desirable features of the model is outlined, followed by a review of several types of cyclic concrete plasticity models which have been reported in the literature. A detailed description of the model adopted for the current research is provided, and several extensions to the model implemented in this research are described.

In order to select a concrete model, the structural response of a CFT beam-column subjected to cyclic loading must be considered, as was done in Chapter 3 for the steel model selection. The important features of the structural response that are most directly related to the concrete behavior are:

1. A decrease of the elastic zone (i.e., the zone of linear load-deformation response) is caused by the concrete crushing, as well as by local buckling and decrease of the elastic zone of the steel. The nonlinear stress-strain behavior of concrete at moderate to high stress levels also contributes to the elastic zone decrease on the structural level.
2. Strength degradation with progressive cyclic loading is caused by damage induced in the concrete, manifested in microcrack formation, as well as by local buckling of the steel tube.
3. Gradual stiffness reduction of a CFT beam-column is partially due to stiffness reduction of the concrete fibers at the stress-strain level.

Additionally, it has been observed in CFT experiments that the confining pressure exerted on the concrete by the steel tube does not significantly affect the strength of rectangular CFTs, although it noticeably increases the member ductility (Bridge, 1976). The selected concrete model must be capable of accurately representing strength and stiffness degradation during cyclic loading, and it must be able to account for the ductility enhancement due to confinement in an approximate fashion.

4.2 Selection of the Model

Several classes of material models have been used in the fiber analysis of concrete or composite structures. Traditionally, one of the most popular types has been the use of a set of algebraic curves specifying the uniaxial stress-strain relation. Originally developed for monotonic concrete response, these curves provided polynomial expressions of the stress in terms of the strain. Most of these curves were defined separately for several regions, such as an elastic zone at low stress level, an inelastic region up to the peak stress, and a post-failure branch. These formulations were simple, yet accurate in modeling monotonic response of concrete fibers.

The popularity of uniaxial algebraic stress-strain curves for monotonic analysis promoted their use for cyclic analysis. Since the inelastic behavior of concrete is inherently dependent upon loading history, a simple function relating the stress to the strain became insufficient for cyclic analysis. Several sets of comprehensive rules have been proposed in the literature to account for this history dependence, so that different values of stress may correspond to the same strain level (Mander et al., 1988). These rules may include several expressions for envelope curves, supplemented by rules for transition curves, partial unloading and reloading branches, etc. (Chang and Mander, 1994). In addition to this, a uniaxial model could be modified to account approximately for the confinement of the concrete by the steel tube, so that both the peak stress and the ductility of the fiber are affected. An extensive calibration to experimental results is required for such models, and the need to explicitly account for a wide range of complex loading histories complicates the implementation. Cyclic uniaxial stress-strain curves

have been used in the fiber analysis of concrete structures (Taucer et al., 1991; Chang and Mander, 1994; El-Tawil and Deierlein, 1996) and CFTs (Kawaguchi, 1991; Inai and Sakino, 1996).

An alternative approach is to use a multiaxial stress- and/or strain-space incremental plasticity formulation for the cyclic concrete model. Such formulations usually postulate a plastic potential surface and formulate a rule for plastic flow, thus eliminating the need to specify numerous branches of the stress-strain curve explicitly. While the potential surface expression and the flow rule must still be calibrated to experimental results, use of a multiaxial incremental plasticity model leads to a more uniform and consistent formulation, thus simplifying the implementation. Moreover, use of a multiaxial plasticity model permits future extension of the fiber element formulation in which the circumferential stresses and strains in the concrete caused by confinement are accounted for explicitly, so that the influence of the concrete core confinement by the steel tube on the member behavior may be studied.

For practical implementation, suitable for frame analysis, a model providing a sufficiently accurate description of concrete behavior at both prefailure and postfailure stages within the incremental plasticity formulation is needed. As described at the beginning of this chapter, the most critical features of the concrete behavior for the modeling of CFTs are having accurate representation of the nonlinear stress-strain relation, and gradual stiffness and strength degradation under cyclic loading. A bounding surface plasticity formulation including softening based on accumulation of damage is selected for this research, as it is one of the more versatile, yet relatively simple classes of the incremental plasticity models that has found widespread application in the analysis of structures.

4.3 Bounding Surface Cyclic Plasticity Formulation

4.3.1 General Description of the Model

The concrete model used in this research is adapted from a model first proposed by Chen and Buyukozturk (Chen and Buyukozturk, 1985) and later expanded and refined by Buyukozturk and others (Buyukozturk and Ameur-Moussa, 1988; Ameur-Moussa and Buyukozturk 1990; Pagnoni et al., 1992). This is a multiaxial bounding surface model capable of predicting the behavior of concrete in cyclic compression. The model postulates the existence of a bounding surface in normalized stress space, so that the current stress point is always either inside or on the bounding surface. The peak concrete strength is attained when the stress point contacts the bounding surface. This model is applicable only to stress states where all principle stresses are compressive. A scalar damage parameter is used to model gradual strength and stiffness degradation. The model can satisfactorily predict a nonlinear stress-strain relationship, monotonic softening in the post-failure region, the shear compaction-dilatancy phenomenon, and stiffness degradation caused by cyclic loading. The model is extended in the current research to provide additional capabilities important for CFT modeling. The primary extensions are:

1. *Modeling of cyclic tension.* The bounding surface model as formulated by (Ameur-Moussa and Buyukozturk, 1990) does not include modeling of concrete in tension. However, tensile longitudinal stresses are expected to develop in many CFT concrete fibers during the cyclic seismic loading. Moreover, transitions from compression to tension on the fiber level are expected during cyclic loading, so that a numerical procedure that accounts for such transitions is needed. Since it has been shown that neglecting the tensile capacity of the concrete can cause the results of the analysis of concrete-filled steel tubes to be significantly inaccurate (Hajjar and Gourley, 1996), modeling of tensile behavior and tension-compression transitions is an important part

of the cyclic model. Consequently, cyclic tension and tension-compression transition capabilities were added to the model.

2. *Account for confinement.* Since, in the current implementation, circumferential and radial stresses and strains are not calculated explicitly, a modification of the uniaxial stress-strain response is needed to account implicitly for the confinement of the concrete core by the steel tube. While the effect of confinement on the uniaxial concrete peak strength may be considered small for rectangular CFTs of practical dimensions, its effect on the ductility, manifested by a change of the postfailure slope of the longitudinal uniaxial stress-strain curve, is more pronounced (Bridge, 1976). The postfailure branch of the stress-strain curve was thus modified to account approximately for the effect of confinement.
3. *High compressive strain level.* Modeling of CFTs subjected to cyclic seismic loading requires the formulation to predict the material behavior at a relatively high strain level in the postfailure region, placing a high demand on the robustness of the formulation in this region. Therefore, the model was extended to the high strain postfailure region, and the damage parameter calculations were supplemented by a consistency condition.

The model is formulated in terms of normalized stresses and strains, so that all model parameters are unitless. This is achieved by dividing all quantities having units of stress by the uniaxial peak concrete compressive strength, f'_c, and all strain and related quantities by the corresponding strain at the peak stress, ε_c. In addition, compressive stresses and strains are assumed to be positive in this concrete plasticity formulation (Ameur-Moussa and Buyukozturk, 1990).

The rest of this section describes the main features of the adapted concrete cyclic plasticity model, together with the extensions of the model provided in the current research.

4.3.2 Lack of Elastic Zone

In accordance with experimental observations showing the concrete stress-strain curve to become nonlinear even at relatively low levels of stress (Chen and Han, 1986), the model assumes no elastic zone region. This means that both loading and unloading are governed by incremental plasticity rules, and that the behavior predicted by this model is always nonlinear. Since the model uses a bounding (failure) surface, but no loading surface, it can be classified as a one surface model. In terms of more common bounding surface formulations employing two surfaces, it also can be thought of as a model with a point loading surface, since the elastic range is zero and the loading surface is reduced to the current stress point.

Lack of an elastic zone also causes the reloading branch of the stress-strain curve to be different from the unloading branch, thus modeling the hysteresis loops observed experimentally during cyclic loading of concrete. On the other hand, the model parameters are calibrated so that both loading and unloading branches of the stress-strain curve are initially very close to linear response, with the stiffness close to the initial loading stiffness of concrete. This also causes the hysteresis loops to be relatively narrow prior to obtaining the concrete peak strength. Thus, even though the model does not postulate an elastic region, it predicts the response close to that obtained by models having a small elastic zone. Therefore, the formulation models the behavior of concrete at low values of stress where the deviation from linearity is small, and it models progressively higher nonlinearity with an increase of the stress level.

This model utilizes a scalar damage parameter, K, as a measure of the damage sustained by a material point. While the distribution of the microcracks in the concrete may create anisotropy even if the initial state is assumed to be isotropic, it would require a substantially more complex formulation utilizing a tensorial damage variable to account for the induced anisotropy. Use of a scalar damage parameter is preferred in this research since it simplifies the model while still accounting for the material damage in the average sense. Although the idea of damage measure has a sound physical justification, in a

continuum mechanics-based model such as the current formulation, the damage parameter must be expressed as a function of either stress or strain quantities, rather than be based explicitly on the microcrack distribution.

4.3.3 Damage Parameter Calculation

In the current model, a scalar damage parameter increment, dK, is defined differently for the loading, unloading, and postfailure regions. In addition, loading and unloading are defined separately for the deviatoric plane and along the hydroaxis. Deviatoric loading is defined as a stress change causing the increment of the normalized distance from the current stress point to the bounding surface to be positive (calculation of the normalized distance is described in Section 4.3.4):

$$dD = D - D_{old} \geq 0 \tag{4.1}$$

where: D is the current value of the normalized distance

D_{old} is the previous value of the normalized distance

Thus, the deviatoric loading state corresponds to the stress point approaching the bounding surface. Hydrostatic loading is defined as a stress change corresponding to an increase of the first stress invariant:

$$dI_1 = I_1 - I_{1,old} \geq 0 \tag{4.2}$$

where: I_1 is the current value of the first stress invariant

$I_{1,old}$ is the previous value of the first stress invariant

In principal stress space, deviatoric loading or unloading can be visualized as the movement of the current stress point in the deviatoric stress plane (or in a plane parallel to it), while hydrostatic loading or unloading correspond to a movement parallel to the hydrostatic axis. During a single stress increment, both hydrostatic and deviatoric

loading or unloading may occur. The separation of deviatoric and hydrostatic loading is needed to represent experimental observations that some components of the concrete response are affected by either deviatoric or hydrostatic components of the stress increment, but not always by both. In particular, this separation permits modeling of important phenomena observed experimentally: 1) An increase in volumetric stress alone does not affect octahedral shear strain, and 2) Volumetric strain is affected by both volumetric and octahedral shear stress changes. These phenomena together produce the shear compaction-dilatancy phenomenon characteristic of the concrete (Chen and Buyukozturk, 1985). Modeling them as accurately as possible is an important requirement for any realistic concrete model. The current model provides nonlinear expressions that are functions of the maximum damage parameter value for both shear compaction and dilatancy factors, which are calculated separately. A single shear compaction-dilatancy factor, β, calculated as a sum of the compaction factor and the dilatancy factor, is a proportionality coefficient in the linear expression connecting the plastic volumetric strain and the plastic octahedral shear strain. This compaction-dilatancy factor is utilized in the fiber tangent stiffness calculations (Ameur-Moussa and Buyukozturk, 1990).

For the cases of deviatoric loading and unloading, the damage parameter increment is proportional to the normalized distance increment. It is calculated as:

$$dK = \frac{R \cdot dD}{H^P \cdot F_1} \tag{4.3}$$

where: H^P is a plastic shear modulus

F_1 is a function that accounts for the hydrostatic pressure and stress path dependency

The function F_1 is calibrated to normalize the value of the damage parameter, such that the damage parameter is equal to 1.0 at the peak stress of a monotonic uniaxial

compressive loading excursion (Ameur-Moussa and Buyukozturk, 1990). The function F_1 is defined separately for deviatoric loading and unloading, and contains empirical expressions involving the current values of the stress invariants, and the maximum values of the first stress invariant and the function F_1 itself. The use of these maximum values accounts for the stress path dependency of the function F_1.

For the case of postfailure, the current stress point remains on the bounding surface so that the normalized distance is equal to zero. Thus an alternative definition of the damage parameter increment is needed for the postfailure region. Ameur-Moussa and Buyukozturk (1990) defined the damage parameter increment to be proportional to the octahedral plastic shear strain increment $d\gamma_o^p$, since the octahedral plastic shear strain was thought to be a good measure of the overall material plastic straining in the deviatoric plane. The damage parameter increment is calculated in the postfailure range as:

$$dK = \frac{d\gamma_0^p}{F_1} \tag{4.4}$$

where: $d\gamma_o^p$ is the octahedral plastic shear strain increment

The plastic octahedral shear strain increment is related to the incremental octahedral shear stress, $d\tau_o$, by the plastic shear modulus, H^p:

$$d\gamma_0^p = \frac{d\tau_0}{H^p} \tag{4.5}$$

where: $d\tau_o$ is the incremental octahedral shear stress

The octahedral shear stress is calculated as:

$$\tau_o = \sqrt{\frac{2 \cdot J_2}{3}} \tag{4.6}$$

where: J_2 is the second deviatoric stress invariant:

$$J_2 = \frac{1}{2}(s_1^2 + s_2^2 + s_3^2) \tag{4.7}$$

where: s_i are principal deviatoric stresses

The damage parameter is assumed to increase during deviatoric loading and postfailure regimes, and decrease during deviatoric unloading. The damage parameter is assumed to remain constant during the tensile loading or unloading, since it models only the material damage in compression.

4.3.4 Strength Degradation

This model postulates the existence of a bounding surface which is selected to coincide with the stress-space failure surface of the concrete. Its shape has been determined from multiaxial monotonic experiments (Ameur-Moussa and Buyukozturk, 1990). Failure surfaces for monotonic and cyclic loading are assumed to coincide for a given level of damage, in accordance with the experimental observation that a monotonic loading curve in compression approximately provides an envelope of the cyclic compression curves. The equation of the bounding surface is (Ameur-Moussa and Buyukozturk, 1990):

$$F = \frac{0.25 \cdot \sqrt{J_2} + 3.10 \cdot J_2}{4 \cdot I_1 + 3.48} \cdot (\cos 3 \cdot \theta + 5) - \frac{40}{39 + K_{max}^2} = 0 \tag{4.8}$$

where: K_{max} is the maximum value of the damage parameter experienced during the entire loading history

θ is a Lode angle defined as the angle between the projections of the current stress vector and the tensile semiaxis on the deviatoric stress plane, calculated from:

$$\cos 3 \cdot \theta = \frac{-3 \cdot \sqrt{3 \cdot J_3}}{2 \cdot (J_2)^{3/2}} \tag{4.9}$$

where: J_3 is the third deviatoric stress invariant:

$$J_3 = s_1 \cdot s_2 \cdot s_3 \tag{4.10}$$

The term $H = \frac{40}{39 + K_{max}^2}$ is intended to give values close to 1.0 for the prefailure region during monotonic uniaxial compression. For the peak stress value of monotonic uniaxial compression, the maximum damage parameter, K_{max}, is equal to 1.0, and thus H is also equal to 1.0, and the bounding surface expression reduces to that for monotonic loading.

The bounding surface is mean pressure and Lode angle dependent, and it forms a non-circular cone in the Haigh-Westergaard space that is open in the compression direction of the hydrostatic axis. The cone is centered on the hydrostatic axis. The bounding surface size depends on the maximum value of the damage parameter, K_{max}, ever experienced during the entire loading history of a fiber, so that the surface shrinks isotropically with damage accumulation. It is important to note that the bounding surface is not allowed to expand during the load history, even when the value of the damage parameter is decreased during unloading. This is achieved by making the bounding surface size a function of the maximum value of the damage parameter ever experienced by material. Since the maximum damage value is a nondecreasing function of loading history, the bounding surface size either decreases or remains constant in the process of loading. No kinematic hardening of the bounding surface is used.

For a given stress point, an image point is defined by a radial mapping on the bounding surface, i.e., as the intersection of a line, going through the current stress point in the deviatoric stress direction, with the bounding surface. This line lies in the plane parallel to the deviatoric plane and containing the current stress point. The intersection of that plane with the hydrostatic axes is referred to as the center point. The normalized distance, D, from the stress point to the bounding surface is used to calculate the value of the damage parameter and plastic modulus (see Section 4.3.3). The normalized distance, D, is defined as the ratio of the stress point radius, r, to the image point radius, R:

$$D = \frac{r}{R} \tag{4.11}$$

where: r is the stress point radius

R is the image point radius

Both radii are measured from the center point in the deviatoric plane. The current stress point radius is calculated as:

$$r = \sqrt{2 \cdot J_2} \tag{4.12}$$

No explicit formula for the image point radius is given by (Ameur-Moussa and Buyukozturk, 1990). However, since both the image point and the current stress point have the same values of the first stress invariant, I_1, the Lode angle, θ, and the maximum damage parameter value, K_{max}, these parameters can be substituted into the bounding surface equation, along with the components of the image point. This substitution yields a quadratic equation with one unknown, the value of the second deviatoric stress

invariant, J_2^*, corresponding to the image point. This equation can then be solved explicitly for J_2^*, from which the image stress point radius is calculated as:

$$R = \sqrt{2 \cdot J_2^*} \tag{4.13}$$

The final formula for the image point radius is:

$$R = -8.825 + \sqrt{77.88 + \frac{1280 \cdot I_1 + 1114}{\left(39 + K_{max}^2\right) \cdot \left(\cos 3 \cdot \theta + 5\right)}} \tag{4.14}$$

Normalization of the distance from the current stress point to the bounding surface by the value of the image point radius is needed to account for the mean pressure and Lode angle dependence of the bounding surface. The normalized distance, *D*, and is a measure of the proximity of the stress point and the bounding surface, and it changes from zero, when the stress state is in hydrostatic compression, to one, when the stress point lies on the bounding surface.

4.3.5 Modeling of Tension

The tensile behavior of the concrete is based on a formulation presented in (ASCE, 1982) and is modeled as being linear elastic (with a stiffness equal to the tangent stiffness at the point at which the stress changes from compressive to tensile) up to the rupture stress. After rupture, the fiber loses all capacity to retain stress in tension, thus modeling the opening of the crack. Upon reversed loading, compressive behavior is reinitiated at the point at which tensile behavior first initiated, thus simulating crack closure (ASCE, 1982).

4.4 Postfailure Region Modeling

4.4.1 Calculation of Damage from the Consistency Condition

The postfailure region is characterized by softening of the material. The current stress point is assumed to remain on the bounding surface during this phase, and the damage parameter increases, with its increments being proportional to the octahedral plastic shear strain increments (see Eq. 4.4). The requirement for the stress point to remain on the failure surface during postfailure loading can be mathematically expressed by setting the total differential of the bounding surface function to zero. This leads to an equation, commonly referred to as the consistency equation, which expresses the differential of the bounding surface in terms of stresses, the maximum value of the scalar damage parameter, K_{max}, and the increments of these quantities. From the consistency equation, the increment of the maximum value of the damage parameter, dK_{max}, can be obtained as a function of stresses, stress increments, and the maximum value of the damage parameter, as described below. The maximum value of the damage parameter is defined as the largest value of the damage parameter, K, during the entire load history, and it is dependent upon the loading history. In the general case, the consistency condition for the bounding surface cannot be utilized, since the maximum damage parameter value cannot be calculated incrementally. Rather, the maximum value of the damage parameter must be calculated as the maximum of its current value and the current level of damage:

$$K_{max} = \max(K_{max,old}, K) \tag{4.15}$$

On the other hand, when at the beginning of step the current value of the damage parameter is equal to its maximum value, and the loading condition is postfailure, it is guaranteed that this equality will also hold at the end of the step, since the damage parameter increases in the postfailure region. For this case, the value of the damage

parameter is equal to its maximum value during the entire step, and it is appropriate to calculate the damage parameter increment directly from the consistency equation, using the damage parameter increment, dK, in place of the maximum damage parameter increment, dK_{max}. For all other cases, such a substitution of dK in place of dK_{max} will not be appropriate and may lead to erroneous values of the maximum damage parameter. Therefore, the consistency equation may not be used, unless the current and the maximum values of the damage parameter are equal at the beginning of the postfailure loading step.

The first order consistency condition for the bounding surface where dK is substituted for dK_{max} has a general form:

$$dF = \frac{\partial F}{\partial \sigma_i} \cdot d\sigma_i + \frac{\partial F}{\partial K} \cdot dK = 0 \tag{4.16}$$

where: σ_i are principal stresses

F is the bounding surface defined by Eq. 4.8

from which an expression for the damage increment can be obtained as:

$$dK = -\frac{\frac{\partial F}{\partial \sigma_i} \cdot d\sigma_i}{\frac{\partial F}{\partial K}} \tag{4.17}$$

For the uniaxial case, only the longitudinal stress, σ, is considered, and the consistency equation can be simplified to yield:

$$dK = \frac{40 - \left(39 + K^2\right)\left(0.1667 \cdot \sigma + 1.790\right)}{\left(0.1667 \cdot \sigma^2 + 3.580 \cdot \sigma\right)K} \cdot d\sigma \tag{4.18}$$

Thus the increment of the damage parameter is directly proportional to the longitudinal stress increment, $d\sigma$, and is a nonlinear function of the longitudinal stress and the current value of damage parameter. The damage parameter increment is calculated using the consistency equation for the bounding surface when the current damage parameter is equal to the maximum value of the damage parameter at the beginning of step. This is always the case for monotonic compressive loading.

If the damage parameter increment cannot be calculated from Eq. 4.18, it is calculated as proposed by (Ameur-Moussa and Buyukozturk, 1990):

$$dK = \frac{d\tau_0}{H^P F_1} \tag{4.19}$$

If the increment of the damage parameter is calculated by Eq. 4.19, it is possible to obtain an exceedingly large value when either of the terms in the denominator is close to zero. In particular, the plastic shear modulus is very close to zero for large values of the damage parameter (see Section 4.4.2). In order to address this problem, the denominator is capped from below in this work, so that it will never be less that a small positive constant. In addition, large values of damage parameter cause the empirical equations of the model to be used beyond their limits of applicability. Since a large value of damage indicates inability of a fiber to resist any load, the fibers with the values of damage parameter greater than 63 are permanently deactivated. This value of damage parameter corresponds to the bounding surface decreasing to one percent of its original size, so that the error introduced by ignoring the compressive capacity of a fiber is small. After the fiber is deactivated, its contribution to the strength and stiffness of the beam-column is neglected, and no further concrete plasticity calculations are performed for that fiber. This corresponds to a physical phenomenon of a concrete volume been pulverized by either large compressive load or repeated application of a smaller load.

4.4.2 Calculation of the Plastic Shear Modulus in the Postfailure Regime

Equations 4.3 and 4.5 require calculation of the plastic shear modulus, H^P. Section 4.3.3 described the calculation of H^P in the prefailure region. In the postfailure region, if only small excursions are to be modeled, then it is possible to define the plastic shear modulus as an empirical expression to calculate the damage parameter increment as a function of the octahedral plastic shear stress increment and the plastic shear modulus. This is, in effect, using the deformation theory of plasticity to supplement the incremental plasticity theory which is used in the prefailure region. This approach does not take into account the loading history, but it can lead to a satisfactory prediction of the material response, provided that the loading is proportional and the strain range covered is relatively small. This approach was chosen by (Ameur-Moussa and Buyukozturk, 1990), who introduced a plastic shear modulus expression to provide a fit to the postfailure branch of experimental uniaxial stress-strain curves. Their equation for the plastic shear modulus in the postfailure region is:

$$H^p = -0.15 \cdot \exp\left[-0.025 \cdot \left(K_{\max} - 1\right)^2\right] \cdot F_2 \tag{4.20}$$

where: F_2 is a multiaxial factor described in Section 4.5

This equation causes the plastic shear modulus to decrease to zero very rapidly with an increase of the value of the maximum damage parameter, $K_{\max}$.

The stress-strain curve obtained with the damage parameter increment calculated using this approach corresponds very closely to the one where the damage parameter increment is calculated from the consistency equation for the bounding surface, as long as the compressive strain is small. In particular, for uniaxial loading, the two curves are very close up to a strain level of about three times the strain at peak stress. After that, the curves diverge, with the difference increasing with an increase in strain.

A corresponding disadvantage of using an empirical expression for the plastic shear modulus to calculate the damage parameter increment is that the tangent predictor of the stress increment leads to the calculation of an updated stress point that does not lie on the bounding surface, since the consistency condition is not enforced if Equations 4.4, 4.5, and 4.20 are used. While it is common in numerical implementations of incremental plasticity theory to calculate an updated stress point that is located slightly off the bounding surface, usually the discrepancies are due to the first order approximations used to obtain the consistency equation. The most common methods to address this problem are either to subdivide the strain increment into a number of smaller subincrements, or to use some sort of a return mapping algorithm (Crisfield, 1991). Subincrementation is similar to reducing the load step, and may be computationally expensive. Alternatively, return mapping algorithms are designed to directly address the problem of the stress point not being located on the surface by modifying either the current stress point or the bounding surface. This insures that the beginning-of-step stress point is always on the bounding surface, as expected in the theoretical development. If a return mapping is not used, the stress point may drift from the bounding surface, and the plastic state determination algorithm will not work properly in the postfailure range.

In the current research, both subincrementation and a return mapping algorithm are used to improve the accuracy of the model prediction. The subincrementation technique is used if the calculated strain increment is greater than a preset value of an allowable strain increment. The number of subincrements is calculated by dividing the calculated strain increment by the allowable value, but may not be less than two. Return mapping is performed in the deviatoric stress plane, with the value of the stress point scaled so that the final stress point lies on the bounding surface. This is analogous to a radial return algorithm commonly used in plasticity models (Crisfield, 1991).

4.5 Calibration to Moment-Curvature-Thrust Results for CFTs

The empirical equation for the plastic shear modulus in the postfailure region proposed in (Chen and Buyukozturk, 1985) was obtained by a curve-fit for the uniaxial stress-strain experimental curves. Consequently, it does not allow for the different slopes of the postfailure branch of the stress-strain curves to be predicted. In the revised version (Ameur-Moussa and Buyukozturk, 1990) of the model, the original equation is multiplied by a multiaxial factor, F_2, as seen in Eq. 4.20. This factor is a function of the first stress invariant:

$$\begin{aligned} F_2 &= \frac{0.14}{I_{1,\max}^2 - 0.86}, \quad I_{1,\max} \le 2.54 \\ F_2 &= 0.025, \qquad\qquad I_{1,\max} > 2.54 \end{aligned} \tag{4.21}$$

where: $I_{1,\max}$ is the maximum value of the first stress invariant ever experienced by the material fiber

The purpose of this factor is to account for the change of the postfailure slope due to confinement of the concrete. Its value varies between 1.0 for unconfined concrete and 0.025 for highly confined concrete.

The slope of the descending branch of the concrete stress-strain curve primarily influences the ductility of the beam-column. If the slope is steep, the total cross-sectional rigidity becomes equal to zero after enough concrete fibers reach the postfailure stage. Zero cross-sectional rigidity leads to an indefinite stiffness matrix for a beam-column. Therefore, exercising some control over the slope of the postfailure branch is essential for successfully modeling CFT response.

The softening response of concrete should be properly considered at a structural level, rather than at a continuum level (Chen and Han, 1986). Therefore, it is appropriate to consider the member structural parameters in calculating the postfailure response of a concrete fiber. The main cause of the variation of the slope of the concrete stress-strain

curve in the postfailure range is the different degree of confinement exerted by the steel tube. If circumferential stresses and strains are calculated explicitly in the analysis, then their values may be used to calculate the multiaxial factor, F_2. Alternatively, the confinement may be accounted for approximately by making the slope of the descending branch of the stress-strain curve a function of the element structural parameters. This approach was chosen for the current research.

The experimental moment-curvature-thrust diagrams reported in (Tomii and Sakino, 1979) were selected to calibrate the postfailure slope of the concrete. Moment-curvature-thrust response was selected for calibration rather than pure axial stress-strain response since flexure is an important and dominant component of behavior in CFT beam-columns. The value of F_2 parameter was selected so as to provide good correspondence with the experimental results, as well as to provide a sufficient level of curvature ductility. The experimental results used for the calibration included two groups of beam-columns, each loaded first with a constant axial force, and then in flexure with a uniform bending moment. For the first group, the ratio of steel tube depth to steel thickness, D/t, was equal to 24; for the second group this ratio was equal to 44. Each group consisted of five square CFT beam-columns, with nearly identical geometric and material properties. The steel tubes where annealed and had yield stresses ranging from 280 to 340 MPa. The concrete strength was approximately 25 MPa. The ratio of applied axial force to the axial capacity of the CFT members, P/P_0, was the varying parameter within each group.

The moment-curvature-thrust diagrams of the CFT members from the first group exhibited positive slope for the duration of the experiment. The initial elastic slope was followed by a rounded transition zone and an elasto-plastic region with a small positive slope. For all specimens but the one with the highest axial force, no failure points were reported, and thus it is believed that the actual ultimate ductility level is higher than the cut-off value used for the plots in (Tomii and Sakino, 1979). The downward slope of the concrete for this group of columns was chosen to provide the curvature ductility level at least equal to the values reported.

The specimens from the second group all had moment-curvature-thrust diagrams with an ascending portion, a peak moment, and a descending branch. For these beam-columns, the peak points on the moment-curvature-thrust diagrams correspond to the limit points on the force-deformation curves. In this work, no attempt has been made to model the downward slope of the moment-curvature-thrust diagrams. Instead, the downward slope of concrete was selected to provide enough curvature ductility to reach the peak moment.

While it is possible to have the F_2 parameter vary as a function of the D/t ratio, it was found that a constant value of 0.05 was sufficient to obtain a good prediction of all of the experimental moment-curvature-thrust results for both groups of CFTs. For the first group, an entire moment-curvature-thrust relation is predicted accurately for all specimens (see Figure 4.1). For the second group, the level of curvature corresponding to the peak moment is predicted in the average sense (see Figure 4.2). Thus, although the predicted value of curvature is less than the experimental value for some CFTs, and more for the other CFTs, a modification of the F_2 parameter will not improve the results. Therefore, a constant value of F_2 equal to 0.05 is used for all analyses in this work.

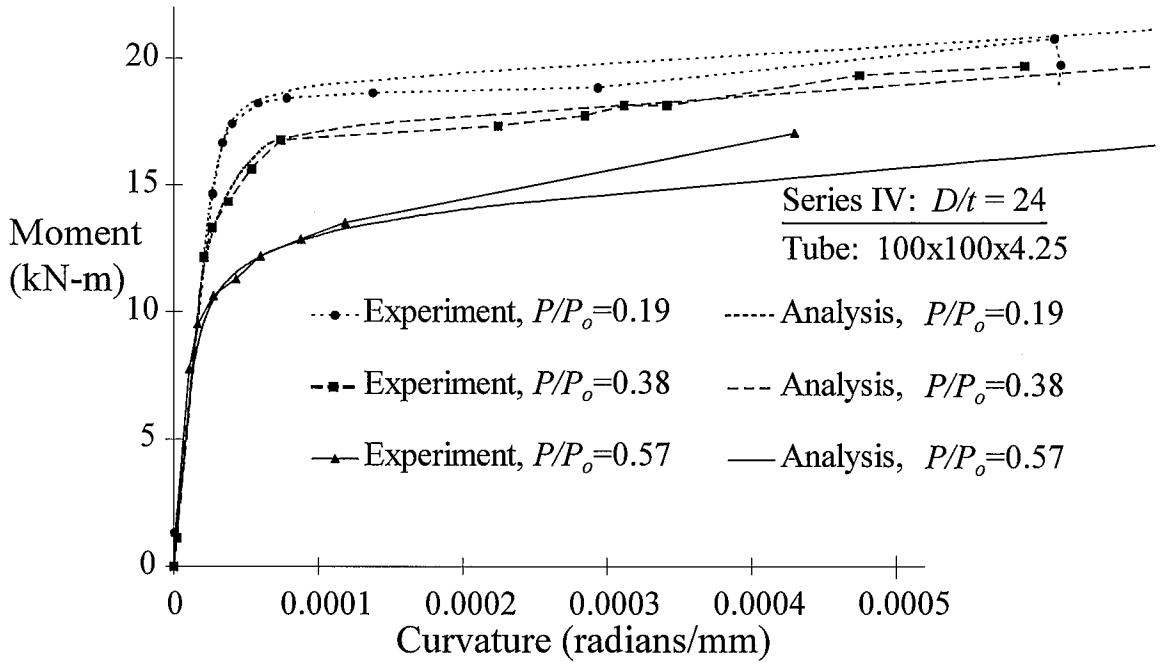

Figure 4.1: Comparison of Experimental and Computational Moment-Curvature-Thrust Diagrams for CFTs with D/t Equal to 24.

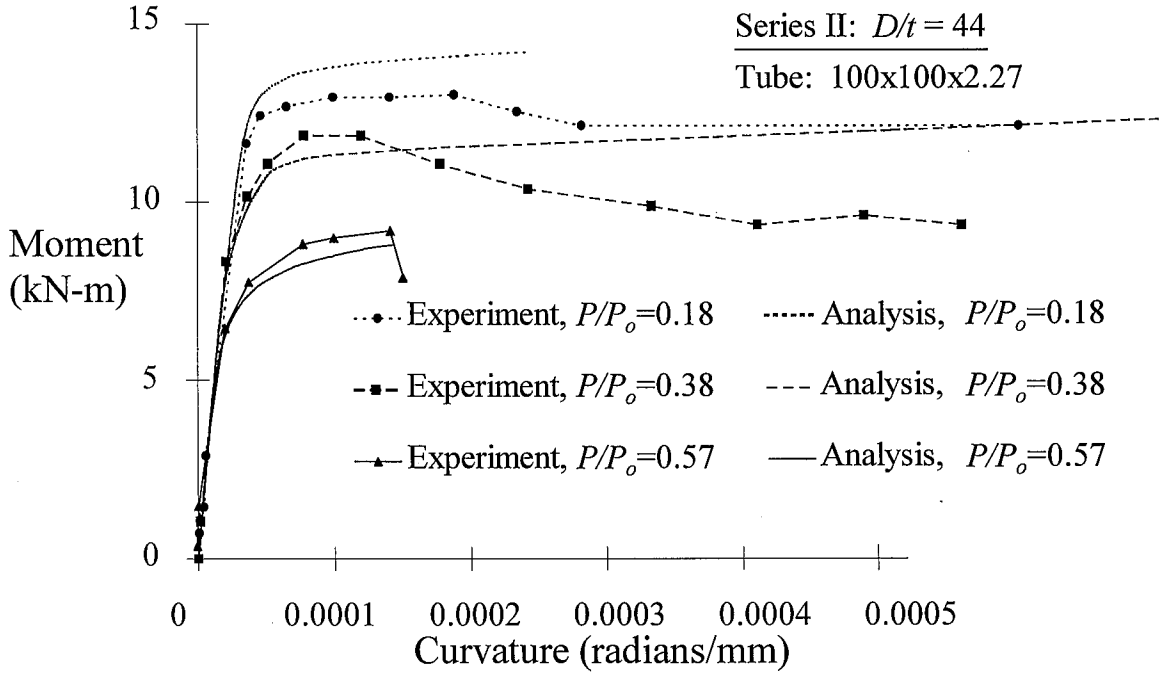

Figure 4.2: Comparison of Experimental and Computational Moment-Curvature-Thrust Diagrams for CFTs with D/t Equal to 44.

Chapter 5

Verification

This chapter describes verification of the CFTFiber program. The program is verified by comparing computed structural response of CFT members to available experimental data. Both monotonic and cyclic experiments are used for comparison. Particular emphasis is placed on the verification of cyclic behavior.

The geometrically nonlinear formulation employed in the CFTFiber program was verified by comparing the predicted response of elastic steel wide flange and CFT elements to analytical solutions and published benchmark problems (Schiller and Hajjar, 1996). The results were found to be in agreement in all cases.

5.1 Monotonic CFT Experiments

Verification of the CFT fiber element was performed by comparing the finite element results to over thirty different experimental studies of CFT beams, eccentrically loaded beam-columns, nonproportionally loaded beam-columns, and composite frames composed of steel I-girders framing rigidly into CFT columns, holding all calibration parameters fixed (Schiller and Hajjar, 1996). Experimental verification studies were selected to provide data for CFTs having a wide range of parameters, such as material strengths, D/t ratio, L/D ratio, and the method of applied loading (Gourley et al., 1995).

Figures 5.1a through 5.1h show the comparison between the fiber model and experimental monotonic load-deflection curves for several of the verification studies [details of each test are provided in Table 5.1 and (Hajjar et al., 1997b)]. Each test is referenced by the nomenclature of the experimentalist. Figures 5.1a and 5.1b are beams loaded in pure flexure by point loads, including both major and minor axis bending. Figures 5.1c-5.1f are eccentrically loaded beam-columns, including comparisons to tests from three different experimentalists. These four examples include both stocky and slender beam-columns subjected to uniaxial or biaxial bending, for a range of material strengths. Figures 5.1g and 5.1h (Tomii and Sakino, 1979) are annealed specimens which are loaded nonproportionally, with varying levels of constant axial force being applied in the different tests (in the table, P_0 is the ultimate axial strength of the member), followed by application of bending moment.

For the verification studies, ten fibers were used in each flange of the steel tube (with one fiber through the tube thickness), and the concrete core was meshed with a 10 by 10 grid of fibers. Four elements were used along the length of each member.

5.1 Cyclic CFT Experiments

Figure 5.2 compares the computational results to the data from two of the cyclic tests of Sakino and Tomii (1981), one with a *D/t* of the steel tube of 24, the other with a *D/t* of 34. The test setup is similar to that of Fig. 3.1. The steel tubes are annealed. Ten fibers were used in each flange of the steel tube (with one fiber through the tube thickness), and the concrete core was meshed with a ten by ten grid of fibers. Twelve elements were used along the length of the member. The axial force is held constant at a level of $P/P_o = 0.2$ ($P_o = 729$ kN) for the test of Fig. 5.2a, and at a level of $P/P_o = 0.3$ ($P_o = 528$ kN) for the test of Fig. 5.2b. Note that Sakino and Tomii continued these experiments to higher deformation levels. However, substantial local buckling of the steel tube occurred at the

Table 5.1: Concrete-Filled Steel Tube Monotonically Loaded Verification Experiments

Test (Specimen)	Actual Tube Dimensions (mm)	D/t major (minor)	L/D major (minor)	f_c' (MPa)	f_y (MPa)	Other data
Lu and Kennedy, 1994 (CB33)	253.4x152.0x 6.17	39.7 (23.75)	12 (20)	45.2	377	Major axis bending; P=0; load applied 766 mm from each end of 3040 mm beam
Lu and Kennedy, 1994 (CB53)	253.4x152.0x 6.17	39.7 (23.75)	8.8 (14.7)	42.1	377	Minor axis bending; P=0; load applied 463 mm from each end of 2231 mm beam
Bridge, 1976 (SHC-1)	203.7x203.9x 9.96	20	10.5	29.9	291	e = 38 mm [1]
Cederwall et al., 1991 (10)	120x120x8	15	25	39	397	e = 20 mm
Bridge, 1976 (SHC-5)	202.6x203.2x 10.0	20	15	44.3	319	e = 38 mm $\alpha = 30°$ [2]
Shakir-Khalil and Zegiche, 1989 (6)	120x80x4.47	24 (16)	23 (24.5)	45	343.3	e_{major} = 24 mm e_{minor} = 16 mm
Tomii and Sakino, 1979 (III-3)	100x100x2.99	33	3	20.6	289	P/P_0 = 0.30 Annealed tube
Tomii and Sakino, 1979 (III-6)	100x100x2.99	33	3	20.6	289	P/P_0 = 0.60 Annealed tube

[1] Eccentricity of applied axial load from centroidal axis of member

[2] Angle of applied axial load with respect to major principal axis of cross-section (i.e., $\alpha = 0°$ induces minor axis bending)

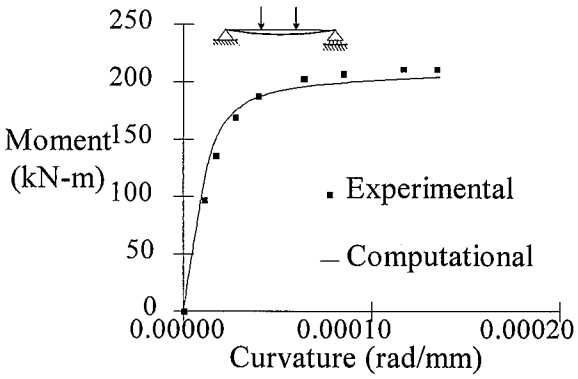

a) Lu and Kennedy (1994), Specimen CB33

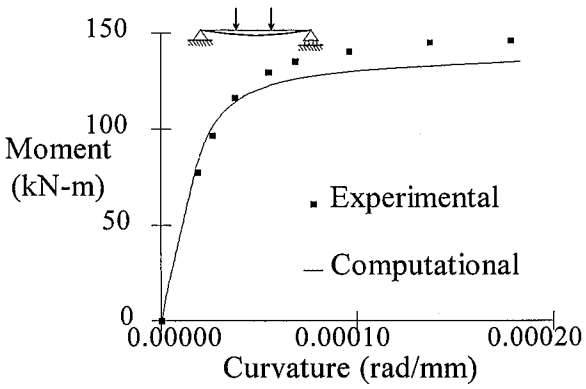

b) Lu and Kennedy (1994), Specimen CB53

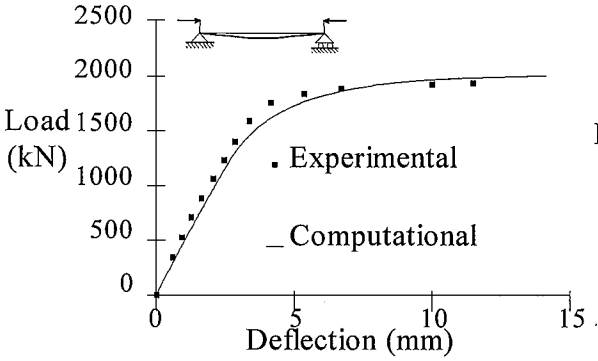

c) Bridge (1976), Specimen SHC-1

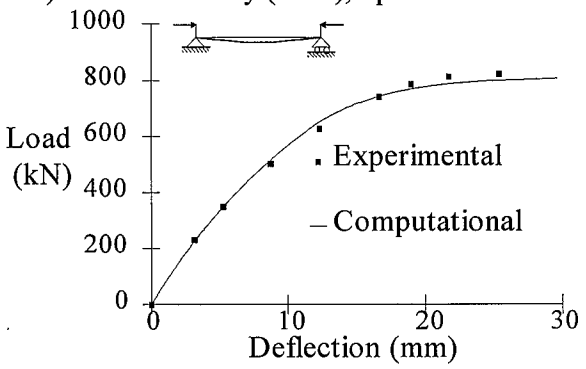

d) Cederwall et al (1991), Specimen 10

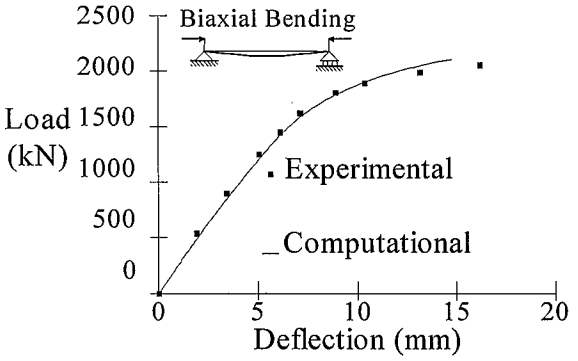

e) Bridge (1976), Specimen SHC-5

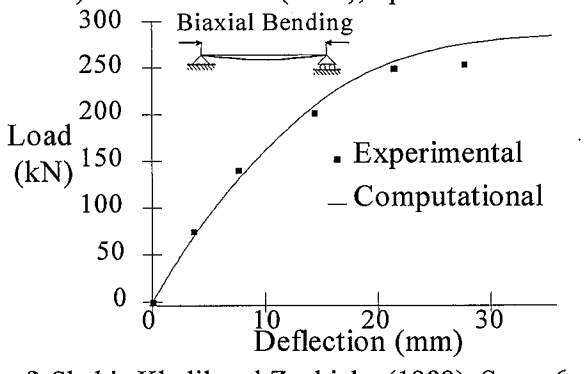

f) Shakir-Khalil and Zeghiche (1989), Spec. 6

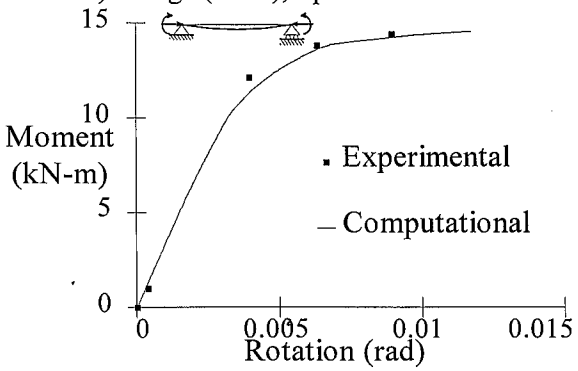

g) Tomii and Sakino (1979), Specimen III-3

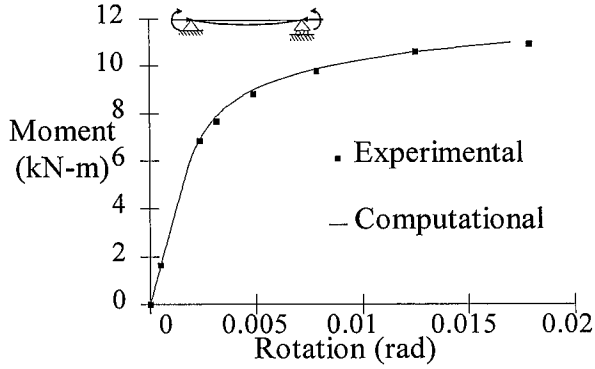

h) Tomii and Sakino (1979), Specimen III-6

Figure 5.1: Comparasion of Monotonic Loading Results

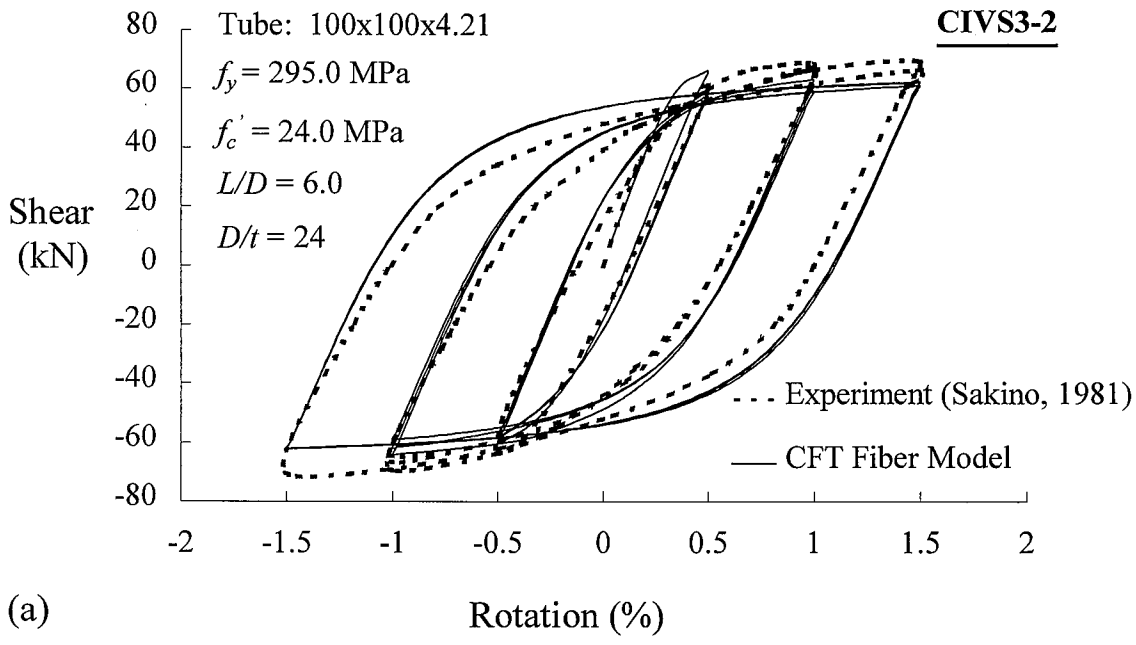

(a)

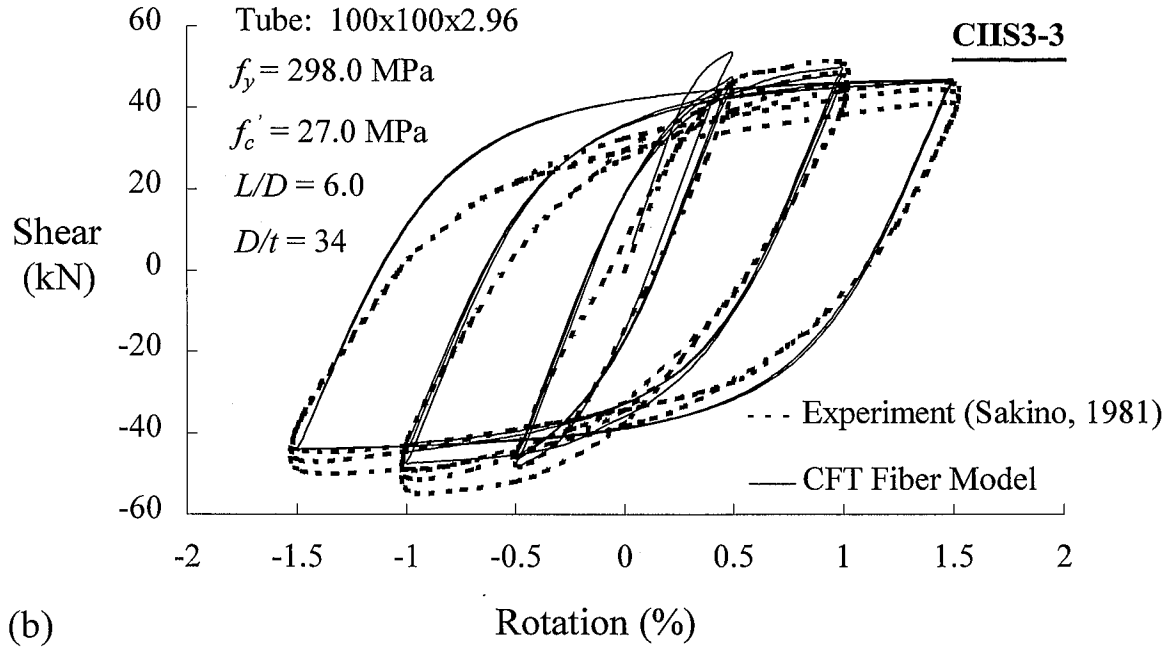

(b)

Figure 5.2: Comparison of Cyclic CFT Experimental and Computational Results

higher levels of chord rotation. Capability of modeling local buckling is pending in the fiber model; since the present formulation does not model local buckling, the comparison to these experiments was terminated at the points at which significant local buckling occurred in the tests.

5.3 Three-Dimensional Cyclic CFT Subassemblage

To verify the capability of analyzing composite subassemblages, the final verification problem consists of a three-dimensional subassemblage of steel I-girders framing rigidly into a CFT beam-column. The setup of the experiment, performed by Morino and his colleagues (Kawaguchi et al., 1991b; Morino et al., 1993), is shown in (Fig. 5.3). The specimen, labeled SCC20 (Morino et al., 1993), was designed such that the CFT beam-column, rather than the fully-restrained connections, would reach its limiting capacity first, while the steel beams were designed to remain elastic for the duration of the experiment. The CFT was loaded first with a constant value of axial load, $P = 0.15P_0$ (P_0 = 1300 kN for this specimen), while simultaneously a constant load of $W = 21.0$ kN was applied to one end of the steel beam in the Y-Z plane (see Fig. 5.3a). The specimen was then loaded cyclically in the X-Z plane. The anti-symmetric beam shear forces, Q, were varied to obtain increasing increments of rotation, R, equal to 0.005, 0.01, and 0.02, and 0.03 radians. For each rotation increment, two full cycles of loading were performed. This loading pattern created a combination of cyclic biaxial bending and axial force in the CFT beam-column.

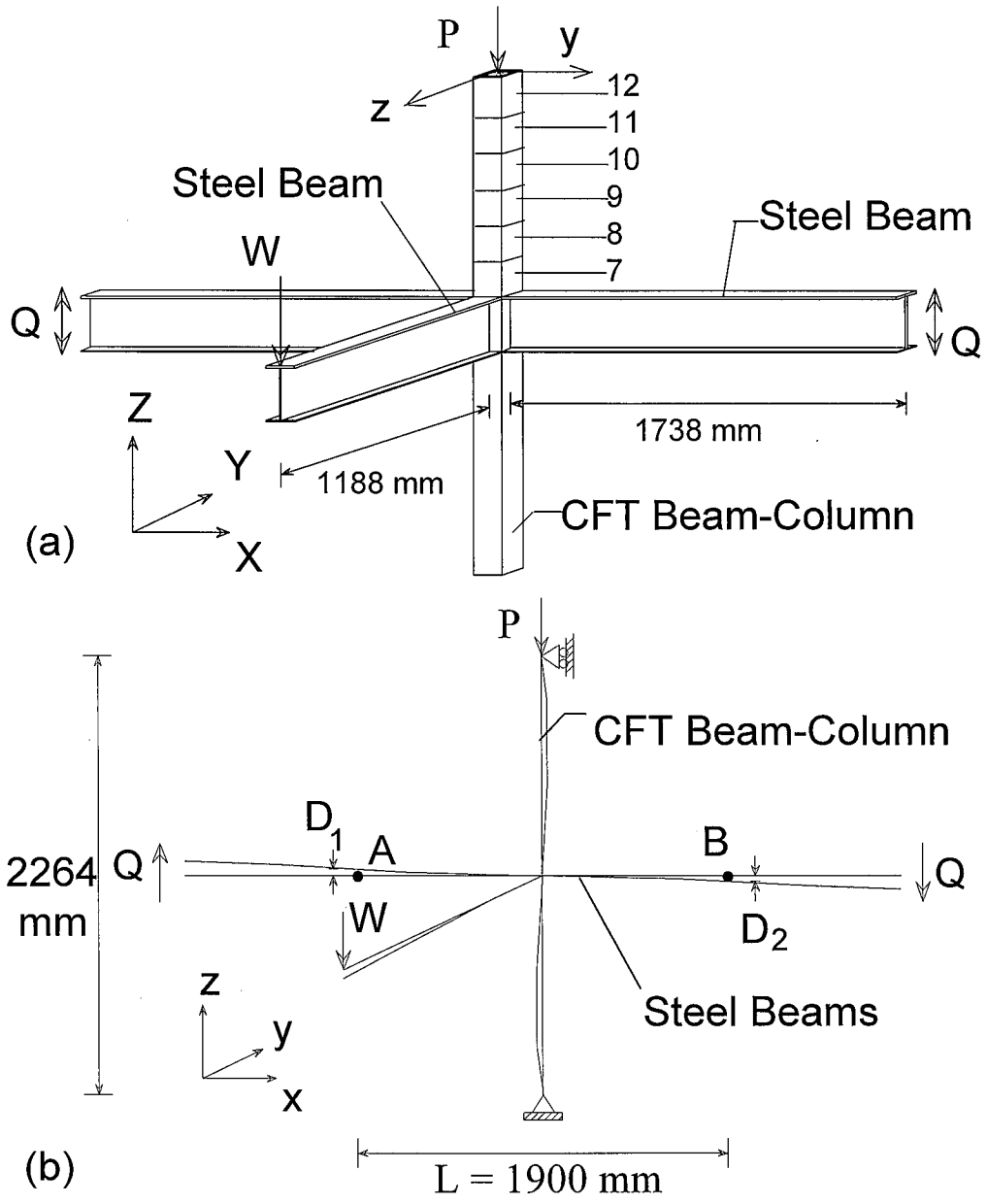

Figure 5.3: Three-Dimensional Composite CFT Subassembly (Morino et al., 1993)

The CFT beam-column consists of a square tube with cross-section dimensions $125 \times 125 \times 5.74$ and material strengths of $f_c^{'} = 20.0$ MPa and $f_y = 395$ MPa. The steel I-beams are built-up sections consisting of flanges measuring 125×9 mm and a web measuring 231×6 mm, and having a yield strength of $f_y = 400$ MPa. Figure 5.3b

illustrates a schematic representation of the computational model of the subassemblage. The drift rotation is calculated by summing the displacements, D_1 and D_2 at locations A and B, respectively, and dividing by the length L between these points, thus simulating the approach used by the experimentalists. Both the connection rotation and the beam flexure between the connection and the measuring points, A and B, contribute to the calculated values of the drift rotation. The beam shear shown in the results is calculated by averaging the values of shear forces in the X-Z planes at both ends of the beam. These forces, although close in value, are not equal, due to the boundary conditions and axial displacement of the CFT beam-column. Ten fibers were used in each flange of the steel tube (with one fiber through the tube thickness), and the concrete core was meshed with a ten by ten grid of fibers. Twelve elements were used along the length of the member, and two steel wide-flange fiber elements were used for each steel beam. Since the steel elastic modulus was not reported for the experiment, a value of 210 GPa was selected to provide a match to the initial elastic slope in the first half-cycle of loading. In addition to the boundary conditions shown at the ends of the CFT beam-column in Fig. 5.3b, each beam had its out-of-plane translation restrained. The CFT element numbering is shown in Fig. 5.3a, while fiber numbering scheme is shown in Figure 5.4. All cross-sectional quantities discussed in the rest of this chapter refer to the bottom cross section of any referenced element.

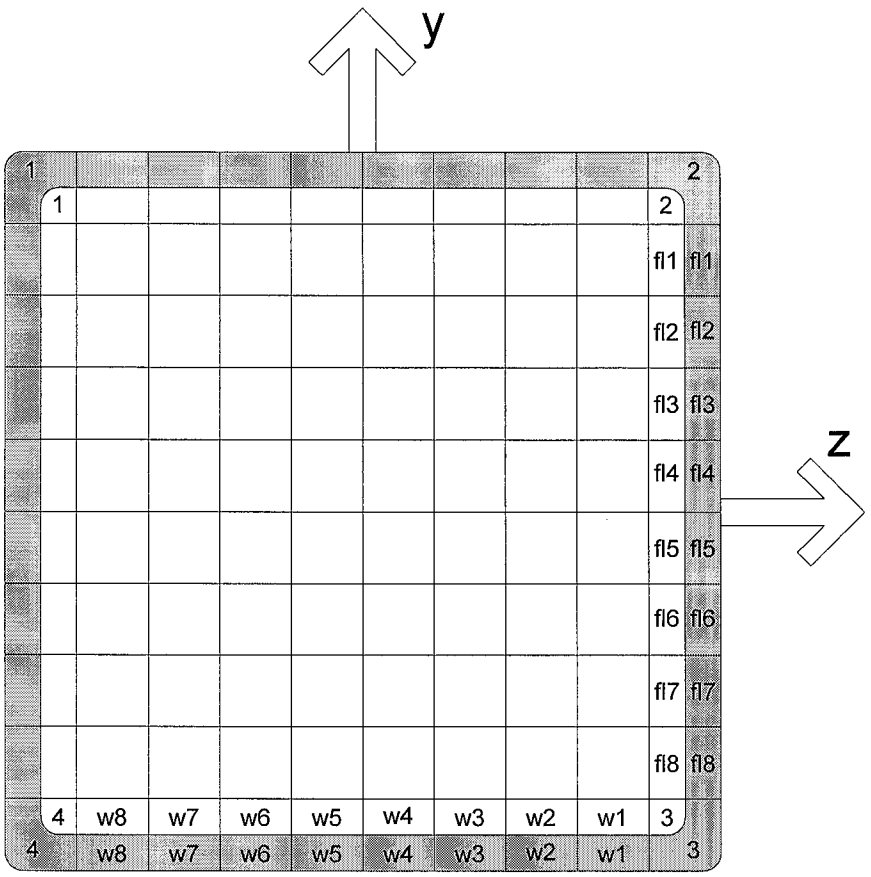

Figure 5.4: Cross Section Fiber Numbering

Figure 5.5 illustrates the CFT fiber model results compared to the experimental results provided by Morino et al. (1993). All calibration parameters were held at their previously established values. The entire hysteresis curve is predicted well by the fiber model, with the stiffness prediction being particularly accurate throughout the loading history. While the maximum shear capacity is somewhat underpredicted by analysis, with the largest error being approximately 13% at a rotation level of 0.03 radians, the overall shear capacity is predicted well, with the error significantly below its maximum level for most of the analysis.

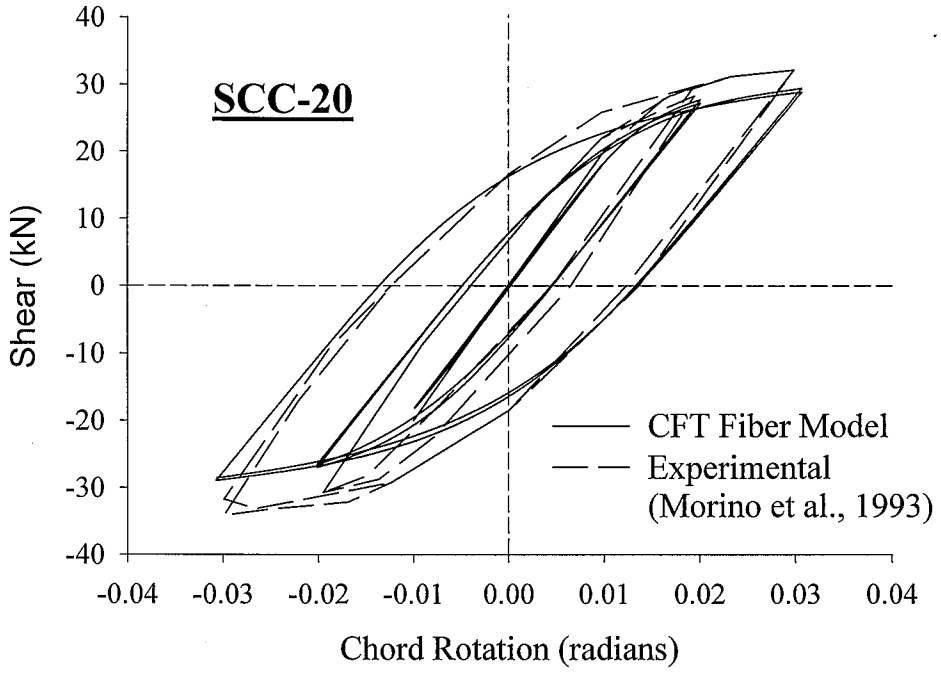

Figure 5.5: Comparison of Experimental and Computational Shear-Rotation Hysteresis Curve for Three-Dimensional Subassembly

In order to provide additional insight into the structural behavior of the CFT beam-column and illustrate the capabilities of the computational model, several computed quantities are plotted for the entire load history. The moment-curvature relations at four different cross-sections of the CFT beam-column are plotted in Figure 5.6. Wide hysteresis loops, indicating significant energy dissipation through the inelastic steel and concrete behavior, are observed for Element 7, where the moment is the largest. The loops become much narrower and the curvature range decreases for Element 8, while the moment magnitude is reduced to a lesser extent. The moment-curvature relation become very close to linear for Elements 9 and 10. The decrease in curvature range and the inelastic energy dissipation are seen to occur at a higher rate than is a decrease in the maximum moment in the cross section.

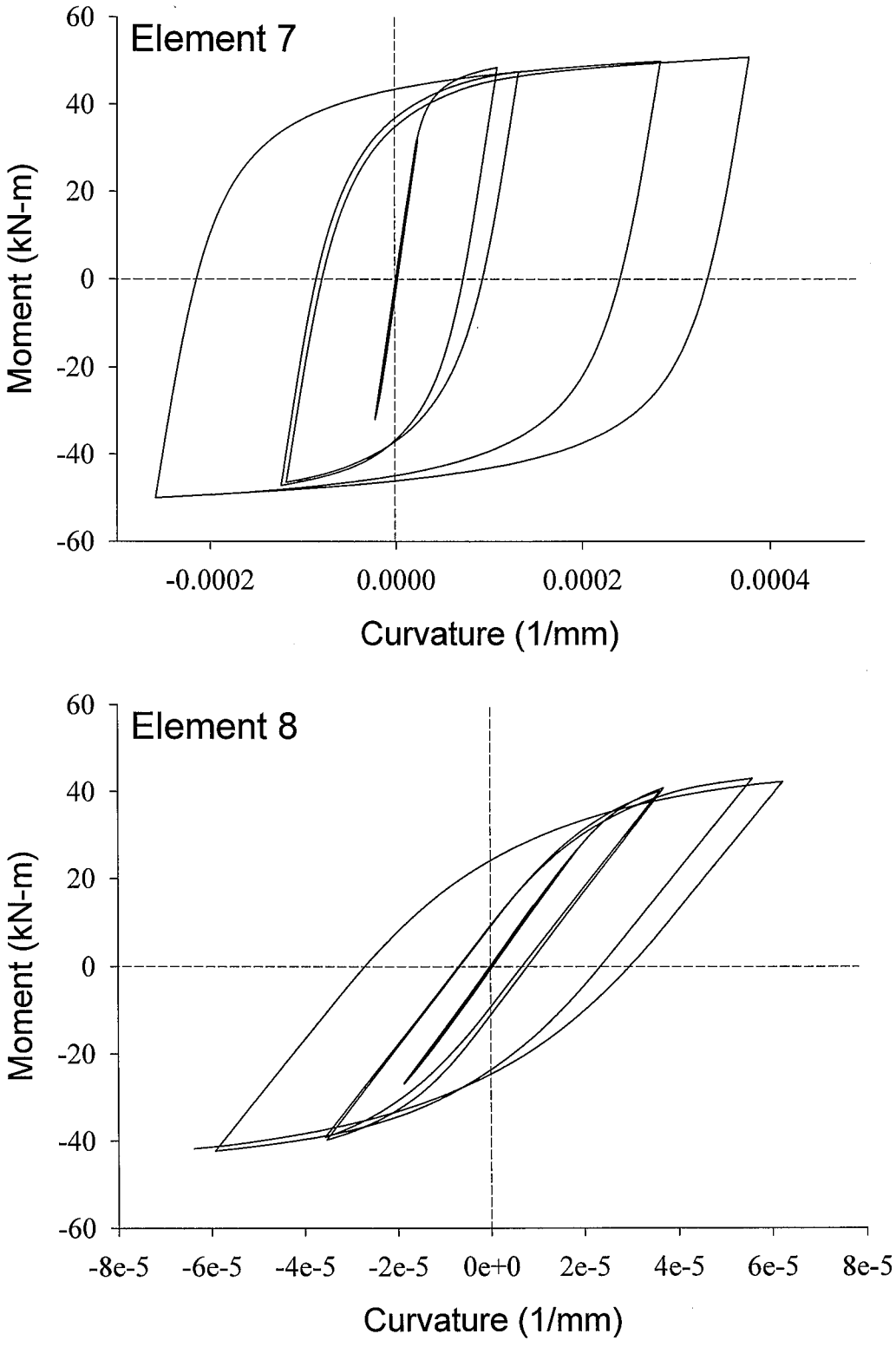

Figure 5.6: Moment-Curvature Relations

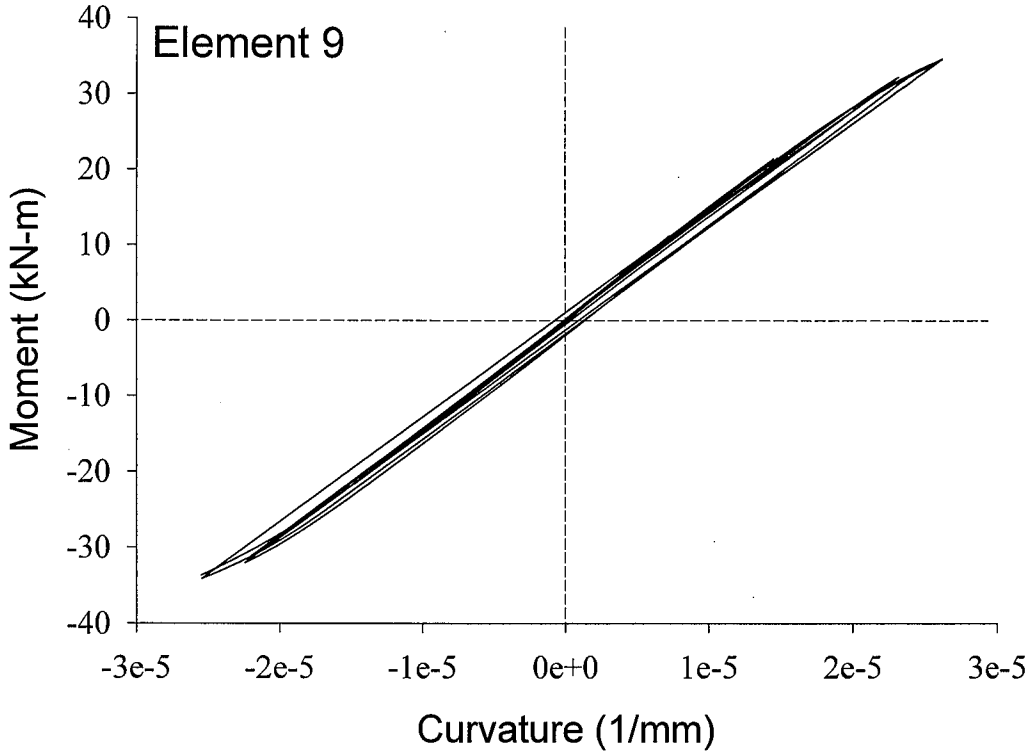

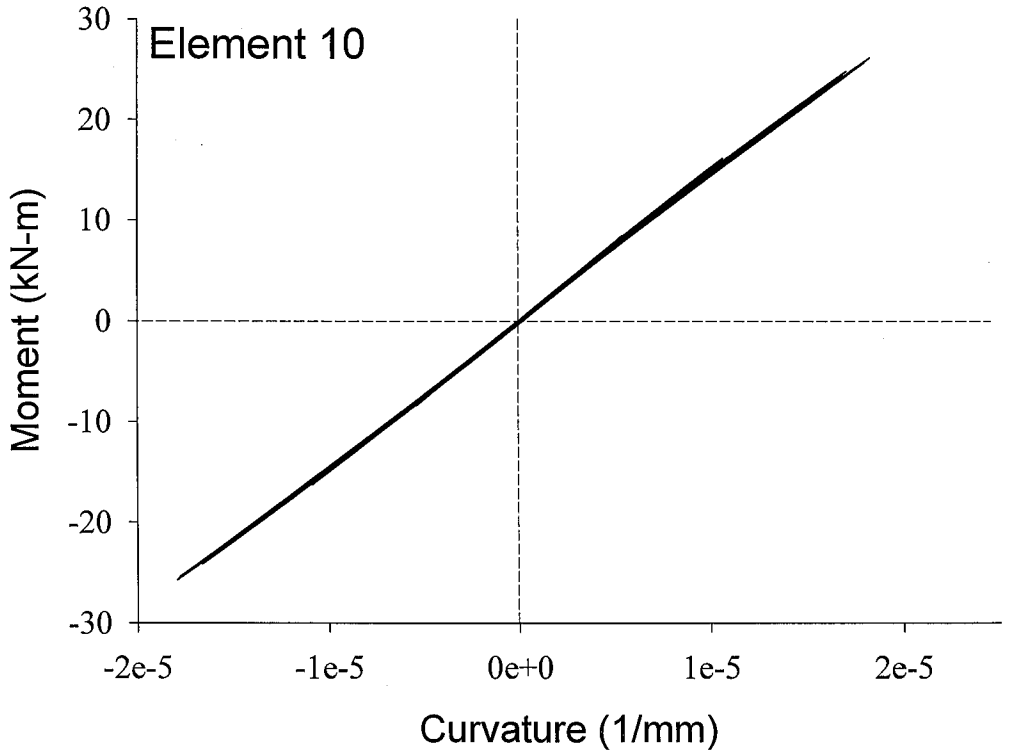

Figure 5.6: Moment-Curvature Relations (continued)

Stress-strain histories of the steel corner fibers are shown in Figure 5.7 for Element 7, and in Figure 5.8 for Element 8. The scale for each graph is selected to show the entire range of stress and strain experienced by the fibers, so that different graphs have different scales. Fibers 2 and 3 are mostly in compression due to the combined effect of the axial load and out-of-plane tip load. Axial load produces compression in Fibers 1 and 4, while the moment created by the tip load produces tension in these fibers, so that these fibers have a near zero mean strain during cyclic loading.

Several features of the cyclic steel plasticity model described in Chapter 3 can be observed from these graphs. A rounded elasto-plastic transition zone can be clearly observed for Fiber 1, Element 7, as well as the increased roundness of the loops with the increase of the strain magnitude. Also, when loading in one direction is followed by unloading with a small excursion into inelastic range, and then by reloading in the original direction, the reloading curve follows the path of original loading. While there is a rounded transition zone, no overshooting is observed, as can be seen most clearly in the stress-strain plot for Corner 2, Element 7. When the fiber is cycled with a nonzero mean stress, a small amount of ratchetting is predicted by the model, as seen in Fibers 2 and 3, Element 8.

Comparison of the stress-strain plots for Fiber 1 in Elements 7 and 8 shows that while the shape of the loops are similar, the fiber from Element 7 (at the midheight of the CFT column) experiences a noticeably greater amount of inelastic action. A similar conclusion can be drawn by comparing other corresponding fibers from Elements 7 and 8. Thus it can be seen that the amount of inelastic action in the fibers directly corresponds to the width of the hysteresis loops of the moment-curvature diagrams, discussed earlier, as expected.

Stress-strain histories of the concrete corner fibers are shown in Figure 5.9 for Element 7, and in Figure 5.10 for Element 8. The scale for each graph is selected to amplify the regions of interest, so that different graphs have different scales and show a different range of the loading history. Fiber 1, Element 7 undergoes several compression-tension cycles, followed by mostly monotonic compressive loading, where it loses most

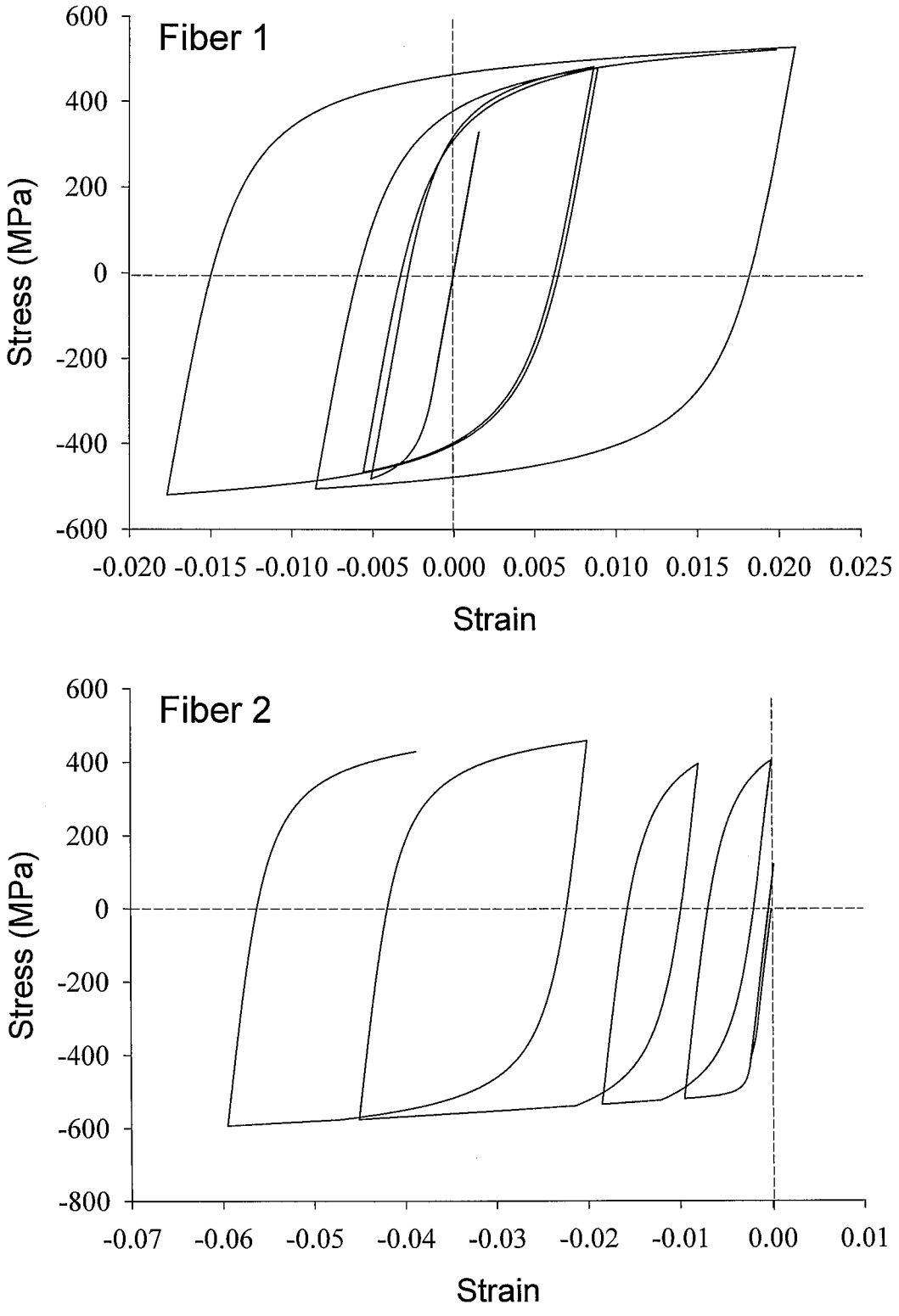

Figure 5.7: Corner Steel Fibers, Element 7

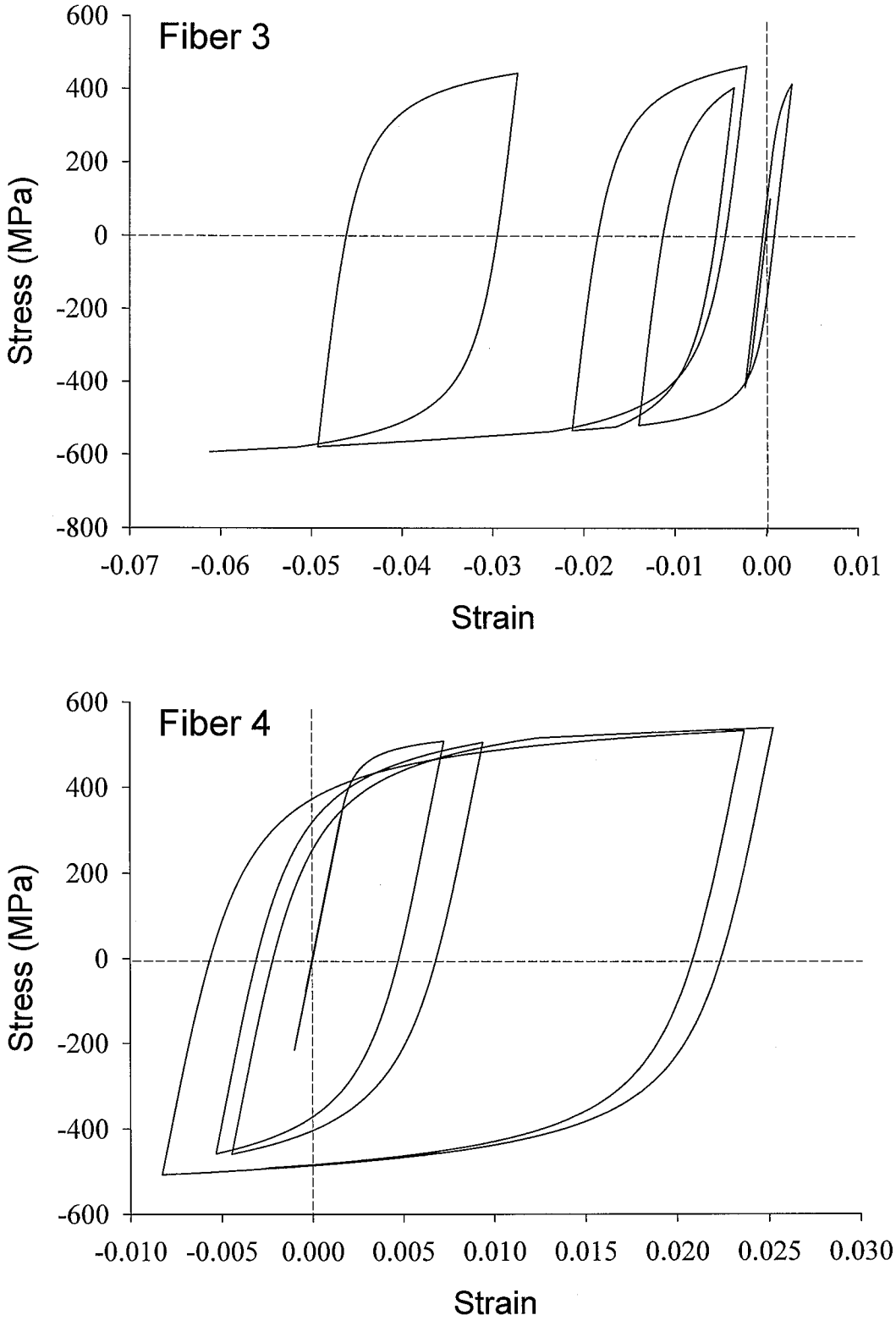

Figure 5.7: Corner Steel Fibers, Element 7 (continued)

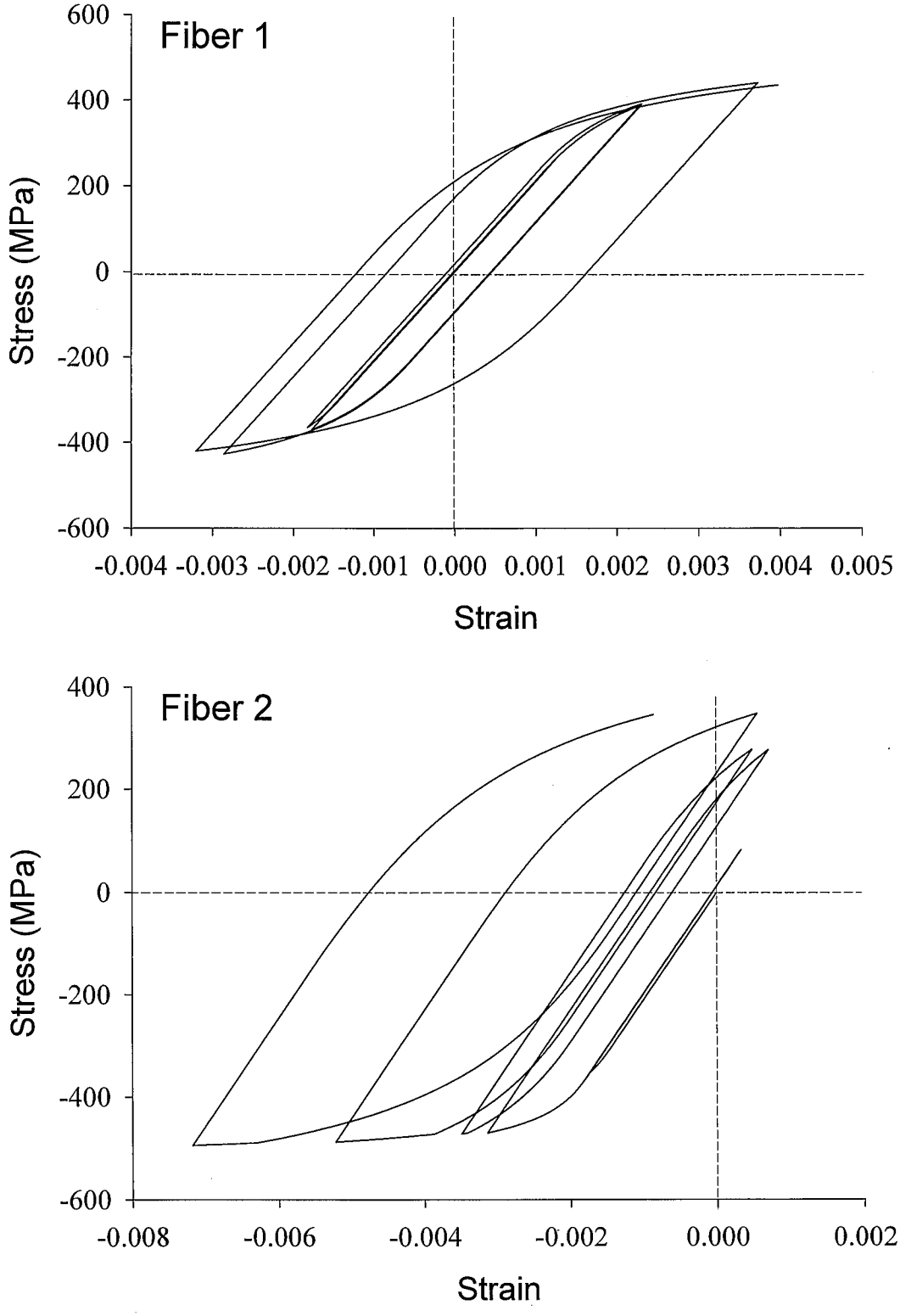

Figure 5.8: Corner Steel Fibers, Element 8

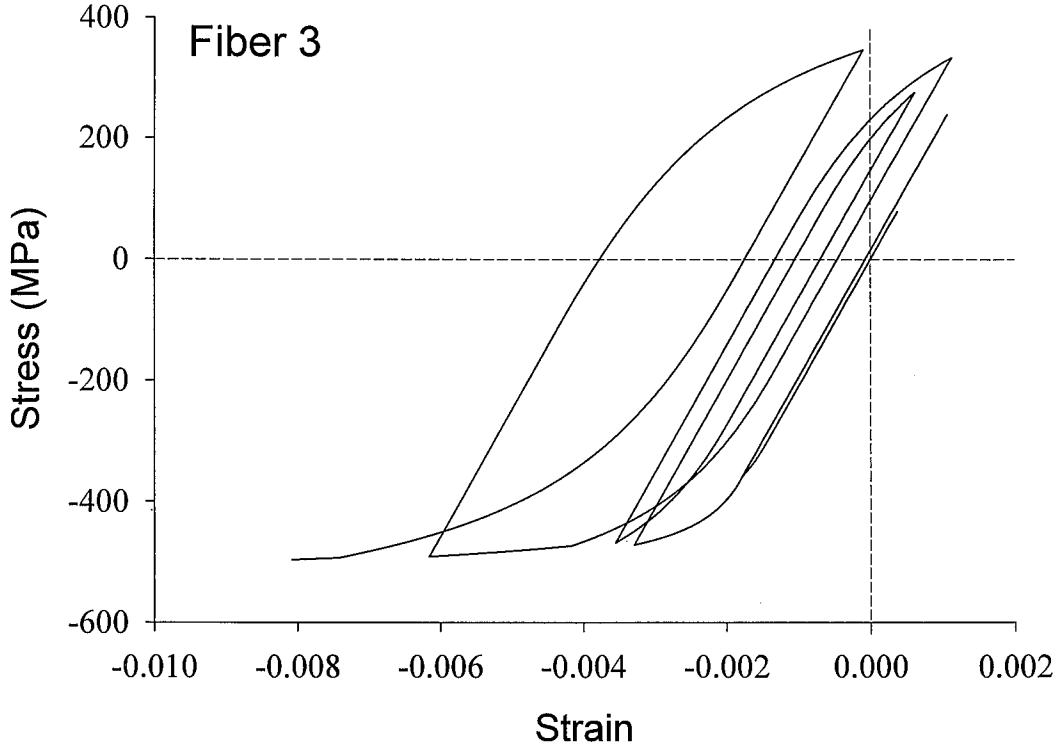

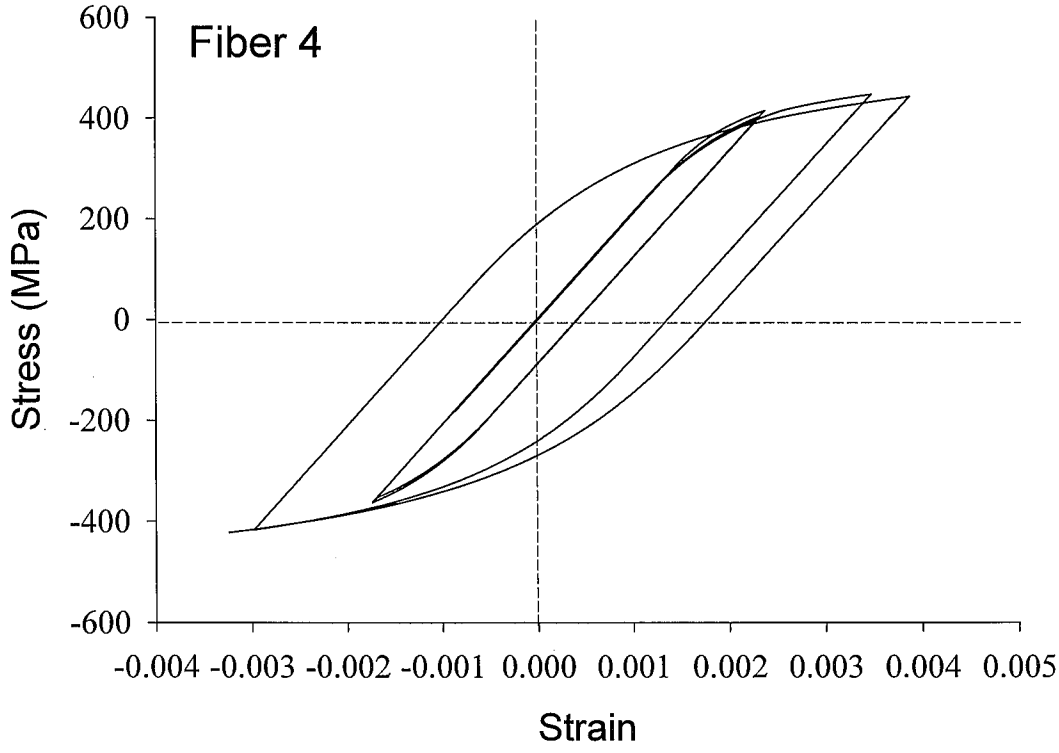

Figure 5.8: Corner Steel Fibers, Element 8 (continued)

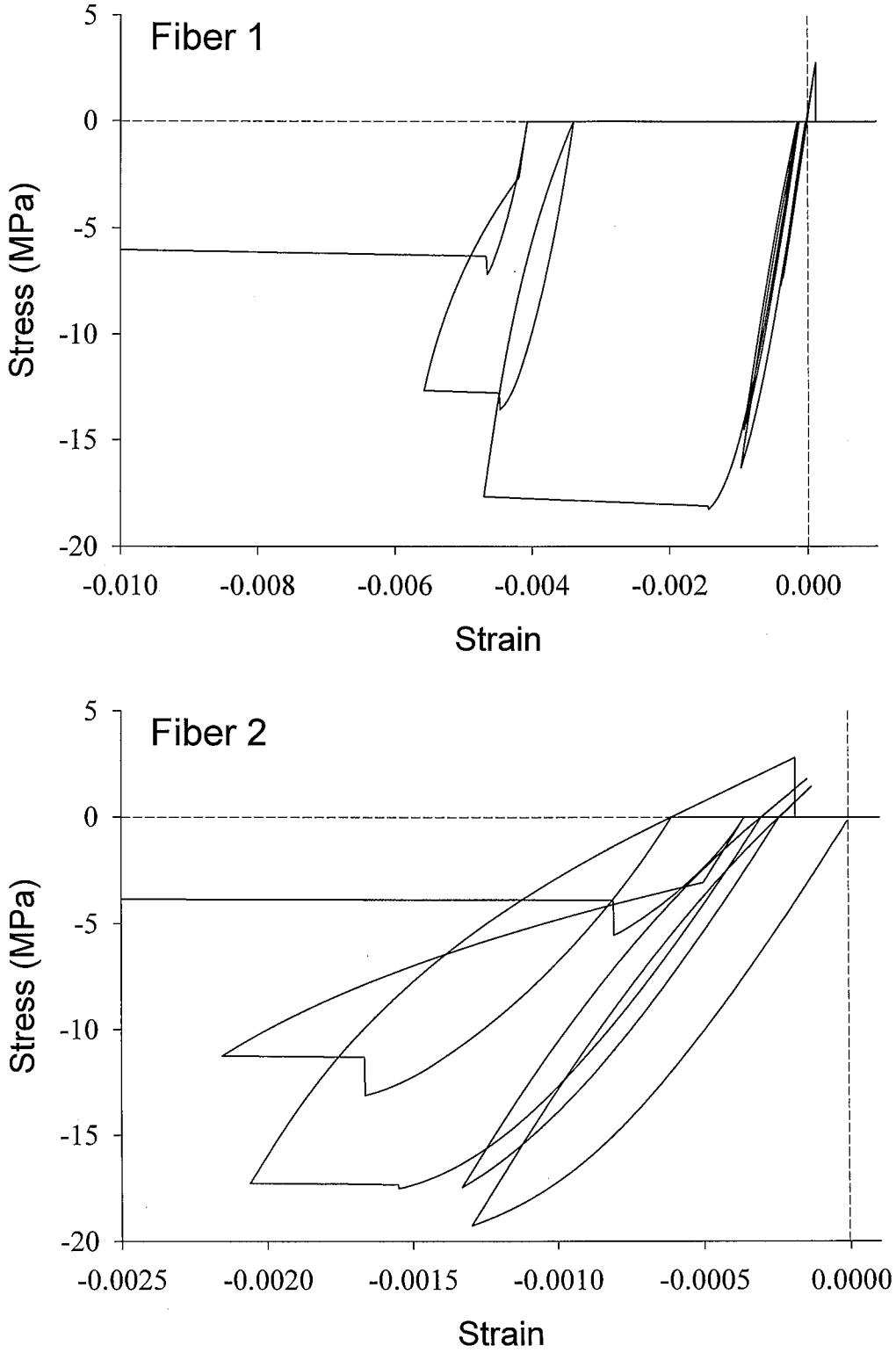

Figure 5.9: Corner Concrete Fibers, Element 7

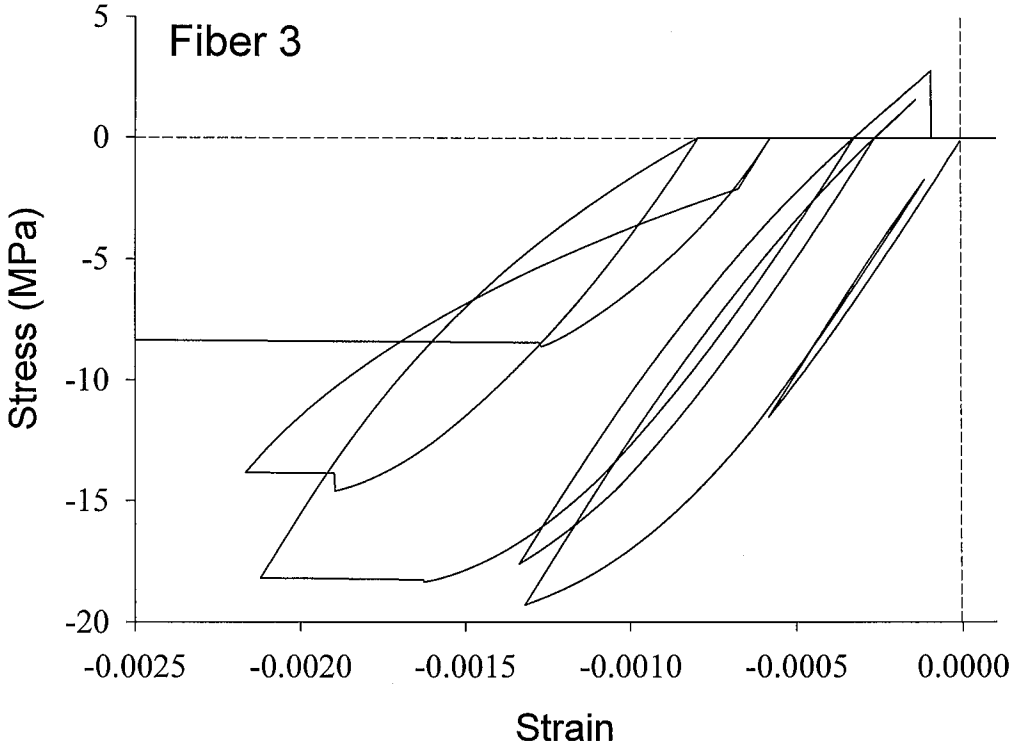

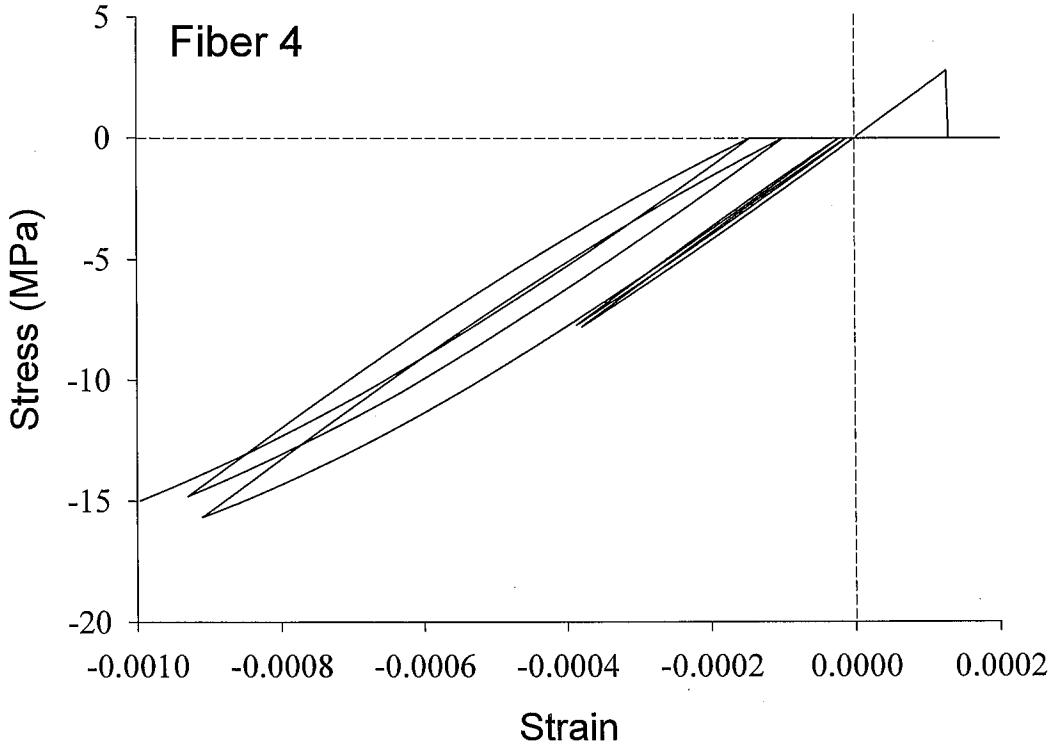

Figure 5.9: Corner Concrete Fibers, Element 7 (continued)

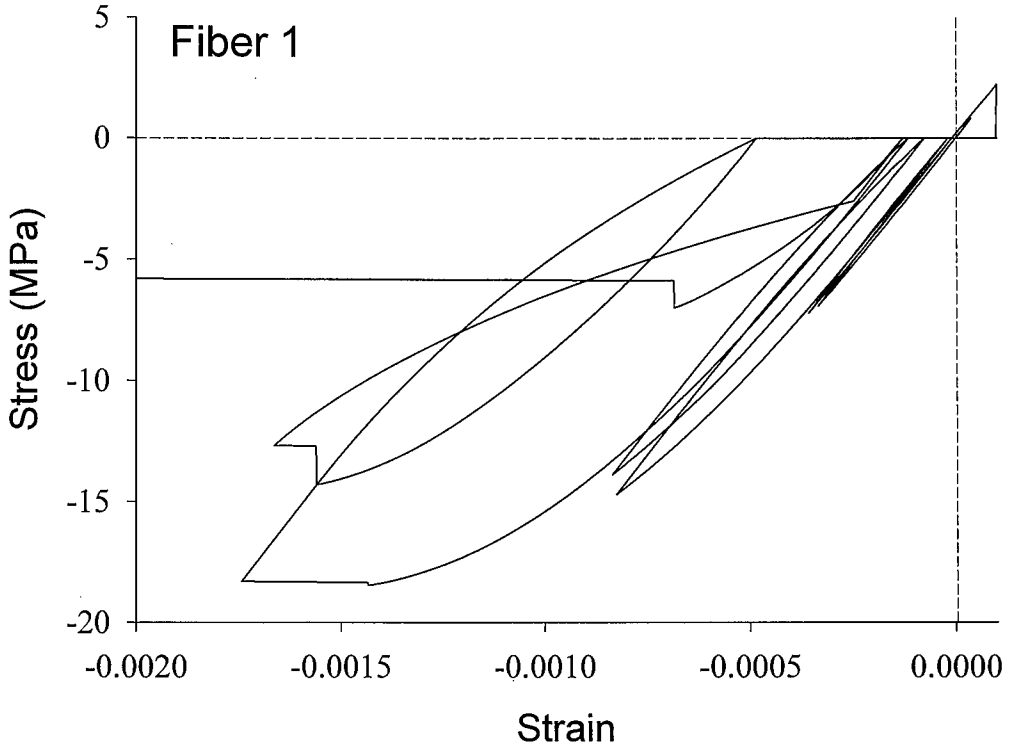

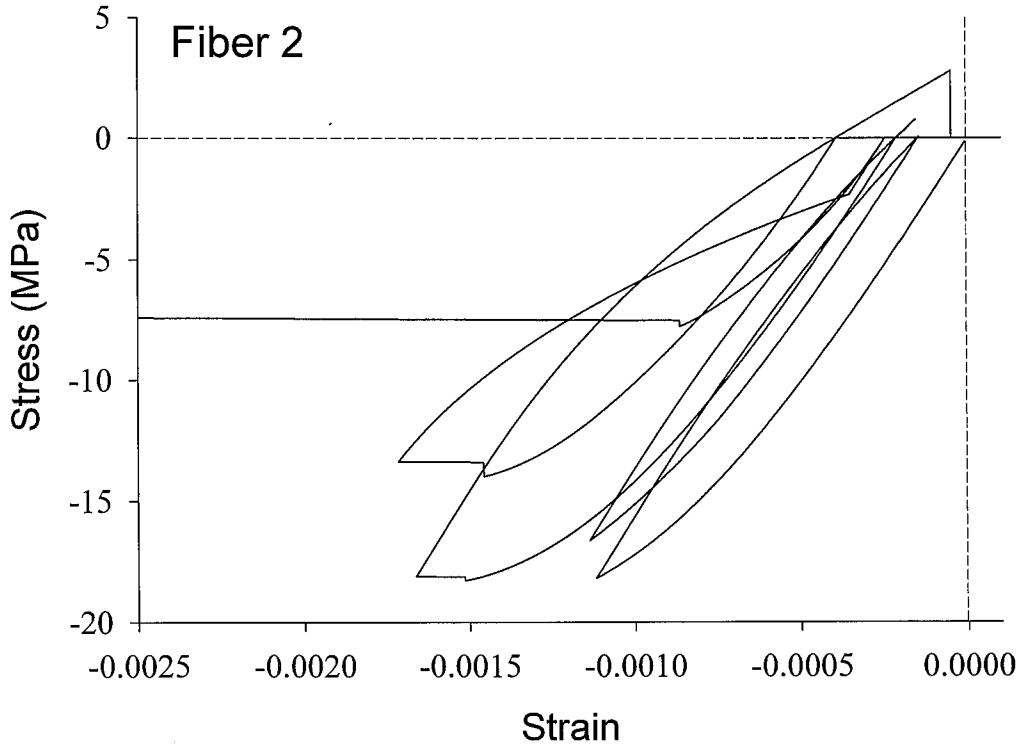

Figure 5.10: Corner Concrete Fibers, Element 8

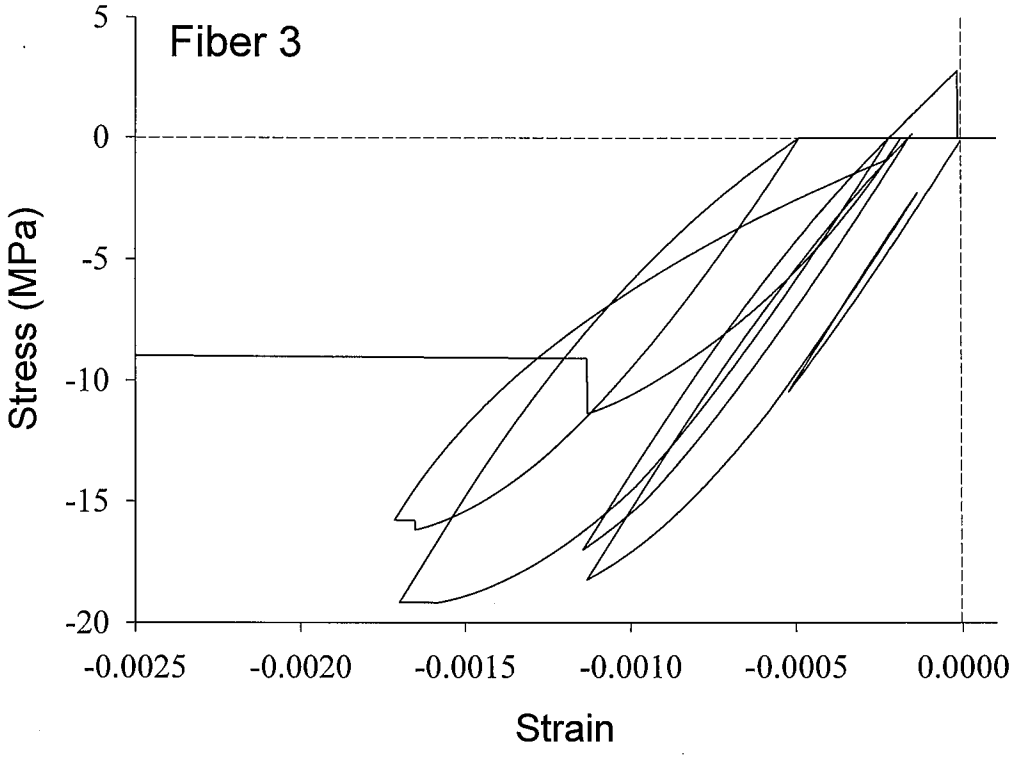

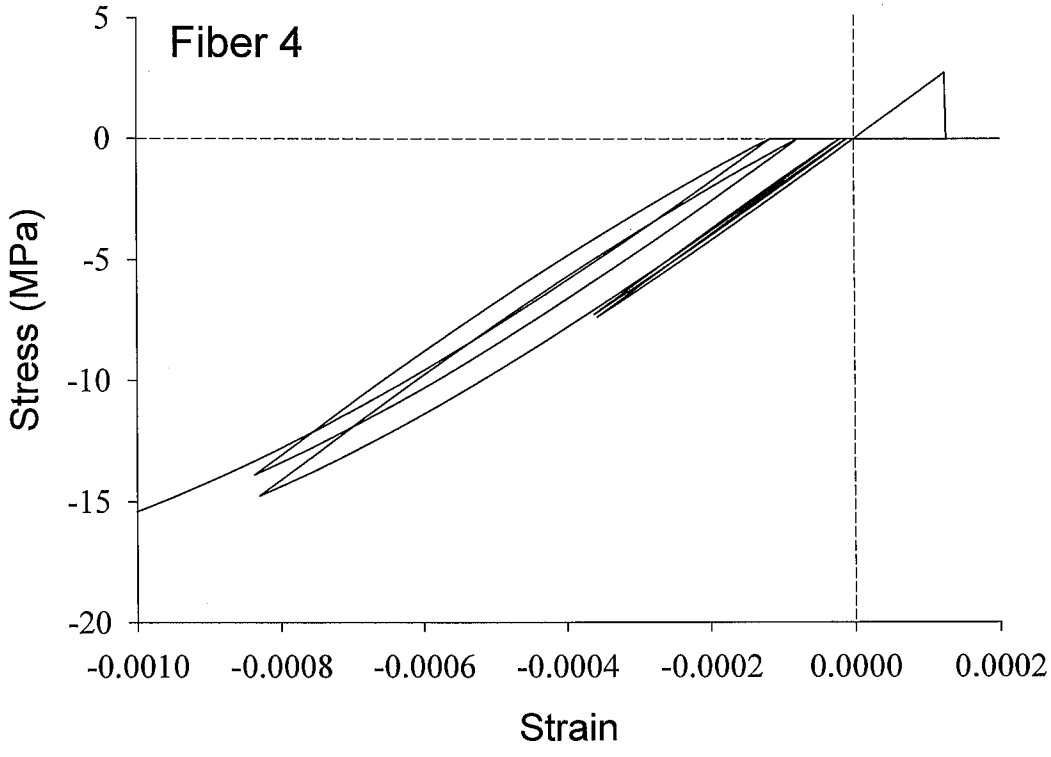

Figure 5.10: Corner Concrete Fibers, Element 8 (continued)

of its strength. This fiber starts with a mean strain close to zero, due to the combined effect of axial load and the out-of-plane tip load. Fibers 2 and 3, Element 7 show more extensive inelastic cycling, since these two fibers start with a compressive initial strain and stress due to the axial load and tip load. Stiffness degradation with the successive cycles is clearly observed for these fibers. Hysteresis loops can be seen in the stress-strain curve for Fiber 4, Element 7, as well, with the unloading stiffness being larger that the loading stiffness. Several small cycles at the low level of stress exhibit almost linear behavior for this fiber. While the concrete model has no elastic zone, it can successfully predict behavior that is close to linear at low levels of stress, followed by an increasing deviation from linearity with increasing stress, as seen in the stress-strain plot for Fiber 4, Element 7.

In order to illustrate the spread of plasticity through the cross section, stress-strain histories for all the steel fibers in the flange of Element 7 (positions of the fibers are marked in Fig. 5.4) are shown in Figure 5.11. All of the plots have the same scale to facilitate comparison of the fibers' behavior. All of these fibers have compressive components of strain and stress due to the axial load, while the stress and strain components created by the out-of-plane tip load change from maximum compression for Fiber fl1 to maximum tension for Fiber fl8. All of the fibers exhibit closed loops which are similar in shape and include some ratchetting, since the nonzero mean strain does not influence the shape of the stress-strain curve, as discussed in Chapter 3. Similar plots for the fibers comprising the web of Element 7 (positions of the fibers are marked in Fig. 5.4) are presented in Figure 5.12. All of the fibers are mostly in compression due to both the axial load and out-of-plane tip load. Fibers close to the middle of the web (i.e., Fibers w3 and w4) are mostly in monotonic compression, with small unloading/reloading branches, since the bending stresses produced by the cyclic loading are small for these fibers.

Stress-strain histories for the concrete flange fibers of Element 7 are shown in Figure 5.13, while those for the web concrete fibers are shown in Figure 5.14. All of the plots have the same scale to facilitate comparison of the fibers' behavior. Fibers fl1 and fl2 are seen to experience the greatest number of loading/unloading loops due to their

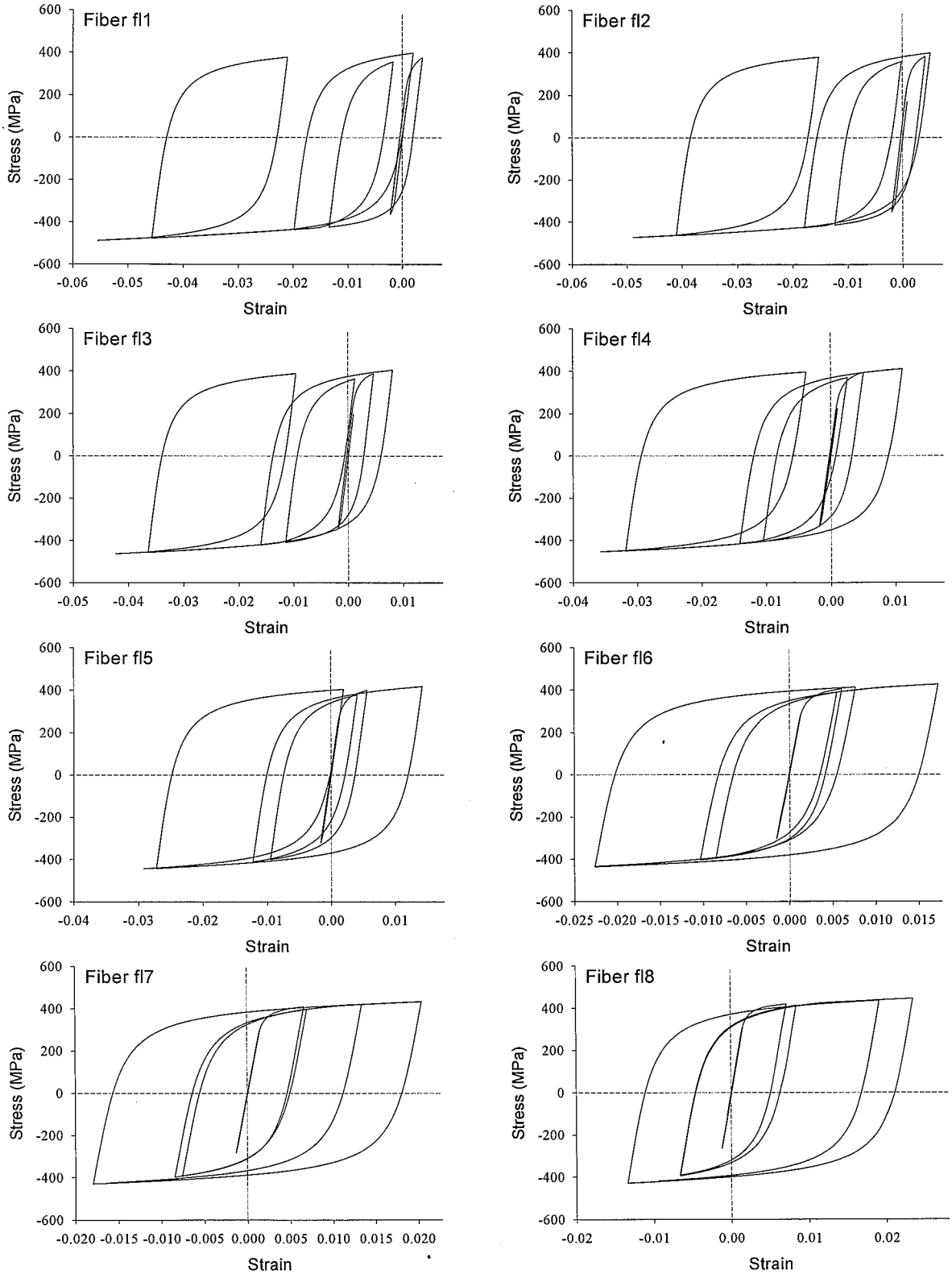

Figure 5.11: Steel Flange Fibers, Element 7

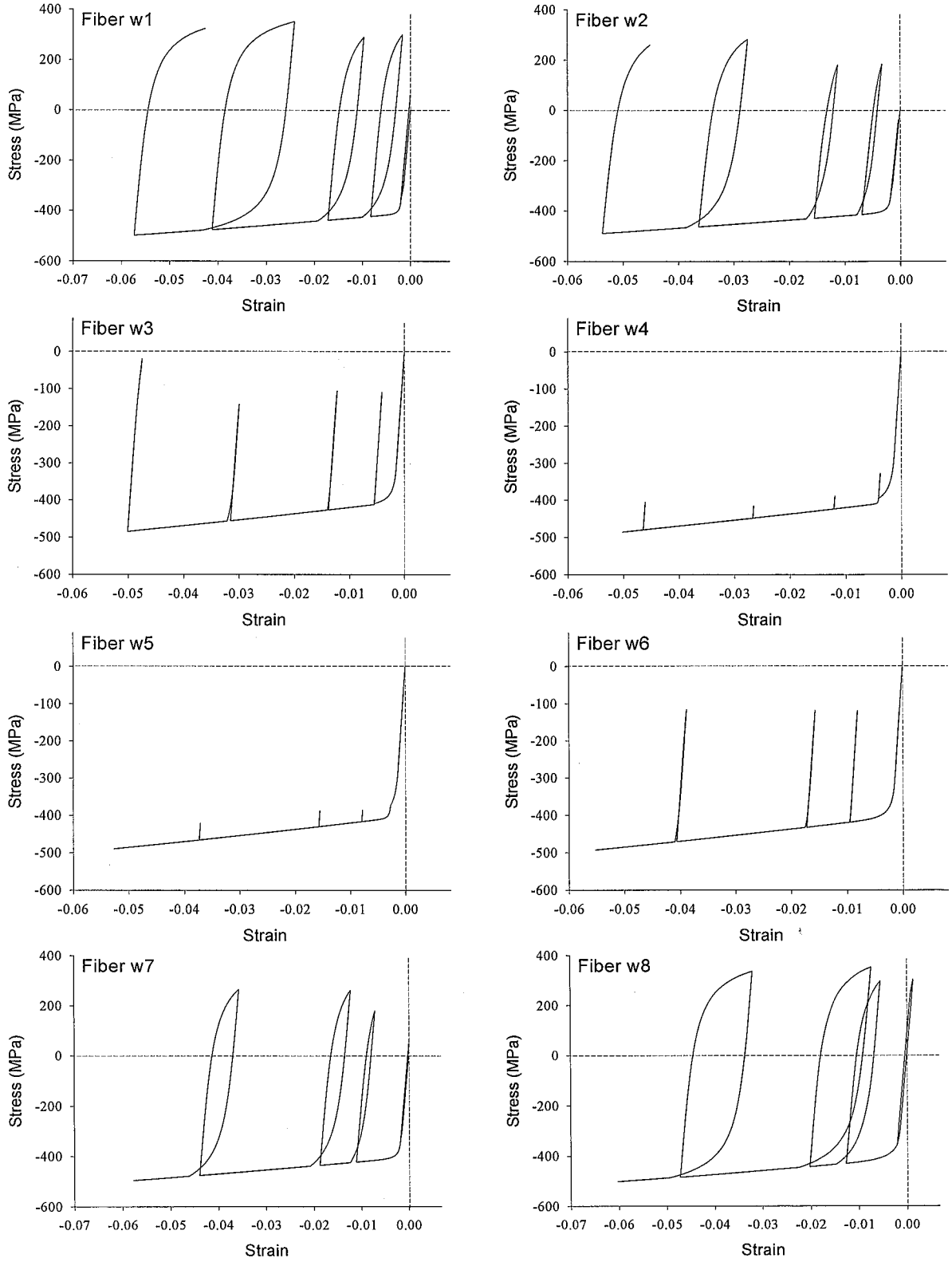

Figure 5.12: Steel Web Fibers, Element 7

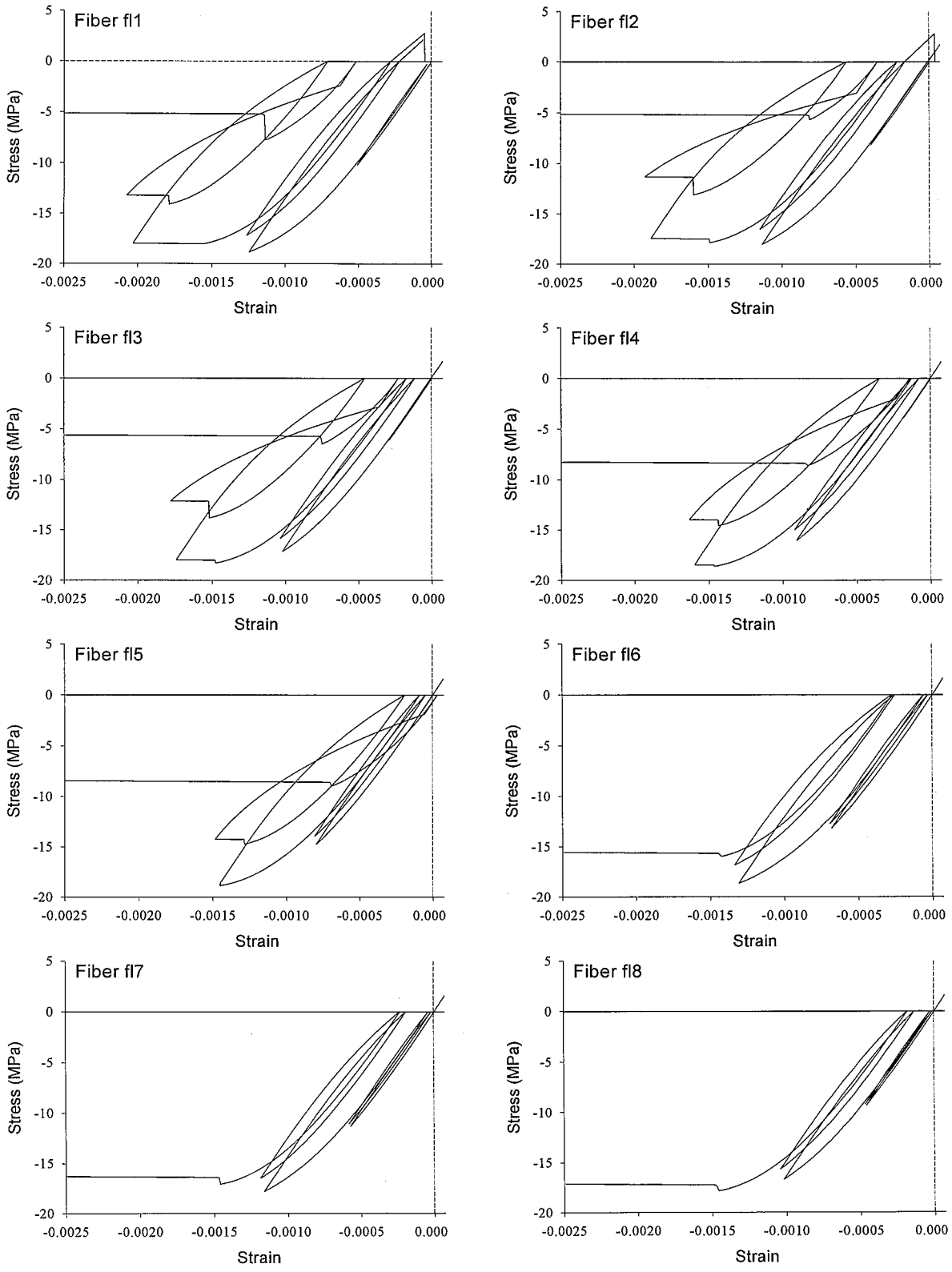

Figure 5.13: Concrete Flange Fibers, Element 7

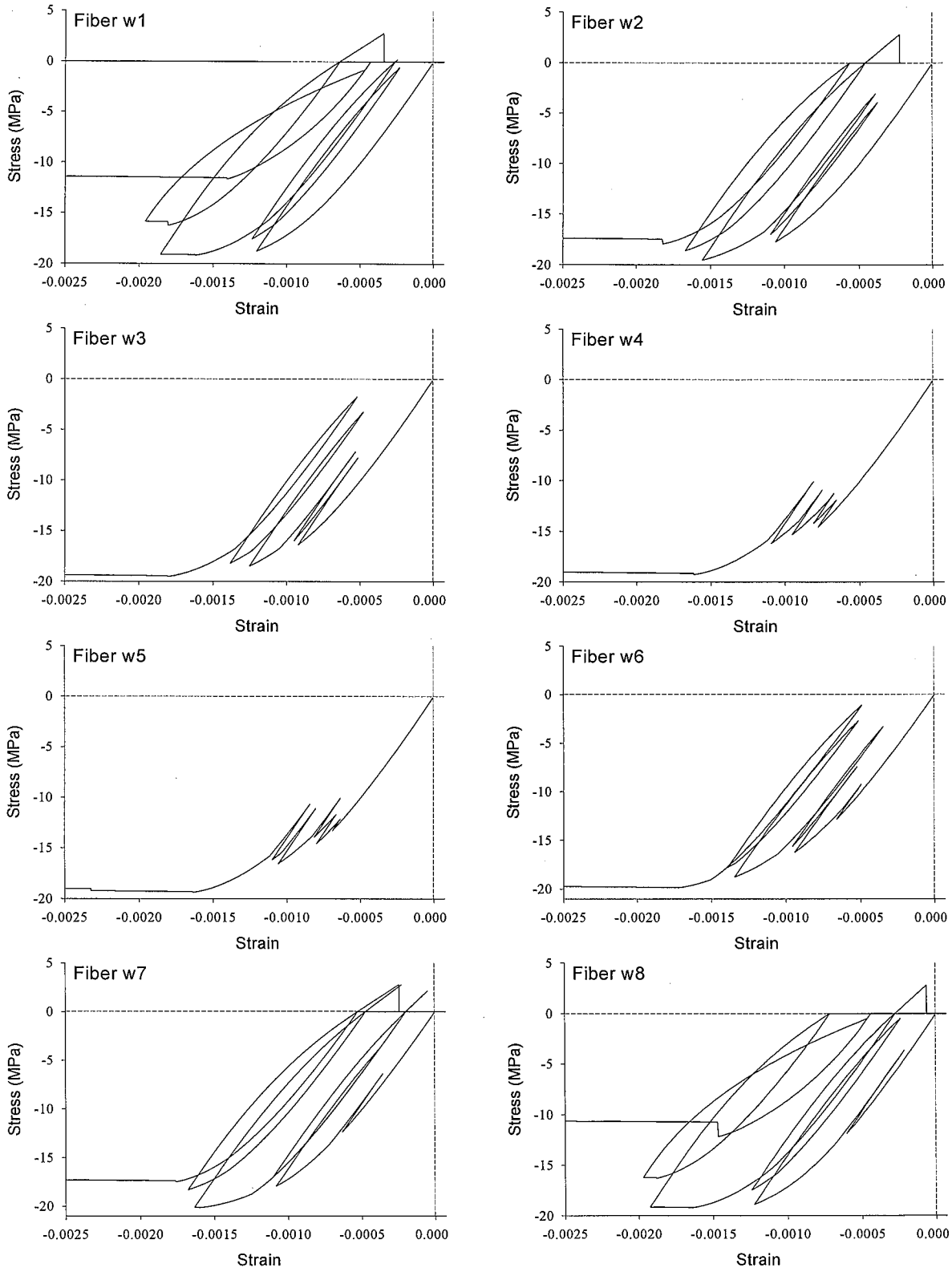

Figure 5.14: Concrete Web Fibers, Element 7

initial compression, while fibers fl7 and fl8, which initially have small mean stresses, show less hysteretic activity prior to crushing fully in a late loading cycle. Fibers close to the middle of the web (i.e., Fibers w3 and w4) have stress-strain curves close to monotonic compression, similar to the corresponding web steel fibers.

Chapter 6

Conclusions

The current research presents a formulation of a beam-column element for cyclic analysis of concrete-filled steel tubes suitable for use in general purpose frame analysis. A distributed plasticity fiber element approach is utilized in which the element end cross sections are discretized in a grid of fibers. Stress and strain histories are monitored for each fiber for the duration of the analysis, and all cross-sectional stress resultants and rigidities are calculated by numerical integration of the fiber properties and stresses. This approach allows modeling the spread of plasticity within the element without substantially increasing the number of the structural degrees-of-freedom over that of a standard twelve degree-of-freedom beam element. Interlayer slip between the steel tube and the concrete core is modeled by providing a nonlinear slip interface. Geometric nonlinearity is accounted for comprehensively by retaining the second order terms of the strain tensor, so that the formulation is suitable for large displacement, moderate rotations, and small strain problems. A similar formulation for a steel element adapted from (White, 1986) is included for modeling steel wide-flange members as components of composite steel and CFT frames.

The current research is suitable for both monotonic and cyclic analysis of CFTs subjected either to proportional or nonproportional loading. The fiber element developed in this research has been incorporated into a general purpose frame analysis computer program, CFTFiber, originally written for monotonic analysis of CFTs by Schiller

(Schiller and Hajjar, 1996). Cyclic plasticity models for both steel and concrete were implemented in this work to permit modeling the materially nonlinear behavior of CFTs subjected to cyclic loading. The current formulation has been verified by comparing computed and experimentally observed structural responses of a set of CFT elements, including proportionally and nonproportionally loaded beams and beam-columns. A final verification problem presents a complete three-dimensional subassamblage subjected to the nonproportional cycling loading.

This chapter provides a summary of the current research, with the main focus on modeling material nonlinearity of cyclically loaded CFTs. Comparison of computational and experimental results is discussed, followed by suggestions for future research.

6.1 Summary of Cyclic Analysis of Composite CFT Frames

While a significant amount of research has been conducted on computational modeling of CFT beam-columns, no distributed plasticity formulation suitable for modeling composite frames with CFT elements subjected to cyclic loading has been reported in the literature. A concentrated plasticity "macro" model capable of cyclic analysis of CFTs as part of composite frames has been developed by Gourley and Hajjar (1994), and a distributed plasticity formulation for monotonic analysis of composite frames including CFTs has been developed by Schiller and Hajjar (1996). The current research extends this work by incorporating cyclic steel and concrete plasticity models, so that cyclic behavior of CFT beam-column elements, subassemblies, and composite frames may be studied.

The current formulation offers a variety of possible applications to the analysis of CFTs:

1. Conducting parametric studies in order to assess the influence of various parameters on the structural behavior. Such studies may be utilized for developing the design provisions that account for the material and geometrically nonlinear behavior in an approximate fashion.
2. Calibrating computationally more efficient but less refined "macro" models. This calibration is particularly needed if a different type of steel or concrete is used for the CFT elements.
3. Estimating the strength and stiffness of the prototype structures used in the experimental investigations of the CFT behavior. Since such structures may have innovative designs, they are less amenable to analysis by more conventional methods.
4. Conducting fully nonlinear dynamic analysis in order to assess the behavior of the composite frame subjected to the earthquake loading (dynamic analysis capabilities are pending).

The finite element formulation of the beam-column fiber element for the CFT analysis is presented in Chapter 2. It describes calculation of the element stiffness matrix, force recovery procedure, modeling the geometric and material nonlinearity, and inclusion of the interlayer slip in the element formulation.

Chapter 3 discusses the salient features of the cyclic response of a typical CFT beam-column that must be captured by a model. The requirement to the steel plasticity formulations are deduced from these features, and the steel plasticity model adopted for this research is then described. Specific characteristic of cold-formed steel tubes such as lack of the yield plateau, residual strains due to cold-forming, and variation of material properties across the cross section are discussed, followed by a description of the extensions of the steel model made to account for these features. Calibration of the steel model to the results of the hollow steel tube experiments is presented at the end of the chapter.

Modeling cyclic behavior of the concrete core is described in Chapter 4. Requirements to the concrete plasticity model are derived from the structural behavior of

CFTs, and the concrete plasticity model adapted for the current research is described in detail. Extensions to the model developed in the course of this research are described, such as adding the capability to model tensile stress and tension-compression transition, and the ability to work in a high compressive strain region. Several implementation issues related to the integration of the rate plasticity equations are discussed. Finally, modification of the model to account approximately for the confinement provided by the steel tube, and calibration to the experimental moment-curvature diagrams are described.

Verification of the model is presented in Chapter 5, where computational results are compared to the experimental data for a set of monotonic and cyclic tests. The final example describes a three-dimensional composite subassemblage consisting of steel girders framing rigidly into a CFT beam-column subjected to axial force and cyclic biaxial bending. Time histories of several computed quantities are presented in order to provide insight into the structural behavior of a CFT member as a part of a complete subassamblage.

6.2 Suggestions for Future Research

The current work is part of a computational research program on CFT behavior conducted at the University of Minnesota. It builds upon the concentrated plasticity formulation of Gourley and Hajjar (1994), and the distributed plasticity formulation for monotonic analysis of CFTs of Schiller and Hajjar (1996).

The current formulation is capable of modeling the cyclic behavior of CFT beam-columns, and composite frames consisting of CFT and steel members. Additional capabilities that would be desirable include:

1. *Modeling of local buckling of the steel tube.* It is known the effect of local buckling can significantly change the overall structural response of a CFT member, particularly

when subjected to cyclic loading (Matsui, 1985). Since local buckling is primarily a geometric local phenomenon, it cannot be modeled explicitly within the framework of a fiber analysis formulation. It may be possible, however, to account for it approximately by modifying the steel constitutive relation, e.g., as suggested in (Tomii and Sakino, 1979).

2. *Dynamic analysis.* Fully nonlinear dynamic analysis is an effective research tool for studying seismic structural response of CFT members.
3. *Ability to carry the analysis past the limit point.* Currently the analysis performed by CFTFiber program is load-controlled. Limit point detection is implemented by checking the positive-definitness of the global tangent stiffness matrix, but the analysis cannot proceed past the first limit point. Consequently, the descending branches of the load-deformation curves, often observed in the cyclic CFT experiments (Sakino and Tomii, 1981), cannot be modeled. Implementation of a limit point handling algorithm in the analysis [i.e., an arc-length type procedure (Crisfield, 1991)] will allow modeling of this type of behavior.
4. *Explicit modeling of concrete confinement.* Currently, the confinement of the concrete core by the steel tube is accounted for approximately by modifying the descending branch of the concrete stress-strain curve. It may be desirable to model the confining effect explicitly by calculating hoop stresses and strains in both the steel tube and the concrete core, and monitoring the contact between the two materials.
5. *Connection modeling.* All connections are assumed to be either pinned or fully-restrained, and no panel zone deformations are accounted for in the present research. Modeling connection behavior in a more comprehensive fashion will extend the program capabilities to performing complete system analysis of composite frames.

Appendix A

List of Symbols

a = steel model parameter used in the loading surface radius calculation

${}^{1}A^{m}$ = area of material m at C1

b = steel model parameter used in the loading surface radius calculation

c = steel model parameter used in the loading surface radius calculation

c = pertaining to concrete

${}_{1}C_{ijkl}$ = material constitutive tensor at C1

$\{\Delta d\}$ = vector of nodal displacement increments

D = tube depth measurement

D = normalized distance to the concrete bounding surface

D_{old} = previous value of the normalized distance to the concrete bounding surface

D_1, D_2 = distances used for subassembly drift rotation measurement

e = constant used in shape parameter calculation

${}_{1}e_{ij}$ = linear Green-Lagrange strain tensor at C1

${}_{2}e_{ij}$ = linear Green-Lagrange strain tensor at C2

Δe_{xx} = incremental strain at a point measured in the direction of the element centroid

Δe_{xy}, Δe_{xz} = incremental shear strains at a point

Δe_m^m = incremental elongation between the i-end node and the midpoint node of material m

Δe^m = incremental elongation between the i-end node and the j-end node of material m

${}^1E^m$ = uniaxial tangent modulus of material m at C1

E_0^p = bounding modulus of steel

E_{0i}^p = initial value of the bounding modulus of steel

${}^1EA_i^m$ = axial rigidity at the i-end of the element of material m at C1

${}^1EI_{yyi}^m$ = flexural rigidity about the y-axis at the i-end of the element of material m at C1

${}^1EI_{zzi}^m$ = flexural rigidity about the z-axis at the i-end of the element of material m at C1

${}^1EI_{yzi}^m$ = modulus times second moment of the area about the y and z-axes at the i-end of the element of material m at C1

${}^1EQ_{yi}^m$ = modulus times first moment of the area about the y-axis at the i-end of the element of material m at C1

${}^1EQ_{zi}^m$ = modulus times first moment of the area about the z-axis at the i-end of the element of material m at C1

f = constant used in shape parameter calculation

f_{bond} = bond strength of the slip interface

f'_c = concrete compressive strength

f_u = steel ultimate strength

f_y = steel yield strength

F_1 = concrete constitutive model parameter which accounts for the hydrostatic pressure and stress path dependency

F_2 = concrete constitutive model parameter which accounts for the multiaxial stress state of the concrete

F_i = generic force resultant at the i-end of a member

h = shape parameter used in steel plastic modulus calculation

H = applied horizontal load

H^P = plastic modulus of concrete

${}^2I$ = steel-concrete interface at C2

I_1 = first stress invariant

$I_{1,\text{old}}$ = previous value of the first stress invariant

$I_{1,\max}$ = maximum value of the first stress invariant

J_2 = second deviatoric stress invariant

J_2^* = second deviatoric stress invariant corresponding to the image stress point

J_3 = third deviatoric stress invariant

$\hat{k}$ = stiffness per unit area of the slip interface

k = tangent stiffness of the slip interface per unit length

k_{slip} = initial stiffness of the slip interface per unit length

K^P = plastic modulus of steel

K = damage parameter used for the concrete constitutive model

$K_{\max}$ = maximum value of the damage parameter K achieved in the loading history

$K_{\max,old}$ = previous maximum value of the damage parameter K

L = element length

m = shear span for a flexural test

M = applied bending moment

M_u = ultimate moment a member can sustain

$\hat{n}$ = unit vector

${}_1\hat{n}$ = unit vector at C1

p = point inside the element volume

P = applied axial force

P_0 = ultimate axial strength

P_{max} = maximum observed axial load for a column test

Q = applied shearing force

r = current stress point radius

R = image stress point radius

R = element chord rotation

$\{\Delta R\}$ = vector of global incremental applied loads

$\{\Delta\Re\}$ = incremental applied load vector for an element

s = pertaining to steel

s_i = principal deviatoric stresses

${}^2S$ = surface of the element at C2

S_{ij} = current stress point in deviatoric stress space

${}^2_1S_{ij}$ = second Piola-Kirchhoff stress tensor (PK2) measured at C2 with respect to C1

t = tube thickness

${}^2t_i$ = surface tractions at C2

T = torque

${}_2u_i$ = element deformations measured with respect to C2

Δu_c^m = incremental deformation of the element centroid in the corotational x-axis direction for material m

Δu^m = incremental deformation of any point in the element volume in the corotational x-axis direction for the material m

$\{\Delta U\}$ = vector of global incremental displacements

V = applied shear force

${}^2V$ = volume of the element at C2

${}^1V^m$ = volume of material m at C1

W = applied shear force

W^P = plastic work

x = distance measured along corotational x-axis

y = distance measured along corotational y-axis

z = distance measured along corotational z-axis

α = angle to the major axis at which an eccentrically applied axial load is located

β_{ij} = centroid of the steel bounding surface

δ = midpoint displacement of a flexural test

δ = plastic distance

δ_{in} = initial plastic distance

δ_m = metric distance between the point of reversal and its conjugate point on the memory surface

δ_v = metric distance between the point of reversal and its conjugate point on the memory surface

Δ = deflection of an axially loaded column

$\varepsilon_{p\ initial}$ = initial plastic strain used in the steel constitutive model

${}_1\varepsilon_{ij}$ = Green-Lagrange strain measured with respect to C1

ε^s = steel strain

ε_c = concrete strain corresponding to the peak stress

γ = kinematic hardening parameter

$d\gamma_o^p$ = octahedral plastic shear strain increment

κ = steel loading surface radius

$\overline{\kappa}$ = steel bounding surface radius

$\overline{\kappa}_m$ = radius of the steel memory surface

${}_1\eta_{ij}$ = nonlinear Green-Lagrange strain terms at C1

η_{ij} = center of the limiting surface in the plastic strain space

${}^2\pi$ = stress in the slip interface at C2

θ = rotation

ρ = perimeter of steel-concrete interface

ρ = radius of the non-hardening surface

σ_I = principal stresses

${}^1\tau^m$ = uniaxial stress in material *m* at C1

${}^2\tau_{ij}$ = Cauchy stress tensor measured at C2

τ_o = octahedral shear stress

$\varphi(\Delta d)$ = nonlinear function of the nodal displacement increments

ω = steel model parameter used in the bounding modulus calculation

${}_2\psi$ = deformation of the slip interface measured with respect to C2

$\Delta\psi$ = incremental deformation in the slip layer

${}^1\zeta^m_{yyi}$ = internal second moment of the stress about the *y*-axis at the i-end of the element of material *m* at C1

${}^1\zeta^m_{yzi}$ = internal second moment of the stress about the *y* and *z*-axes at the i-end of the element of material *m* at C1

${}^1\zeta^m_{zzi}$ = internal second moment of the stress about the *z*-axis at the i-end of the element of material *m* at C1

References

Ahmad, S. H. and Weerakoon, S. L. (1995). "Model for Behavior of Slender Reinforced Concrete Columns under Biaxial Bending," *ACI Structural Journal*, Vol. 92 No. 2, pp. 188-198.

Alvarez, R. J. and Birnstiel, C. (1969). "Inelastic Analysis of Multistory Multibay Frames," *Journal of the Structural Division*, ASCE, Vol. 95, No. ST11, pp. 2477-2503.

American Society of Civil Engineers (1982). "State-of-the-Art Report on Finite Element Analysis of Reinforced Concrete," ASCE Task Committee, Nilson, A. (chairman), ASCE, New York, NY.

Ameur-Moussa and Buyukozturk (1990). "A Bounding Surface Model for Concrete," *Nuclear Engineering and Design*, Vol. 121, pp. 113-125.

Bathe, K. (1982). *Finite Element Procedures in Engineering Analysis*, Prentice-Hall, Inc., Englewood Cliffs, NJ, 735 pp.

Bode, H. (1976). "Columns of Steel Tubular Sections Filled with Concrete Design and Applications," *Acier Stahl*, No. 11/12, pp. 388-393.

Bridge, R. Q. (1976). "Concrete Filled Steel Tubular Columns," *Report No. R283*, School of Civil Engineering, University of Sydney, Sydney, Australia.

Bridge, R. Q., and Webb, J. (1993). "Thin Walled Circular Concrete Filled Steel Tubular Columns," *Composite Construction in Steel and Concrete II*, Easterling, W. S. and Roddis, W. M. (eds.), Engineering Foundation, ASCE, New York, NY, pp. 634-649.

Buyukozturk and Ameur-Moussa (1988). "A Bounding Surface Model for Concrete," *Bulletin of the Technical University of Istanbul*, Vol. 41, pp. 169-199.

Cederwall, K., Engstrom, B., and Grauers, M. (1991). "High-Strength Concrete Used in Composite Columns," Proceedings of the Second International Symposium on Utilization of High-Strength Concrete, Hester, W. T. (ed.), Berkeley, CA, May 1990, pp. 195-214.

Chaboche, J. L. (1986). "Time-Independent Constitutive Theories for Cyclic Plasticity," *International Journal of Plasticity*, Vol. 2, No. 2, pp. 149-188

Chaboche, J.-L., Van, K. Dang, and Cordier, G. (1979). "Modelization of the Strain Memory Effect on the Cyclic Hardening of 316 Stainless Steel," Proceedings of the 5th International Conference on Structural Mechanics in Reactor Technology, Berlin, Germany, Elsevier Science Publishers Ltd., Amsterdam.

Challa, V. and Hall, J. (1994). "Earthquake Collapse Analysis of Steel Frames," *Earthquake Analysis and Structural Dynamics*, Vol. 23, pp. 1199-1218.

Chang, G. A. and Mander, J. B. (1994). "Seismic Energy Based Fatigue Damage Analysis of Bridge Columns: Part I - Evaluation of Seismic Capacity." Report No. NCEER-94-0006, National Center for Earthquake Engineering Research, State University of New York at Buffalo, Buffalo, NY.

Chang, K. C. and Lee, G. C. (1986). "Constitutive Relations of Structural Steel Subjected to Nonproportionally Applied Stresses," *Journal of Engineering Mechanics*, ASCE, Vol. 112, No. 8, pp. 792-805

Chen, E. S. and Buyukozturk, O. (1985). "Constitutive Model for Concrete in Cyclic Compression," *Journal of Engineering Mechanics*, ASCE, Vol. 111, No. 6, pp. 797-813.

Chen, W. F. and Chen C. H. (1973). "Analysis of Concrete-Filled Steel Tubular Beam-Columns," *Memoires*, IABSE, Vol. 33, No. II, pp. 37-52.

Chen, W. F. and Han, D. J. (1988). *Plasticity for Structural Engineers*, Springer-Verlag, New York, NY.

Clarke, M. J. (1992), "The Behavior of Stressed-Arch Frames," Ph.D. dissertation, School of Civil and Mining Engineering, University of Sydney, Sydney, Australia.

Cofie, N. G. and Krawinkler, H. (1985), "Uniaxial Cyclic Stress-Strain Behavior of Structural Steel," *Journal of Engineering Mechanics*, ASCE, Vol. 111, No. 9, pp. 1105-1120.

Crisfield, M. A. (1991). *Nonlinear Finite Element Analysis of Solids and Structures*, John Wiley & Sons, New York, NY.

Dafalias, Y. F. (1986). "Bounding Surface Plasticity. I: Mathematical Foundation and Hypoplasticity," *Journal of Engineering Mechanics*, ASCE, Vol. 112, 1986, pp. 966-987

Dafalias, Y. F. (1992). "Bounding Surface Plasticity Model for Steel under Loading," *Stability and Ductility of Steel Structures under Cyclic Loading*, Fukumoto, Y. and Lee, G. C. (eds.), CRC Press, Boca Raton, FL, pp. 25-36

Dafalias, Y. F. and Popov, E. P. (1975). "A Model of Nonlinearly Hardening Materials for Complex Loading." *Acta Mechanica*, Vol. 21, pp. 173-191.

Dafalias, Y. F. and Popov, E. P. (1976). "Plastic Internal Variables Formalism of Cyclic Plasticity," *Journal of Applied Mechanics*, Vol. 49, No. 4, pp. 645-650

Dafalias, Y. F. and Popov, E. P. (1977). "Cyclic Loading for Materials with a Vanishing Elastic Region," *Nuclear Engineering and Design*, Vol. 41, No. 2, pp. 293-302.

Drucker, D. C. and Palgen, L. (1981). "On Stress-Strain Relations Suitable for Cyclic and Other Loading," *Journal of Applied Mechanics*, Vol. 48, pp. 479-485

El-Tawil, S. and Deierlein, G. G. (1996). "Inelastic Dynamic Analysis of Mixed Steel-Concrete Space Frames," *Structural Engineering Report No. 96-5*, School of Civil and Environmental Engineering, Cornell University, Ithaca, NY.

Elnashai, A. and Elghazouli, A. (1993). "Performance of Composite Steel/Concrete Members Under Earthquake Loading. Part I: Analytical Model," *Earthquake Engineering and Structural Dynamics*, Vol. 22, pp. 315-345.

Fujimoto, T., Nishiyama, I, Mukai, A., and Baba, T. (1996). "Test Results of Concrete Filled Steel Tubular Beam-Columns," U.S.-Japan Joint Technical Coordination Conference on Composite and Hybrid Structures, U.S.-Japan Cooperative Earthquake Engineering Program, Phase 5, Hong Kong, December 12-14, 1996.

Gourley, B. and Hajjar, J. (1994). "Cyclic Nonlinear Analysis of Three-Dimensional Concrete-Filled Steel Tube Beam-Columns and Composite Frames," *Structural Engineering Report No. ST-94-3*, Department of Civil Engineering, University of Minnesota, Minneapolis, MN.

Gourley, B. C., Hajjar, J. F., and Schiller, P. H. (1995). "A Synopsis of Studies of the Monotonic and Cyclic Behavior of Concrete-Filled Steel Tube Beam-Columns," *Structural Engineering Report No. ST-93-5.2*, Department of Civil Engineering, University of Minnesota, Minneapolis, MN.

Hajjar, J. F. and Gourley, B. C. (1996). "Representation of Concrete-Filled Steel Tube Cross-Section Strength," *Journal of Structural Engineering*, ASCE, Vol. 122, No. 11, pp. 1327-1336.

Hajjar, J. F., Gourley, B. C., and Olson, M. C. (for Part II) (1997a). "A Cyclic Nonlinear Model for Concrete-Filled Tubes. I. Formulation. II: Verification," *Journal of Structural Engineering*, ASCE, Vol. 123, No. 6, pp. 736-754.

Hajjar, J. F., Schiller, P. H., and Molodan, A. (1997b). "A Distributed Plasticity Model for Concrete-Filled Steel Tube Beam-Columns with Interlayer Slip," *Engineering Structures*, at press.

Hajjar, J. F., Molodan, A., and Schiller, P. H. (1997c). "A Distributed Plasticity Model for Cyclic Analysis of Concrete-Filled Steel Tube Beam-Columns and Composite Frames," *Engineering Structures, Special Volume on Innovations in Stability Concepts and Methods for Seismic Design in Structural Steel*, at press.

Hajjar, J. F., Gourley, B. C., Schiller, P. H., Molodan, A., and Stillwell, K. A. (1997d). "Seismic Analysis of Concrete-Filled Steel Tube Beam-Columns and Three-Dimensional Composite Frames." *Composite Construction III*, Buckner, C.D. and Shahrooz, B. M. (eds.), Engineering Foundation, ASCE, New York, NY, at press.

Inai, E, and Sakino, K. (1996). "Simulation of Flexural Behavior of Square Concrete Filled Steel Tubular Columns," U.S.-Japan Joint Technical Coordination Conference on Composite and Hybrid Structures, U.S.-Japan Cooperative Earthquake Engineering Program, Phase 5, Hong Kong, December 12-14, 1996.

Izzuddin, B. A. and Elnashai, A. S. (1993). "Adaptive Space Frame Analysis. Part II: A Distributed Plasticity Approach." *Proceedings of the Institute of Civil Engineering*, Vol. 99, pp. 317-326.

Izzuddin, B. A., Karayannis, C. G., and Elnashai, A. S. (1994). "Advanced Nonlinear Formulation for Reinforced Concrete Beam-Columns." *Journal of Strucural Engineering.*, ASCE, Vol. 120, No. 10, pp. 2913-2934.

Kanchanalai, T. (1977). "The Design and Behavior of Beam-Columns in Unbraced Steel Frames," AISI Project No. 189, Civil Engineering/Structures Research Laboratory Report No. 77-2, Department of Civil Engineering, Structures Research Laboratory, University of Texas at Austin, Austin, TX.

Kawaguchi, J., Morino, S., Atsumi, H., and Yamamoto, S. (1991a). "Strength Deterioration Behavior of Concrete-Filled Steel Tubular Beam-Columns Under Repeated Horizontal Loading," Proceedings of the Third International Conference on Steel-Concrete Composite Structures, Wakabayashi, M. (ed.), Fukuoka, Japan, 26-29 September 26-29, 1991, pp. 119-124.

Kawaguchi, J., Morino, S., and Yasuzaki, C. (1991b). "Elasto-Plastic Behavior of Concrete-Filled Steel Tubular Three-Dimensional Subassemblages," Research Report of the Faculty of Engineering, Mie University, Tsu, Mie, Japan, Vol. 16, pp. 61-78

Kawaguchi, J., Morino, S., Atsumi, H., and Yamamoto, S. (1993). "Strength Deterioration Behavior of Concrete-Filled Steel Tubular Beam-Columns," *Composite Construction in Steel and Concrete II*, Easterling, W. S., and Roddis, W. M. (eds.), Engineering Foundation, ASCE, New York, NY, pp. 825-839.

Kawaguchi, J., Morino, S. and Sugimoto, T. (1996). "Elasto-Plastic Behavior of Concrete Filled Steel Tubular Frames," *Composite Construction III*, Buckner, C.D. and Shahrooz, B. M. (eds.), Engineering Foundation, ASCE, New York, NY, at press.

Key, P. W, Hasan, S. W., and Hancock, G. J. (1988). "Column Behavior of Cold-Formed Hollow Sections," *Journal of Structural Engineering*, ASCE, Vol. 114, No. 2, pp. 390-470.

Khan, A. S. and Huang, S. (1995). *Continuum Theory of Plasticity.* John Wiley and Sons, NewYork, NY.

Krishnamoorthy, C. S. (1987). "Finite Element Models for Inelastic Analysis of Reinforced Concrete Frames and Application to Limit State Design," *Computational Plasticity: Models, Software and* Applications, Owen, D. R. J., Hinton, E., and Onate, E. (eds.), Pineridge Press, Swansea, U.K.

Lee, G. C., Chang, K. C., and Sigura, K. (1992). "The Experimental Basis of Material Constitutive Laws of Structural Steel under Cyclic and Nonproportional Loading," *Stability and Ductility of Steel Structures under Cyclic Loading*, Fukumoto, Y. and Lee, G. C. (eds.), CRC Press, Boca Raton, FL, pp. 3-14.

LeMaitre, J. and Chaboche, J. (1990). *Mechanics of Solid Materials*. Cambridge University Press, Melbourne, Australia.

Lu, Y. and Kennedy, D. (1994). "Flexural Behavior of Concrete-Filled Hollow Structural Sections," *Canadian Journal of Civil Engineering*, Vol. 21, No. 1, pp. 11-130.

Mamaghani, I. H. P., Shen, C., Mizuno, E., and Usami, T. (1995). "Cyclic Behavior of Structural Steels. I: Experiments," *Journal of Engineering Mechanics*, ASCE, Vol. 121, No. 11, pp. 1158-1164.

Matsui, C. (1985). "Local Buckling of Concrete Filled Steel Square Tubular Columns," Proceedings of the IABSE-ECCS Symposium on Steel Buildings, IABSE Reports, Vol. 48, pp. 269-276.

Matsui, C. (1986). "Strength and Deformation Capacity of Frames Composed of Wide Flange Beams and Concrete Filled Square Steel Tubular Columns," Proceedings of the Pacific Structural Steel Conference, Auckland, New Zealand, August 4-8, 1986, Vol. 2, pp. 169-181.

Matsui, C. and Tsuda, K. (1987). "Strength and Behavior of Concrete-Filled Steel Square Tubular Columns with Large Width-Thickness Ratio," Proceedings of Pacific Conference on Earthquake Engineering, Vol. 2, Wellington, New Zealand, 1987, pp. 1-9.

Mizuno, E., Shen, C., Tanaka, Y., and Usami, T. (1992). "A Uniaxial Stress-Strain Model for Structural Steels under Cyclic Loading." *Stability and Ductility of Steel Structures under Cyclic Loading*, Fukumoto, Y. and Lee, G. C. (eds.), CRC Press, Boca Raton, FL, pp. 37-48.

Morales, L. E. (1994). "Object-Oriented Software and Advanced Analysis of Steel Frames," M.S. thesis, School of Civil Engineering, Purdue University, West Lafayette, IN.

Morino, S., Kawaguchi, J., Yasuzaki, C., and Kanazawa, S. (1993). "Behavior of Concrete-Filled Steel Tubular Three-Dimensional Subassemblages," *Composite Construction in Steel and Concrete II*, Easterling, W. S. and Roddis, W. M. (eds.), Engineering Foundation, ASCE, New York, NY, pp. 726-741.

Mroz, Z. (1967). "On the Description of Anisotropic Workhardening," *Journal of Mechanics and Physics of Solids*, Vol. 15, pp. 163-175.

Ohno, N. (1982). "A Constitutive Model of Cyclic Plasticity with a Nonhardening Strain Region," *Journal of Applied Mechanics Transactions*, ASME, Vol. 49, pp. 721-727.

Ohno, N. and Kachi, Y. (1986). "A Constitutive Model of Cyclic Plasticity for Nonlinear Hardening Materials," *Journal of Applied Mechanics Transactions*, Vol. 53, No. 2, pp. 395-403.

Pagnoni, T., Slater, J., Ameur-Moussa, R., and Buyukozturk, O. (1992). "A Nonlinear Three-Dimensional Analysis of Reinforced Concrete Based on a Bounding Surface Model," *Computers and Structures*, Vol. 43, No. 1, pp. 1-12.

Prager, W. (1956). "A New Method of Analyzing Stresses and Strains in Work-Hardening Plastic Solids," *Journal of Applied Mechanics*, Vol. 23, pp. 493-496.

Roik, K. and Bergmann, R. (1992). "Composite Columns," *Constructional Steel Design: An International Guide*, Dowling, P. J., Harding, J. E., and Bjorhovde, R. (eds.), Elsevier Science Publishers Ltd., New York, NY, pp. 443-469.

Sakino, K. and Tomii, M. (1981). "Hysteretic Behavior of Concrete Filled Square Steel Tubular Beam-Columns Failed in Flexure," *Transactions of the Japan Concrete Institute,* Vol. 3, pp. 439-446.

Sakino, K., and Ishibashi, H. (1985). "Experimental Studies on Concrete Filled Square Steel Tubular Short Columns Subjected to Cyclic Shearing Force and Constant Axial Force," *Transactions of the Architectural Institute of Japan*, No. 353, pp. 81-89.

Schiller, P. H. and Hajjar, J. F. (1996). "A Distributed Plasticity Formulation for Three-Dimensional Rectangular Concrete-Filled Steel Tube Beam-Columns and Composite Frames," *Structural Engineering Report*, No. ST-96-5, Department of Civil Engineering., University of Minnesota, Minneapolis, MN.

Shakir-Khalil, H. and Zeghiche, Z. (1989). "Experimental Behavior of Concrete-Filled Rolled Rectangular Hollow-Section Columns," *The Structural Engineer*, Vol. 67, No. 19, pp. 345-353.

Shen, C. (1993). "Development of a Cyclic Two-Surface Model for Structural Steels With Yield Plateau," Ph.D. dissertation, Nagoya University, Nagoya, Japan.

Shen, C., Mamaghani, I. H. P., Mizuno, E., and Usami, T. (1995). "Cyclic Behavior of Structural Steels," *Journal of Engineering Mechanics*, ASCE, Vol. 121, No. 11, pp. 1165-1172.

Sherman, D. R. (1992). "Tubular Members," *Constructional Steel Design: An International Guide*, Dowling, P. J., Harding, J. E., and Bjorhovde, R. (eds.), Elsevier Science Publishers Ltd., New York, NY, pp. 91-104.

Sugano, S., Nagashima, T., and Kei, T. (1992). "Seismic Behavior of Concrete-Filled Tubular Steel Columns," Proceedings of the ASCE Structures Congress '92, Morgan, J. (ed.), San Antonio, TX, April 13-16, 1992, ASCE, New York, NY, pp. 914-917.

Sully, R. M. and Hancock, G. J. (1994). "Behavior of Cold-Formed SHS Beam-Columns," *Research Report No. R696*, School of Civil and Mining Engineering, University of Sydney, Sydney, Australia.

Sully, R. M. and Hancock, G. J. (1996). "Behavior of Cold-Formed SHS Beam-Columns," *Journal of Structural Engineering*, ASCE, Vol. 122, No. 3, pp. 326-336.

Taucer, F., Spacone, E., and Filippou, F. (1991). "A Fiber Beam-Column Element for Seismic Response Analysis of Reinforced Concrete Structures," *Report No. UCB/EERC-91/17*, College of Engineering, University of California at Berkeley, Berkeley, CA.

Tomii, M. and Sakino, K. (1979a). "Experimental Studies on the Ultimate Moment of Concrete Filled Square Steel Tubular Beam-Columns," *Transactions of the Architectural Institute of Japan*, No. 275, pp. 55-63.

Tomii, M. and Sakino, K. (1979b). "Elasto-Plastic Behavior of Concrete Filled Square Steel Tubular Beam-Columns," *Transactions of the Architectural Institute of Japan*, No. 280, pp. 111-120.

Tsuji, B., Nakashima, M., and Morita, S. (1991). "Axial Compression Behavior of Concrete Filled Circular Steel Tubes," Proceedings of the Third International Conference on Steel-Concrete Composite Structures, Wakabayashi, M. (ed.), Fukuoka, Japan, September 26-29, 1991, pp. 19-24.

Valanis, K. C. (1971). "A Theory of Viscoplasticity without a Yield Surface (Part I)," *Arch. Mech. Stos.*, Vol. 23, No. 4, pp. 517-551.

Weaver, W. and Gere, J. M. (1990). *Matrix Analysis of Framed Structures*, Van Nostrand Reinhold, New York, NY, 546 pp.

Webb, J. (1993). "High-Strength Concrete: Economics, Design and Ductility," *Concrete International*, Vol. 15, No. 1, pp. 27-32.

White, D. (1986). "Material and Geometric Nonlinear Analysis of Local Planar Behavior in Steel Frames Using Interactive Computer Graphics," M.S. thesis, Department of Structural Engineering, Cornell University, Itasca, NY.

Wright, E. W. and Gaylord, E. H. (1968). "Analysis of Unbraced Multistory Steel Rigid Frames," *Journal of the Structural Division*, ASCE, Vol. 94, No. ST5, pp. 1143-1163.

Zhao, X.-L. and Hancock, G. J. (1992). "Experimental Verification of the Theory of Plastic Moment Capacity of an Inclined Yield Line Under Axial Force," *Research Report No. R649*, School of Civil and Mineral Engineering, University of Sydney, Sydney, Australia.